# Mean structures and temporal variations of the North Pacific subtropical gyre as revealed from an analysis of observational data

Doctoral Dissertation

# MEAN STRUCTURES AND TEMPORAL VARIATIONS OF THE NORTH PACIFIC SUBTROPICAL GYRE AS REVEALED FROM AN ANALYSIS OF OBSERVATIONAL DATA

September 2015

Graduate School of Marine Science and Technology
Tokyo University of Marine Science and Technology
Doctoral Course of Applied Marine Environmental Studies

Masafumi Kimizuka

Doctoral Dissertation

# MEAN STRUCTURES AND TEMPORAL VARIATIONS OF THE NORTH PACIFIC SUBTROPICAL GYRE AS REVEALED FROM AN ANALYSIS OF OBSERVATIONAL DATA

September 2015

Graduate School of Marine Science and Technology
Tokyo University of Marine Science and Technology
Doctoral Course of Applied Marine Environmental Studies

Masafumi Kimizuka

# Abstract

The North Pacific subtropical gyre is a large-scale anticyclonic surface ocean circulation approximately between 15°N and 45°N and is basically driven by surface winds with the northeasterly trade winds to the south and the westerlies to the north. There are two landmark theories for a wind-driven ocean circulation. One is the Sverdrup theory for the two-dimensional barotropic motion of the depth-integrated circulation, and the other is the ventilated thermocline theory for the baroclinic vertical structure of the wind-driven circulation. These theories have motivated many observational and numerical model studies to examine the transport and structure of the ocean circulation and the ventilation of the thermocline from a surface mixed layer, which have advanced greatly our understanding of the wind-driven circulation. However, they have not described the subtropical gyre in detail from observations based on comparisons with the theories. We still have not understood satisfactorily the horizontal and vertical structures of the actual ocean circulation and their temporal changes. This study has investigated the mean structures and temporal variations of the depth-integrated circulation and vertical structures of the North Pacific subtropical gyre using Argo gridded datasets, atmospheric reanalysis products and satellite observations.

In Chapter 2, the mean structures of the subtropical gyre have been investigated using Argo data and several wind stress products, with a particular focus on the gyre axis, which is defined as a large-scale boundary between eastward motions on the northern part of the subtropical gyre and westward motions on the southern part. Structures of the gyre axis are different between the regions east and west of about 180°. In the west, the gyre axis is affected by the strong Kuroshio Extension jet, showing the discrepancy with features expected from the Sverdrup theory and the ventilated thermocline theory. In the

east, depth-integrated geostrophic circulation displays the two gyre axes about 25°N and 30°N in association with a local cyclonic wind stress curl anomaly. It is expected from the Sverdrup balance that the two gyre axes would extend to the west across the subtropical gyre, but the actual geostrophic circulation exhibits only one gyre axis around 30°N to the west.

The vertical structure of the subtropical gyre exhibits a remarkable northward shift of the gyre axis with depth in the east, consistent with the southward decrease in the thickness of density layers around the gyre axis, while the northward shift is less obvious in the west where the gyre axis lies along the southern flank of the Kuroshio Extension. The gyre shift in the east is relatively smaller in the central mode water (CMW) layer due to the horizontal uniformity of the CMW, suggesting the dynamical effect of the CMW on large-scale circulations of the subtropical gyre.

In Chapter 3, using two different Argo datasets and two wind stress products, I have investigated the temporal variations of the depth-integrated circulation and the vertical structures of the subtropical gyre. The depth-integrated circulation reveals a local cyclonic rotation between the two mean gyre axes in the eastern subtropical gyre and a local anticyclonic rotation just lying to the south of the cyclonic rotation. These two rotations show concurrent interannual variations with a predominant period of about 5 years with no notable seasonal cycles. These variations are caused by the vertically coherent change in the eastward flow around 26°N near the boundary of the two local rotations and thus the strong (weak) eastward flow leads to the concurrent intensification (weakening) of the cyclonic rotation to the north and the anticyclonic rotation to the south. This change in the eastward flow is mainly associated with that in the depth-integrated dynamic height to the south of the eastward flow. The lagged regression analysis of the depth-integrated dynamic height and the zonal velocity shows that the signals of these

anomalies propagate southwestward from the northeastern subtropical gyre and are enhanced around 26°N on year-to-year time scales.

The depth-integrated zonal velocity of the eastward flow is compared with the zonal wind-driven transport calculated from surface wind data. Although there is a time lag of about 1 year, they are well correlated with each other, suggesting that the interannual variations of the eastward flow and its associated two local rotations are induced by the local Ekman pumping rather than by large-scale atmospheric forcing. I have discussed the time lag and the possible mechanism of the changes in the Ekman pumping.

The interannual variations of the northward shift of the gyre axis with depth are found in the downstream region of the Kuroshio Extension, where the large northward shift of the gyre axis occurs in coincidence with the relatively weak Kuroshio Extension. In the eastern part of the subtropical gyre, the position of the gyre axis above the upper pycnocline is affected by the eastern subtropical countercurrent (STCC), showing the tendency that the gyre axis appears to the south of the eastern STCC. In the CMW layer, the lower-potential vorticity mode water is sometimes relating to the smaller shift of the gyre axis, but such relationship does not always appear, suggesting that the variations of the gyre axis are affected not only by the CMW but also by other ocean structures. The mechanisms need to be more fully explored in the future.

Chapter 4 provides a summary and general conclusion.

# Table of contents

# Chapter 1
# General introduction

## 1.1 Surface circulation in the North Pacific subtropical gyre

The large-scale surface circulation is characterized by the three major gyres: the tropical gyre, the subtropical gyre and the subpolar gyre. In the North Pacific Ocean, the tropical, subtropical and subpolar gyres are obvious from a cyclonic gyre south of about 15$^{o}$N, an anticyclonic gyre between 15$^{o}$N and 45$^{o}$N and a cyclonic gyre north of 45$^{o}$N, respectively (Fig. 1-1). The subtropical gyre occupies a large portion of the North Pacific Ocean.

The North Pacific subtropical gyre consists of the Kuroshio, the Kuroshio Extension, the North Pacific Current, the California Current and the North Equatorial Current. In the subtropical gyre, there are the Subtropical Countercurrent (STCC) and the Hawaiian Countercurrent (HLCC) (Fig. 1-2). The Kuroshio is the western boundary current of the North Pacific subtropical gyre and flows northward along the southern coast of Japan. After leaving the coast of Japan around 35°N, the Kuroshio penetrates as a free jet in the North Pacific as the Kuroshio Extension (Qiu 2002a; Yasuda 2003). The Kuroshio and the Kuroshio Extension carry warm and saline water from the tropical to mid-latitude regions and release a huge amount of heat to the atmosphere, affecting the overlying atmosphere (Tokinaga et al. 2009; Kwon et al. 2010). The eastward-flowing Kuroshio Extension encounters the Shatsky Rise around 160°E and is split into the two branches. The southern branch partly turns to the west as the recirculation gyre, while the northern branch continues to the eastward-flowing North Pacific Current to the east.

The North Pacific Current is a meridionally broad eastward flow at the central and eastern part of the subtropical gyre. The mean speed of the North Pacific Current is less than 10 cm/s, which is quite smaller than that of the Kuroshio Extension. Recently, it is reported that the North Pacific Current has shifted northward with the shrinking of the Alaska Gyre, which is the eastern subgyre of the North Pacific subarctic gyre, over the past two decades (Douglass et al. 2006; Cummins and Freeland 2007).

The North Equatorial Current is a broad westward current flowing on the southern side of the subtropical gyre. It has been also reported that it has shifted southward over the past two decades (Qiu and Chen 2010; Qiu and Chen 2012), in response to the strengthening of the atmospheric Walker circulation (Tanaka et al. 2004; Mitas and Clement 2005).

The California Current is the eastern boundary current of the subtropical gyre and flows southward in the eastern subtropical gyre. This current carries the North Pacific Central Water transported by the North Pacific Current and parts of relatively low salinity and temperature water advected by southward coastal currents which originates from the eastern subpolar gyre (Marchesiello et al. 2003). A recent study showed that the California Current has an important influence on the formation and interannual variability of the North Pacific Intermediate Water and the eastern subtropical mode water (ESTMW) from an analysis of Argo profiling data and repeat ship observations (Auad et al. 2011).

The surface circulation of the North Pacific subtropical gyre is basically driven by the surface wind. The salinity in the Pacific is lower than that in the other ocean basins because of the zonal transport of the fresh water from the Atlantic to the Pacific (Talley et al. 2011). This low-salinity water tends to inhibit the formation of the thermohaline circulation. Therefore, the North Pacific has been considered to be ideal for studying the

wind-driven surface circulation from an observational point of view (Hautala et al. 1994; Aoki and Kutsuwada 2008).

## 1.2 Sverdrup theory

The North Pacific subtropical gyre is mainly driven by the northeasterly trade winds on the southern side of the subtropical gyre and the westerlies on the northern side. The sea surface winds directly exert influence on a thin surface layer at depths of several ten meters, known as the Ekman layer. Ekman (1905) described that the velocity in the Ekman layer should have a spiral structure and the Ekman transport vertically integrated over the Ekman layer is $\tau/f\rho$ at an angle of 90° to the right of the wind in the North Hemisphere. Here $\tau$ is the wind stress, $\rho$ is the water density, $f$ is the Coriolis parameter. For the subtropical region, the surface wind system with the northeast trade winds to the south and the westerlies to the north generates the northward and southward Ekman transports, respectively. These transports result in the convergence of the Ekman transport, and give rise to the downward Ekman pumping. The divergence of the Ekman transport is obtained by vertically integrating the continuity equation over the Ekman layer as follows:

$$\begin{aligned} w_{EK} &= \frac{\partial U_E}{\partial x} + \frac{\partial V_E}{\partial y} \\ &= \frac{\partial}{\partial x}\left(\frac{\tau^y}{\rho f}\right) - \frac{\partial}{\partial y}\left(\frac{\tau^x}{\rho f}\right) = \mathbf{k}\cdot\nabla\times\left(\frac{\boldsymbol{\tau}}{\rho f}\right), \end{aligned} \tag{1-1}$$

where $U_E$ and $V_E$ is the zonal and meridional Ekman transport, respectively, $\boldsymbol{\tau}$ is the wind stress vector $\boldsymbol{\tau} = (\tau^x, \tau^y)$ and $\mathbf{k}$ is a unit vector in the local vertical direction. This equation indicates that the Ekman pumping velocity can be mainly expressed as wind stress

curl. As shown later, the vertical velocity plays a key role in connecting surface frictional forcing by winds with the large-scale ocean circulation.

The wind-driven circulation theory was first developed in the late 1940s by Sverdrup (1947), Stommel (1948) and Munk (1950). Sverdrup (1947) showed the simple relationship between the sea surface wind stress curl and the circulation in the interior ocean away from the coasts. Because of the Ekman downwelling of the subtropical gyre, the water columns below the Ekman layer in the interior ocean shrink and therefore move equatorward in order to conserve potential vorticity (PV) $f/h$, where $h$ is the layer thickness and the relative vorticity is neglected because it is much smaller than $f$ in the interior ocean. Mathematically, the derivation of the ocean transport is derived from the momentum equations and the continuity equation for the homogeneously single layer in which the motion is exactly two-dimensional and incompressible, as follow:

$$\frac{du}{dt} - fv = -\frac{1}{\rho}\frac{\partial p}{\partial x} + A_H\left(\frac{\partial^2 u}{\partial x^2} + \frac{\partial^2 u}{\partial y^2}\right), \tag{1-2a}$$

$$\frac{dv}{dt} + fu = -\frac{1}{\rho}\frac{\partial p}{\partial y} + A_H\left(\frac{\partial^2 v}{\partial x^2} + \frac{\partial^2 v}{\partial y^2}\right), \tag{1-2b}$$

$$0 = \frac{\partial p}{\partial z}, \tag{1-2c}$$

and

$$\frac{\partial u}{\partial x} + \frac{\partial v}{\partial y} + \frac{\partial w}{\partial z} = 0, \tag{1-3}$$

where $u$, $v$ and $w$ are the zonal, meridional and vertical velocities, $A_H$ is the horizontal turbulent viscosity coefficient, and $p$ is the pressure. Cross-differentiating the Eqns. (1-2a,b) and eliminating the pressure gradient terms using the continuity equation (1-3) lead to the vorticity equation on the $\beta$ plane:

$$\frac{d\zeta}{dt} + \beta v = f\frac{\partial w}{\partial z} + A_H \nabla^2 \zeta , \tag{1-4}$$

where $\zeta$ is the relative vorticity. Integrating the Eq. (1-4) over the thickness of the geostrophic interior $D$ that is the ocean depth with a slight approximation:

$$\frac{d\zeta}{dt} + \beta v = \frac{f}{D}(w_{EK} - w_B) + A_H \nabla^2 \zeta , \tag{1-5}$$

where $\beta$ is the meridional gradient of the Coriolis parameter, $w_B$ is the velocity pumped out of the lower boundary layer. The Eq. (1-5) is rewritten by substituting the vertical velocity at the lower boundary layer [$w_B = \delta_E \zeta/2$] and expanding the material derivative of the relative vorticity as

$$\frac{\partial \zeta}{\partial t} + u\frac{\partial \zeta}{\partial x} + v\frac{\partial \zeta}{\partial y} + \beta v = \frac{f}{D} w_E - f\frac{\delta_E}{2D}\zeta + A_H \nabla^2 \zeta , \tag{1-6}$$

where $\delta_E$ is the lower boundary layer thickness. The first term of the left-hand side is the time-dependent term of the relative vorticity. The second and third terms on the left side are referred as the advection terms of the relative vorticity. The second term on the right side represents the effect of the vorticity change due to vortex stretching produced by the vertical velocity at the bottom boundary layer, which is referred the bottom friction term, and the third term indicates the effect of the lateral diffusion of the vorticity. Here, because the surface Ekman pumping is much larger than that caused by the bottom friction, the second term of the right hand side can be neglected and the effect of the advection and lateral diffusion are negligible and for steady flow at the interior ocean, Eq. (1-6) is reduced to:

$$\beta V = f w_E , \tag{1-7}$$

where $V$ is the depth-integrated meridional velocity. This equation is called the Sverdrup relation. The equatorward transport must be returned to the north because of the conser-

vation of the mass. Stommel (1948) and Munk (1950) explained how the return flow have to develop along the western boundary in term of the bottom and lateral frictions, respectively.

Many previous studies have attempted to verify the Sverdrup theory. In the North Pacific, the verification of the Sverdrup theory was done by Hautala et al. (1994), who compared the geostrophic transport estimated from zonal hydrographic section along 24°N conducted in the the World Ocean Circulation Experiment (WOCE) cruise with the Sverdrup transport computed from ship-observed surface winds of the Comprehensive Ocean-Atmosphere Data Set (COADS). They showed that the Sverdrup balance is almost valid in the entire ocean basin. Their results were further confirmed by Aoki and Kutsuwada (2008) from an analysis of several different wind stress products and historical hydrographic data from the World Ocean Database 2005 (Boyer et al. 2006). The time-varying Sverdrup balance has also been examined by a number of studies (e.g., Sekine and Kutsuwada 1994; Kubota et al. 1995; Chelton and Mestas-Nuñez 1996). Although these studies have demonstrated that the barotropic geostrophic transports can be explained by the Sverdrup theory, they have not yet investigated the horizontal structure of the subtropical gyre in detail based on the Sverdrup theory.

## 1.3 Ventilated thermocline theory

While the Sverdrup theory provides a basic picture of barotropic wind-driven circulation, the ventilated thermocline theory (Luyten et al. 1983) and the theory of the PV homogenization for an unventilated thermocline (Rhines and Young 1982; Young and Rhines 1982) brought insights on the baroclinic structure of the ocean. According to their theories, the subtropical region is classified into the three characteristic regions; the ven-

tilated region, the western unventilated pool region and the eastern shadow zone (Fig.1-3). These regions are different in the dynamical process. In the ventilated region, the sea surface water is subducted from the base of mixed layer into the thermocline, advected by the Sverdrup flow along isopycnal surfaces, preserving the PV during the subduction. The water partly re-emerges to the surface in late winter when it is entrained by deep mixed layer. Therefore, the water subducted into the thermocline retains the water properties of the late winter mixed layer (Stommel 1979). The western unventilated pool region is defined as the region bounded on the east by subsurface streamlines that only outcrop at the outer western edge of the interior. The pool is a region of homogenized PV. The eastern shadow zone is the region between the easternmost subducted streamlines and the eastern boundary. The water of this region is not ventilated. Indeed, an oxygen at 600-800m depth in the region is lowest in the North Pacific subtropical gyre (Talley 2007).

The streamlines at the upper and lower layers from the two layer model based on the ventilated thermocline theory are shown in Figure 1-4, indicating that the streamlines at the lower layer in the ventilated region are twisted clockwise with respect to the streamlines in the upper layer. That is, the velocity vector spirals clockwise with increasing depth in the subtropical gyre. This feature has been confirmed in the real ocean and is called the $\beta$-spiral (Stommel and Schott 1977). The $\beta$-spiral is essentially caused by the conservation of the PV. Let us consider the two layer model ocean for the North Pacific subtropical gyre (Fig. 1-5). Because the water column in the lower layer moves southward due to the Sverdrup flow, the water column shrinks in order to satisfy the conservation of the PV. Therefore, the boundary between the upper and lower layers slopes toward the south. This slope implies that there must be the eastward shear of the upper layer. Therefore, the velocity spirals clockwise with depth. As mentioned above, the $\beta$-spiral

results from the PV conservation and thus is a crucial characteristic of the ventilated thermocline theory.

Talley (1985) applied the ventilated thermocline model proposed by Luyten et al. (1983) to the North Pacific and discussed the formation of shallow salinity minimum in the subtropical gyre. Huang and Qiu (1994) showed a subduction rate for the North Pacific from an analysis of the wind-driven circulation using Levitus (1982) climatology. The subduction rate was discussed from comparison with that estimated from an ideal-fluid thermocline model with continuous stratification by Huang and Russell (1994) and was further investigated by analyzing latest ocean climatology (Suga et al. 2008) and numerical simulations from eddy-resolving ocean general circulation models (e.g., Qu et al. 2002; Tsujino and Yasuda 2004; Qu and Chen 2009; Nishikawa et al. 2010). Although these studies have advanced our understanding of three-dimensional structures of the subtropical gyre, they have not adequately referred to the spatial structure of the ocean circulation, because they focus on subduction processes and rates rather than on gyre structures.

## 1.4 Scope of this thesis

As has been mentioned above, it is still not clear that the detailed consistency between the surface circulation and the Sverdrup theory in terms of the horizontal structure of the circulation. In addition, since the vertical structure of the North Pacific subtropical gyre also has not been adequately examined so far, particularly with a focus on the PV conservation. The purpose of this study is to understand the mean three dimensional structures of the North pacific subtropical gyre and their temporal variations and to reveal the underlying physical processes for the mean field and temporal variations.

In Chapter 2, the mean structures of the North Pacific subtropical gyre are investigated using Argo float observations and several wind stress products. I will focus on the gyre axis (Qu 2002), which is defined as a large-scale boundary between eastward motions on the northern part of the subtropical gyre and westward motions on the southern part. The gyre axis of the depth-integrated geostrophic circulation is compared with of the wind-driven circulation in detail, and then the consistency between them is examined in detail. Then I show the structures of the gyre axis with depth and discuss the relationship with the structures of velocity and PV.

In Chapter 3, using two different Argo gridded datasets and two wind stress products, I investigate the temporal variations of the depth-integrated geostrophic circulation and the vertical structures of geostrophic circulation in the North Pacific subtropical gyre, especially focusing on the eastern subtropical gyre. The periodicity and spatial characteristic of the variations are examined in detail and then I discuss the relationship with the wind forcing. I also describe year-to-year variations of the vertical structures of the gyre axis. General conclusion is given in Chapter 4.

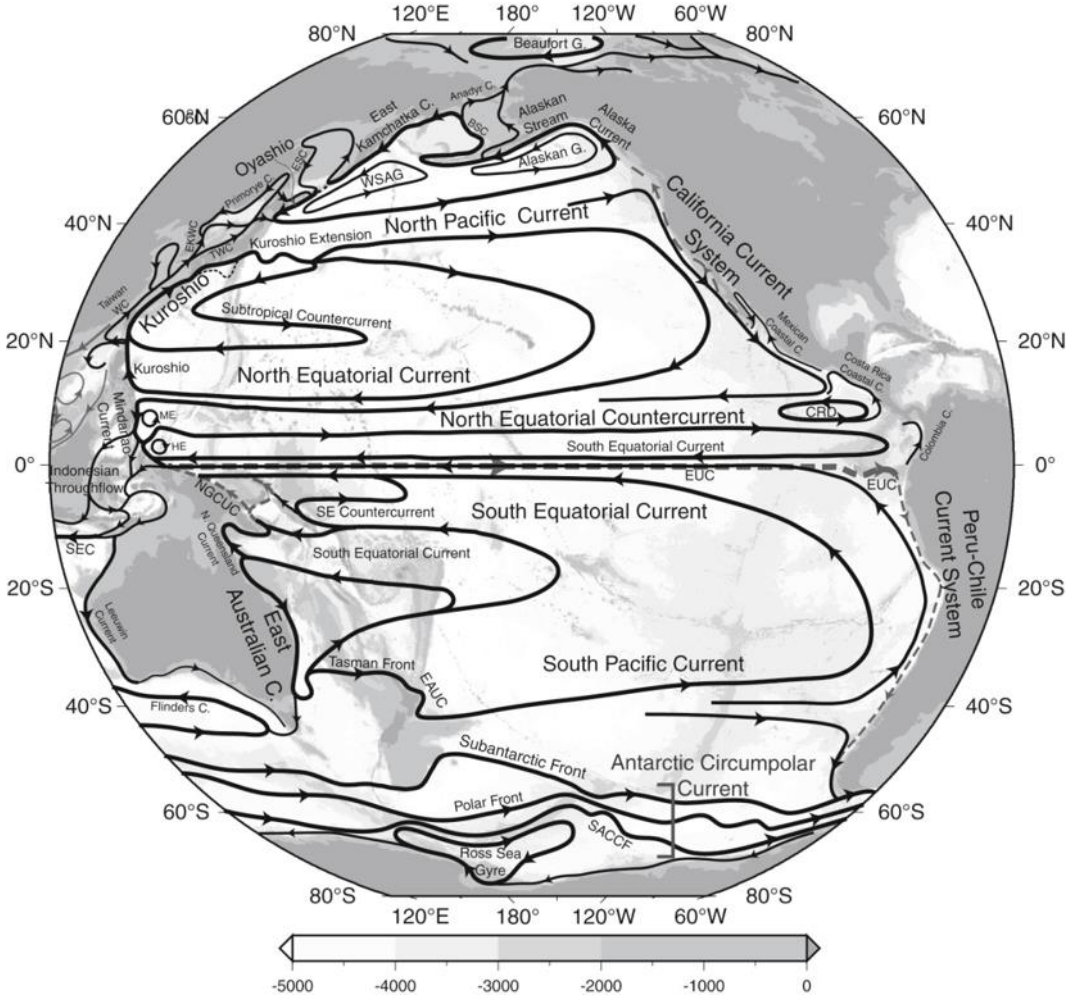


Fig.1-1. Schematic map of the surface current in the Pacific, cited from Talley et al. (2011).

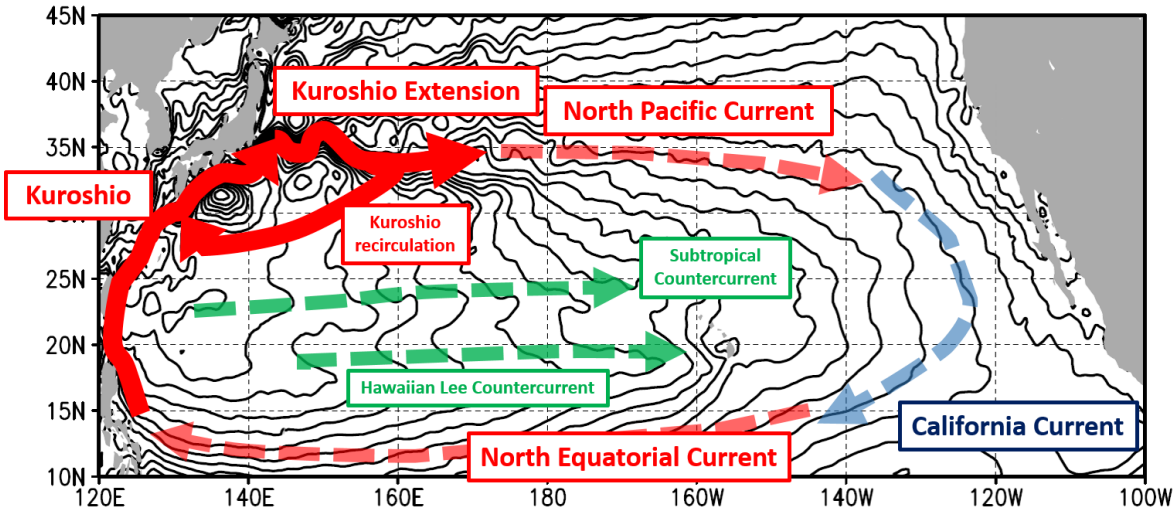


Fig.1-2. Schematic map of the surface currents in the North Pacific subtropical gyre. Counters show the mean sea surface height based on satellite observations.

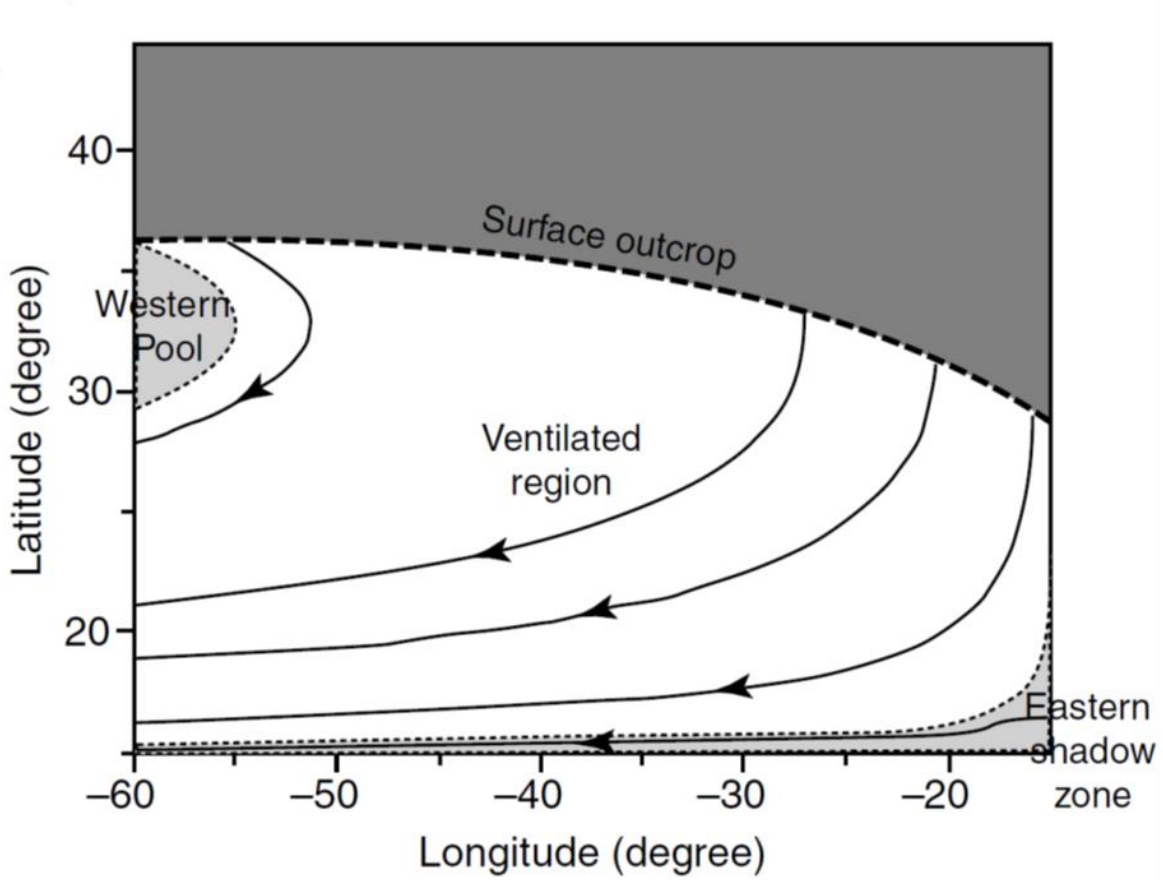


Fig.1-3. Schematic diagram of the streamlines for an idealized subduction on an isopycnal surfaces, cited from Talley et al. (2011) after Williams (1991).

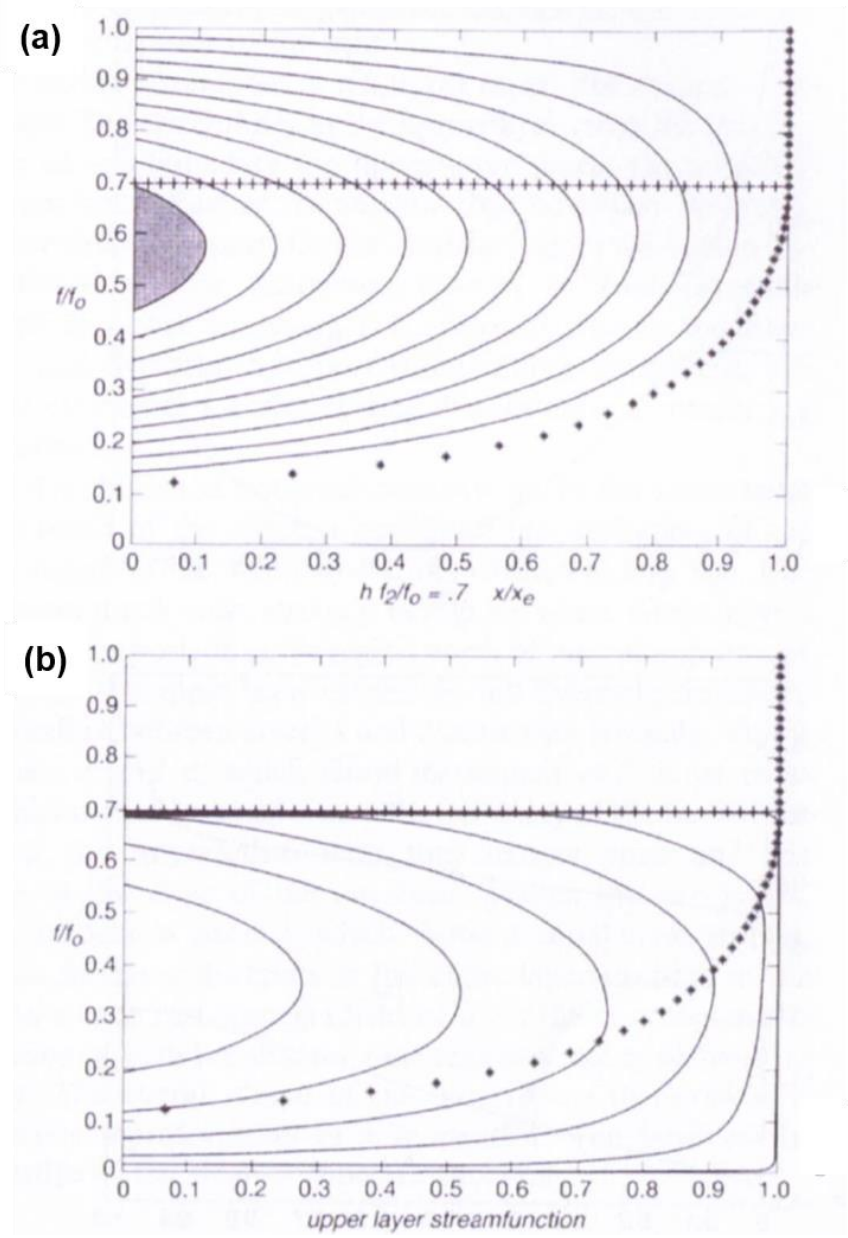


Fig.1-4. Streamline maps at (a) the lower layer and (b) upper layer of the two layer model based on the ventilated thermocline theory (Pedlosky 1996). The cross and asterisks symbols show the outcrop line and the boundary between the ventilated region and the eastern shadow zone, respectively. The shaded region denotes the western unventilated pool region.

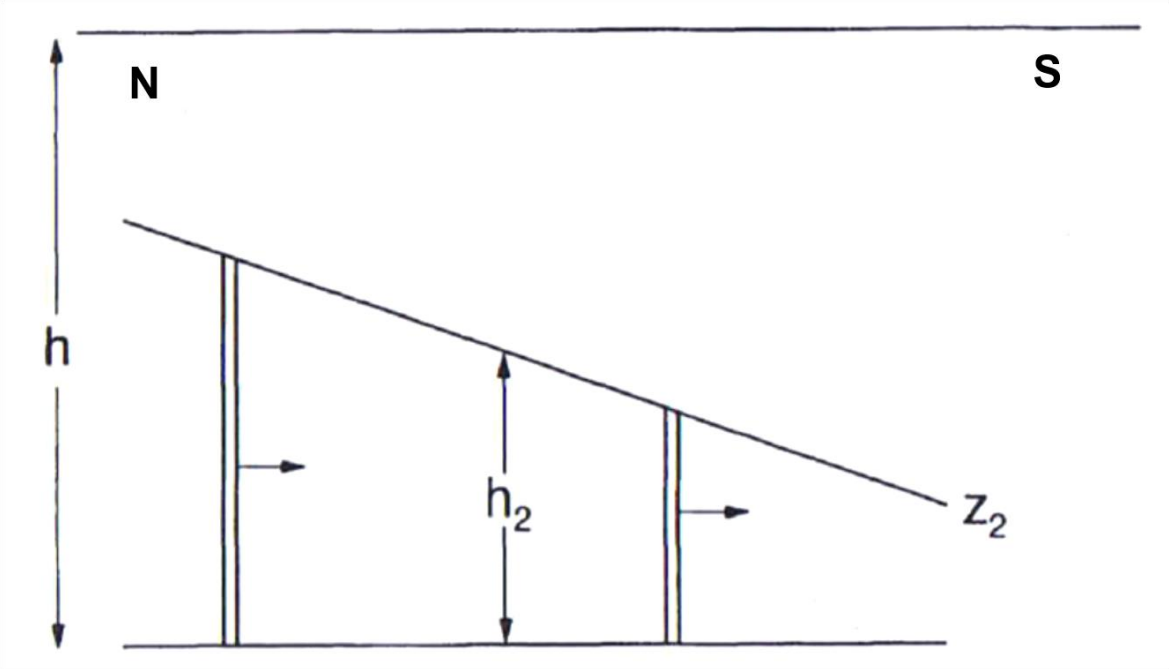


Fig.1-5. Schematic meridional vertical section of the fluid column in the lower layer (Pedlosky 1996).

The right-hand side is the south.

# Chapter 2
# Mean structures of the North Pacific subtropical gyre

## 2.1 Introduction

The subtropical gyre of the North Pacific is a large-scale anticyclonic circulation approximately between 15°N and 45°N. It is basically driven by the northeast trade winds and the westerlies, as explained by a classical wind-driven circulation theory that was developed by some pioneering work by Sverdrup (1947), Stommel (1948) and Munk (1950). Sverdrup (1947) showed the Sverdrup balance in the interior ocean, where depth-integrated geostrophic circulations are related to surface wind stress curl. The Sverdrup circulation is set up by barotropic Rossby waves propagating across the ocean.

The validity of the Sverdrup balance was investigated in the North Pacific by Hautala et al. (1994), who analyzed ship-observed surface wind and hydrographic observations of a zonal section along 24°N and showed that the Sverdrup balance is almost valid in the entire ocean basin. Their results were further confirmed by Aoki and Kutsuwada (2008) from an analysis of several different wind stress products and historical hydrographic data. Since the barotropic adjustment time is less than a month for the North Pacific subtropical gyre, the circulation is considered to equilibrate with a wind forcing on seasonal and longer time scales. The time-varying Sverdrup balance has also been examined by a number of studies (e.g., Sekine and Kutsuwada 1994; Kubota et al. 1995; Chelton and Mestas-Nuñez 1996).

While the Sverdrup theory provided a basic picture of barotropic wind-driven circulation, the ventilated thermocline theory (Luyten et al. 1983) and the theory of the PV homogenization for an unventilated thermocline (Rhines and Young 1982; Young and

Rhines 1982) brought insights on baroclinic structure of the ocean. From an observational point of view, large-scale aspects on structures of geostrophic circulation were examined in the North Pacific subtropical gyre by Qu (2002). He defined the axis of the subtropical gyre as the meridional maximum of depth-integrated dynamic height and Sverdrup transport using climatologies from World Ocean Atlas 1998 and Hellerman and Rosenstein's (1983) surface wind. Their axes both appear along 30°N and extend almost zonally, showing a good agreement in position. He further examined the vertical structure of the axis from dynamic heights at each depth, reporting that the gyre axis moves poleward gradually with depth from 25°N at 100 m to 38°N at 800 m depth in the central and eastern basin east of 180°, but in the west it does not change significantly and almost stays at 30°N. The northward shift of the gyre has also been reported by other observational studies (Reid and Arthur 1975; Huang and Qiu 1994; Kobashi et al. 2006) and numerical models (Nakano and Suginohara 2002). Because the northward shift of the gyre is essentially related to $\beta$-spiral caused by the conservation of PV of the gyre circulation (Stommel and Schott, 1977), it is a crucial characteristic of the ventilated thermocline theory. Nevertheless, the relationship between the gyre shift and the structure of PV has not been investigated from observations in detail so far.

The northward shift of the gyre is considered as a key structure for the formation of the eastern Subtropical Countercurrent (STCC), which is a shallow eastward current around 26°N between 180° and 160°W (Kobashi et al. 2006). The eastern STCC is basically maintained by the central mode water (CMW), a vertically homogeneous water mass characterized by low PV in the central subtropical gyre (Nakamura 1996; Suga et al. 1997). The CMW forms in wintertime deep mixed layer near the Kuroshio Extension, subducted into the thermocline and advected by gyre circulation. Lighter and denser parts of the CMW diverge from the formation site and circulate along the inner and outer paths

of the subtropical gyre, respectively, due to the northward retreat of the gyre of denser isopycnals (Oka and Suga 2005; Kobashi et al. 2006). They again encounter in the central subtropical gyre, piling up in the vertical and forming low PV pool (Kubokawa 1999; Kubokawa and Inui 1999). This pool can heave an overlying thermocline, causing subsurface temperature fronts and thus generating shallow STCC through the thermal wind relation. The STCC is known to affect surface winds and precipitation through its thermal effects (Kobashi et al. 2008; Xie et al. 2011). Detailed knowledge of structure of the subtropical gyre would help to understand variability of STCC and its influences on the atmosphere (Kobashi and Kubokawa 2012).

The present study examines the mean structures of the North Pacific subtropical gyre with a particular focus on the gyre axis, using Argo float observations and wind stress data from several reanalysis and satellite products. I describe the gyre axis in a different way from Qu (2002) to show a detailed picture of the gyre axis and its relationship with the Sverdrup balance and the ventilated thermocline theory. Our study identifies differences between the regions east and west of about 180°. Distinct from the west where the gyre axis is strongly affected by the Kuroshio Extension jet and its recirculation gyre, the east shows some consistency with features expected from the Sverdrup balance and the ventilated thermocline theory. I find two gyre axes in the east that are associated with a local cyclonic wind stress curl anomaly. I also show that a northward shift of the gyre axis with depth, which is a prominent feature in the east as shown by Qu (2002), occurs non-uniformly in the vertical, due to the presence of the CMW and the pycnocline. The results present an important dynamical effect of the CMW on large-scale circulations of the subtropical gyre.

The rest of this chapter is organized as follows. Section 2.2 describes the data used and the method employed to determine the gyre axis. In Section 2.3, the relationship be-

tween the wind-driven Sverdrup circulation and the depth-integrated geostrophic circulation is shown. The vertical structure of the gyre axis is examined in Section 2.4. Section 2.5 gives summary and discussion.

## 2.2 Data and methods

### 2.2.1 Geostrophic circulation

This study uses monthly temperature and salinity data from 2001 to 2011 from Grid Point Value of the Monthly Objective Analysis using Argo float data (MOAA GPV) produced by Hosoda et al. (2008). This product is based on Argo float data, the Triangle Trans-Ocean Buoy Network (TRITON) and available conductivity-temperature-depth (CTD) profilers, optimally interpolated at standard pressure levels from 10 to 2000 dbar on a 1° grid in space.

Dynamic heights are calculated at each depth referenced to 2000 dbar from the monthly MOAA GPV. For the comparison with geostrophic transports expected from surface wind stress curl, depth-integrated dynamic heights are also computed by integrating dynamic heights between the surface and 2000 dbar. These maps of dynamic heights are all smoothed with a 13-month running mean to remove seasonal variations, and then are used to obtain geostrophic velocity. Note that our results are not sensitive to the choice of the reference level. If another commonly used level of 1000 dbar is adopted, our results do not change significantly (not shown).

The Argo float observations in the North Pacific are quite sparse until 2004, and thus the MOAA GPV before 2005 is considered almost the same as the World Ocean Atlas climatology that is a first-guess value in the optimal interpolation (Hosoda et al. 2008). I

conducted the same analysis using the data from 2005 to 2011 and found that the distribution of the gyre axis is almost the same as those from 2001 to 2011.

### 2.2.2 Wind-driven transport

I analyzed six products of monthly-mean surface wind stress data: Japanese 25-year Reanalysis (JRA; Onogi et al. 2007), Japanese Ocean Flux Data Sets with Use of Remote Sensing Observations (J-OFURO; Kubota et al. 2002), National Centre for Environmental Prediction (NCEP)/National Center for Atmospheric Research (NCAR) reanalysis (NCEP1; Kalnay et al. 1996), NCEP/Department of Energy (DOE) reanalysis (NCEP2; Kanamitsu et al. 2002), the Modern-Era Retrospective Analysis for Research and Applications (MERRA; Rienecker et al. 2011) and Hellerman and Rosenstein's (1983) data (HR). The period analyzed in this study is the same as that of the MOAA GPV, but the J-OFURO covers only from 2001 to 2008 and the HR is monthly climatology from 1870 to 1976. The JRA covers the period until 2004, but continues to be updated for the subsequent period using the same assimilation system, the Japan Meteorological Agency (JMA) Climate Data Assimilation System (JCDAS). The specification of the products is summarized in Table 2-1.

Sverdrup balance in response to surface Ekman convergence is expressed as

$$\int_{x_e}^{x}\int_{-h}^{0} v_G \, dz \, dx = \frac{f}{\beta}\int_{x_e}^{x} w_{EK} \, dx, \qquad (2\text{-}1)$$

where $x_e$ is the eastern boundary, $v_G$ is the meridional geostrophic velocity at each depth, $f$ is the Coriolios parameter, $\beta$ is the meridional gradient of the Coriolis parameter, $h$ is the depth of wind-driven flow, and $w_{EK}$ is the Ekman pumping velocity. Here I assume that vertical velocity at a depth of bottom of wind-driven flow is negligible. This equa-

tion is rewritten by substituting the Ekman pumping velocity ($w_{EK}=\mathbf{k}\cdot\nabla\times(\boldsymbol{\tau}/f\rho)$) as

$$\int_{x_e}^{x}\int_{-h}^{0} v_G \, dz \, dx = \frac{1}{\beta\rho}\int_{x_e}^{x} \mathbf{k}\cdot\nabla\times\boldsymbol{\tau} \, dx + \frac{1}{f\rho}\int_{x_e}^{x} \tau^x \, dx, \qquad (2\text{-}2)$$

where $\rho$ is the density, $\boldsymbol{\tau}$ is the wind stress vector $\boldsymbol{\tau} = (\tau^x, \tau^y)$, and $\mathbf{k}$ is a unit vector in the local vertical direction. In this study, I calculate the geostrophic transport from the right-hand side of Eq. (2-2), which I will refer to as the wind-driven transport following the term used by Aoki and Kutsuwada (2008). I also refer to the circulation associated with the wind-driven transport as the wind-driven circulation henceforth.

The Ekman pumping velocity is smoothed in space and time. The MOAA GPV used to derive geostrophic circulation is spatially smoothed by an optimal interpolation with a meridional decorrelation scale of about 3° to 4° around 30°N at depths of 200 to 400 m (Hosoda et al. 2008), though it is slightly different at locations and depths. To match the resolution, the monthly Ekman pumping velocity except for that from relatively coarse-resolution NCEP1, NCEP2 and HR is smoothed meridionally by a 3° moving average. This procedure filters out features with scales less than about 300 km. Then, the monthly maps of the wind-driven transport are smoothed with 13-month running mean to remove seasonal variations. Regarding the HR, I look at only annual mean wind-driven transport.

### 2.2.3 Gyre axis

In this study, the gyre axis is defined as the large-scale boundary between eastward motions on the northern part of the subtropical gyre and westward motions on the southern part of it. The gyre axis is calculated from the maps of geostrophic circulation and wind-driven transport.

The climatological positions of the gyre axis, which are the main target of the present study, are determined from the rate of the appearance of the gyre axis. The gyre axis is first detected from each monthly map and then it is counted at each grid over the analysis period, which will be shown as the percentage. I regard a band with the high percentage as the climatological gyre axis. It should be noted that this climatological gyre axis does not necessarily correspond to a boundary between eastward motions to the north and westward motions to the south at the time mean maps. I will make a brief comparison with the gyre axis of the time mean maps. For the wind-driven transport calculated from the HR, because it is a long-term mean data (Table 2-1), the gyre axis is calculated only from the mean map.

In comparison with Qu (2002), who defined the gyre axis as the meridional maximum of mean Sverdrup transport and dynamic heights, the present study cannot exclude the existence of multiple axes and thus may be able to capture the structure of the subtropical gyre in detail.

The result, however, should be carefully discussed, because our method is sensitive to tiny spatial variations of zonal velocity and transport. The present study assessed the statistical significance of the climatological gyre axis. By adopting the bootstrap method (Press et al. 1992), I generate 1000 maps of the appearance rate of the gyre axis. At each grid point, I first merged the time series of zonal velocity/transport with those from meridionally adjacent two grid points, which are used to define the gyre axis at each map, and then resampled the data to make 1000 datasets using the bootstrap technique on the assumption that all the data are independent. Using this new data, I calculated the appearance rate of the gyre axis in the same way from each dataset and then determined the 95 and 90 percentile confidence levels. I checked if the appearance rate from the original data exceeds their confidence levels at each grid.

In addition to the statistical assessment, I further looked at the effect of small-scale variations such as eddies on the climatological gyre axis. To highlight large-scale structures of zonal velocity/transport, I calculated the gyre axis from a polynomial curve fitting to the monthly meridional profiles and then determined the climatological gyre axis. I will compare the result with the original one.

Although the climatological gyre axis in the present study has some weakness as mentioned above, the statistical assessment and the additional analysis will support the meaningfulness of our gyre axis. We believe that the gyre axis is useful for describing structures of the ocean circulation.

## 2.3 Vertical-integrated geostrophic circulation

Figure 2-1 shows the mean depth-integrated dynamic height and the rate of the appearance of the gyre axis. In the western basin, the climatological gyre axis is recognized from a zonal band of significant high percentages along about 30°N. The location of the gyre axis is consistent with the result of Qu (2002). On the other hand, in the east of 170°W, there are two meridional mounds of high percentages around 25°N and 30°N, suggesting two gyre axes. These two gyre axes are significant at the 95 percentile confidence level. The northern axis looks like it is connected to the western gyre axis. Although these two gyre axes may be obscure in the mean depth-integrated dynamic height map, the depth-integrated dynamic height tends to take some local peaks or be uniform in the meridional direction, and therefore the axis defined from the mean map (marked by open circle symbols in Fig. 2-1) displays one gyre axis with somewhat unnatural discontinuity around 155°W.

Figure 2-2a shows the appearance rate of the gyre axis, the same as in Fig. 2-1, but calculated from a 5th order polynomial curve fitting to a monthly meridional profile of depth-integrated dynamic heights in the latitude range of 20°~35°N at each longitude, in order to highlight large-scale structures. Figure 2-2b indicates the mean contribution ratio, which represents the extent to which each fitting of 2nd to 6th order polynomials explains the original profile of depth-integrated dynamic heights. As seen from Fig. 2-2a, the polynomial fitting can capture almost the same two gyre axes between 165°W and 150°W as in Fig. 2-1. They are obvious from the fitting with more than 4th order (not shown). The northern axis, however, disappears to the east of 150°W, where the contribution ratio decreases slightly to the east (Fig. 2-2b), suggesting the importance of higher-order terms there. Because the appearance rate of the gyre axis from the original data is statistically significant there (Fig. 2-1), the northern axis east of 150°W may be associated with relatively small-scale but persistent geostrophic circulation.

The existence of the two gyre axis in the east is also supported by the relative vorticity calculated from a depth-averaged mean geostrophic velocity between the surface and 2000 m. Figure 2-3 shows the zonal averages of the relative vorticity between 165°W and 130°W, revealing significant cyclonic rotation anomaly with positive curl around 28.5°N between the two gyre axes, embedded in the background of basin-scale anticyclonic circulation of the subtropical gyre.

The two climatological gyre axes are also seen from the wind-driven transport with some notable differences. Figure 2-4 shows the mean wind-driven transport and the appearance rate of the gyre axis. The MERRA that has the most fine grid interval (Table 2-1) displays several bands of high percentage (Fig. 2-4e). The two high-percentage bands are evident around 26°N and 32°N. They extend from off the west coast of the North America to the west across the basin, and seem to merge together near 140°E.

These two bands are also seen roughly from the gyre axis calculated from the mean wind-driven transport map (circle symbols in Fig. 2-4e). Figure 2-5 shows the percentile of the appearance rate of the gyre axis, which was assessed from the bootstrap method (Section 2.3). The southern band around 26°N is significant at the 90 percentile confidence level. The northern band is also significant to the east of 170°W mostly at the 90 percentile confidence level, though the percentile decreases to about 50~75 percentile to the west. The low percentile in the west could imply high variability of the gyre axis within the band. The two bands are also obvious from the appearance rate map calculated from a 4th order polynomial fitting (not shown).

These two bands are common in the J-OFURO (Figs. 2-4b), and are partly identifiable from the JRA and the lower-resolution NCEP1 and NCEP2 (Figs. 2-4a,c,d), though their latitudinal positions are slightly different probably due to the different grid spacing (Table 2-1). In the J-OFURO (Fig. 2-5b), the northern band shows the percentile of about 70~90% around 30°N to the west of 155°W. The northern band in the JRA is mostly significant at the 80 percentile confidence level except the area between 180° and 145°W (Fig. 2-5a) and is also partly visible from the mean wind-driven transport map (circles in Fig. 2-4a). The NCEP1 and NCEP2 display a high percentile exceeding 90% at the northern band around 33°~34°N. In addition, as shown by Qu (2002), the northern band is also evident from the mean map of the HR (Fig. 2-4f). These features may support the existence of the northern band.

The southern band from the J-OFURO, JRA, NCEP1 and NCEP2 is overall significant at the confidence levels between 80 and 95 percentiles (Fig. 2-5). There are some noticeable differences in distribution. The southern band east of 155°W is found around 22.5°N in the JRA and NCEP2, which is located further to the south as compared to that of the MERRA. The similar southern band is also seen in the HR, which might result

from the contamination of the band around 26°N and another southeast-slanted band extending from 24°N to 19°N in the MERRA (Fig. 2-4e).

These discrepancies among the datasets might be attributable to various factors such as the differences in resolution and assimilation method adopted by the reanalysis products and what kind of observation data they used, but identifying their causes is beyond the scope of this study. Although there are discrepancies among the datasets, all the products strongly suggest that wind over the North Pacific tends to produce two gyre axes in the wind-driven circulation, so we consider that they would deserve to be compared with the ocean gyre axis calculated from the gridded Argo data.

Other bands of high percentages are seen from the MERRA near 35°~40°N to the east of 155°W and near 17°N to the west of the Hawaiian Islands. The similar bands may be recognized from the other datasets except for the HR. The first bands east of 155°W are located at the northeast corners of the subtropical gyres. The second band is associated with a local response of wind stress curl to the Hawaiian Islands (Xie et al. 2001). Therefore, these bands are considered distinct from a large-scale gyre axis of the subtropical gyre, which is the target of the present study.

Figure 2-6 shows the histograms of the appearance rate of the gyre axis against latitude, zonally averaged between 150°E and 170°E and 170°W and 150°W, together with the zonal averages of the depth-integrated dynamic height (Figs. 2-6a,b) and the wind-driven transports (Figs. 2-6c-l). In the eastern basin (Figs. 2-6b,d,f,h,j,l), the two peaks of the appearance rate in the depth-integrated dynamic height around 25°N and 30°N are roughly collocated with those of the wind-driven transports from the JRA, J-OFURO and MERRA, though the ocean gyre axes both lie slightly to the south. The collocation of the two gyre axes indicates a good correspondence between the geostrophic circulation and the wind-driven circulation.

In the western basin, except for the NCEP1, the gyre axes of the depth-integrated dynamic height and the wind-driven transports are commonly present at the same latitude around 30°N, where their zonal averages both show a meridional peak (Figs. 2-6a,c,e,g,i,k). The wind-driven transport from the JRA and the J-OFURO as well as the MERRA shows another peak of the percentage around 26°N, as seen from Fig. 2-4, but there seem to be no ocean gyre axis equivalent to it, suggesting some discrepancy with the wind-driven circulation.

The rate of the appearance of the gyre axis does not necessarily tell that the two gyre axes exist at the same time. Although the temporal variability of the gyre axes is beyond the purpose of the present study, I briefly examined the rate of the appearance of the northern (southern) gyre axis, by counting at each longitude from the monthly maps if there is at least one gyre axis between 23°N (28°N) and 28°N (33°N) for the depth-integrated dynamic heights and between 24°N (29°N) and 29°N (34°N) for the MERRA-derived wind-driven transports (not shown). The results show that the percentage of all the gyre axes exceeds 50% in the region east of 165°W. The zonally-averaged percentage of the northern and southern gyre axes between 165°W and 140°W are 62 % and 69% for the ocean geostrophic circulation and 64% and 77% for the wind-driven circulation, respectively. These rates are roughly comparable to each other between the geostrophic circulation and wind-driven circulation.

What causes the two gyre axes in the eastern basin? Figure 2-7 shows the mean maps of wind-driven transport, Ekman pumping velocity and wind stress vector from the MERRA. The Ekman pumping velocity is relatively weak around 125°W between the two gyre axes at 25°N and 32°N, suggesting a cyclonic anomaly of wind stress curl. The high-pass filtered maps with a running average of 10° width (Fig. 2-7b) clearly show a cyclonic wind anomaly with a positive Ekman pumping velocity anomaly. It has the cen-

ter around 125°W, and extends with weak cyclonic anomalies to the west around 150°W. This cyclonic wind anomaly is responsible for the formation of the two gyre axes across the subtropical gyre, because if I calculate the wind-driven transport by integrating Eq. (2-2) from 160°W instead of the eastern boundary, the two gyre axes disappear but one gyre axis remains around 30°N (not shown).

The area of the cyclonic wind anomaly is dominated by northeasterly winds blowing from the subtropical high (Fig. 2-7a). High-passed wind stress vectors (Fig. 2-7b) indicate that the cyclonic wind curl anomaly is maintained by local southeasterly wind anomalies, which are probably associated with local weakening of the northeasterly winds. These features are common in the JRA and J-OFURO (not shown).

## 2.4 Vertical structure of geostrophic circulation

In this subsection, I investigate how the gyre axis of geostrophic circulation changes in position with depth, and then show how these changes are related to density structures of the subtropical gyre.

Figure 2-8 shows the mean dynamic heights and acceleration potentials together with the appearance rate of the gyre axis at different depths and isopycnal surfaces. The distribution of the appearance rate of the gyre axis is nearly unchanged even if it is calculated from 4th order polynomial fitting maps (not shown). The thick black line represents the climatological gyre axis, which basically traces the significant meridional peak of the high appearance rate of the gyre axis with zonal continuity taken into consideration between 140°E and 140°W. As shown later, the climatological gyre axis agrees nearly with the gyre axis based on the time mean map. The northward shift of the gyre axis with depth is quite obvious. Consistent with the results of Qu (2002), the northward shift oc-

curs markedly to the east of 180°, where the gyre axis moves to the north by more than 10° from 100 m to 800 m depths, while to the west it does not change significantly with depth and lies around 30°N at almost the same latitude of the gyre axis of the depth integrated geostrophic circulation. These features are also evident on isopycnal surfaces (Figs. 2-8d~f).

At a depth of 100 m, some significant bands with high percentage of the gyre axis are discernible around 18°N and 23°N in the western basin (Fig. 2-8a). They appear along the southern boundary of narrow eastward jets of the Hawaiian Lee Countercurrent (e.g., Qiu et al. 1997; Flament et al. 1998; Xie et al. 2001) and the northern STCC (e.g., Uda and Hasunuma 1969; Kobashi et al 2006). Because these jets are narrow and distinct from large-scale eastward motions of the subtropical gyre, they are not regarded as the gyre axis in the present study.

At a depth of 500m and a density surface of 1026.5 kg/m$^3$ (Figs. 2-8b,e), two bands of high percentage may be identified along about 27°N and 32°N to the east of 155°W. The northern band is an eastern part of the band extending from the west. As the northern band moves northward with depth, the southern band also seems to shift to the north around 33°N at 800m depth and 1027.2 kg/m$^3$ density surface (Figs. 2-8c,f), though it is not clear compared to the northern band. The two bands might be indicative of the relationship with those of the depth-integrated geostrophic circulation in the east. However, because the circulation at each depth level does not necessarily correspond to the depth-integrated circulation, further study will need to address their relationship. The present study focuses on the northern higher-percentage band. Some patchy high percentage areas are found south of 25°N at the deep level (Figs. 2-8c,f), which may be associated with alternating subthermocline zonal jets reported by Qiu et al. (2013).

Figure 2-9 shows the distribution of the gyre axes at different depths calculated

from the appearance rate of gyre axis and the mean dynamic height maps. The results are almost the same, illustrating a contrast between a large northward shift of the gyre axis to the east of about 180° and a similar but quite small shift to the west. The 180° roughly corresponds to the area where the depth-integrated geostrophic circulation shows the discrepancy with the wind-driven circulation to the west (Section 3.1).

The gyre shift can be seen more directly from meridional sections of zonal geostrophic velocity (Fig. 2-10). The high appearance rate of the gyre axis approximately follows the line of a zero zonal geostrophic velocity, indicating that the climatological gyre axis based on the appearance rate is almost in agreement with the gyre axis of the mean section. In the west at 160°E (Fig. 2-10a), the gyre axis lies just along the southern flank of a strong barotropic-like eastward jet of the Kuroshio Extension. On the other hand, it is located in a broad weak zonal flow in the east at 160°W (Fig. 2-10b).

The northward shift of the gyre axis is related to the conservation of PV of the gyre circulation (Stommel and Schott 1977). The conservation of PV gives rise to a decrease in the thickness of a water column to the south, which results in forming a clockwise spiral of geostrophic velocity vectors with increasing depth and thus causing the northward shift of the subtropical gyre. Figure 2-11 shows meridional sections of PV and potential density with the positions of the climatological gyre axis superimposed. Under the assumption of negligible relative vorticity, the PV is calculated between the adjacent depths as follows

$$PV = -\frac{f}{\rho}\frac{\Delta\sigma_\theta}{\Delta z}, \qquad (2\text{-}3)$$

where $\Delta\sigma_\theta$ is the potential density difference and $\Delta z$ is the depth interval. It is linearly interpolated into isopycnal surfaces with a 0.05 kg/m$^3$ interval. The meridional gradients of PV are also computed on isopycnal surfaces.

Two distinct mode waters characterized by low PV less than $2.0 \times 10^{-10}$ $m^{-1}s^{-1}$ are found around the climatological gyre axis at depths of 200-300 m at 160°E and 200~500 m at 160°W, which correspond to subtropical mode water (STMW; Masuzawa 1969) and CMW, respectively. The STMW and CMW exist widely in the northwestern and central areas of the subtropical gyre typically in the density range of 1025.0~1025.6 kg/$m^3$ and 1026.0~1026.5 kg/$m^3$, respectively (Suga et al. 2004).

At 160°W, the PV on isopycnal surfaces tends to be meridionally uniform in the vicinity of the climatological gyre axis in the lower main pycnocline below the isopycnal surface of about 1026.5 kg/$m^3$ (Fig. 2-11d). In the density range between 1025.5 and 1026.5 kg/$m^3$, above the lower pycnocline, the meridional gradient of PV is generally negative near the climatological gyre axis, indicating that the PV increases to the south. The increase in PV is relatively small in the low PV core of the CMW around 1026.2~1026.5 kg/$m^3$, but obvious in the upper pycnocline at the isopycnals of 1025.7~1026.0 kg/$m^3$ (Figs. 2-11b, d). Above the isopycnal of 1025.5 kg/$m^3$, the PV gradient is mostly nearly zero except weak positive just beneath the winter mean sea surface density.

The southward increase of PV near the climatological gyre axis in the east is also recognizable from the climatological mean maps of PV. Figure 2-12 shows the mean PV and acceleration potential relative to 2000 dbar on the isopycnal surfaces of 1026.0 and 1026.4 kg/$m^3$. On these surfaces the CMW appears as a lateral PV minimum to the north of the climatological gyre axis (grey lines in Fig. 2-12) between 170°W and 160°W, and extends to the south across the climatological gyre axis roughly along the streamlines of the anticyclonic subtropical gyre circulation, forming a tongue-like structure of PV to the southwest. The PV generally increases to the downstream, which is probably due to the dissipation by mixing effects of eddies (Xie et al. 2011). Indeed, the changes in PV along

the streamlines confirm the general increase to the downstream (Fig. 2-12c), though it is relatively weak in the lower PV layer of the CMW (blue line in Fig. 2-12c). These features are also seen from the PV maps shown by Suga et al. (2004) and Kobashi et al. (2006).

At 160°E in the west, the isopycnal PV is relatively uniform near the climatological gyre axis in the STMW layer around 1025.4 kg/m$^3$ and deep layer below 1026.9 kg/m$^3$ (Fig. 2-11c). On the other hand, the PV gradient is positive in the lower main pycnocline between 1025.8 and 1026.8 kg/m$^3$, indicating the southward decrease of PV, which is in contrast to relatively uniform PV of the lower pycnocline in the east. This decrease in PV to the south is primarily due to relatively high PV water of the pycnocline at depths of 350~700 m (Fig. 2-11a), which lies in the midst of a strong eastward flow of the Kuroshio Extension (Fig. 2-10a), suggesting that the pycnocline of the Kuroshio Extension disrupts the meridional continuity of PV. The decrease in PV to the south is also seen from the changes in PV along the acceleration potentials (Fig. 2-12c). The water in the pycnocline of the Kuroshio Extension first moves to the east and then veers to the southwest, during which the PV gradually decreases. The high PV water in the pycnocline is also clearly identified from the zonal sections of potential density and PV (Fig. 2-13), displaying that the high PV pycnocline extends to about 180°, approximately in the area where the weak gyre shift with depth is observed.

The thickness of density layers may be straightforward to see the relationship with the gyre shift. In the present study, the thickness ($h$) is defined as follows

$$h = \frac{f}{PV} = -\rho \frac{\Delta z}{\Delta \sigma_\theta}. \qquad (2\text{-}4)$$

Figure 2-14 shows the meridional distributions of the thickness on several isopycnal surfaces, which are zonally averaged between 150°E and 170°E and 170°W and 150°W. The

gray curves in each panel represent the thickness that would exist when the isopycnal PV is uniform meridionally, and they were calculated by averaging PV within a 2° latitude bin in the vicinity of the climatological gyre axis on each isopycnal surface and then dividing $f$ by it at each latitude. Therefore, the meridional gradient of the gray curves is $\beta$.

As expected from the PV sections in Fig. 2-11, the thickness of density surfaces in the lower main pycnocline below the isopycnal of 1026.5 kg/m$^3$ in the east decreases to the south near the climatological gyre axis almost along with $\beta$ (Figs. 2-14m, n) because of the uniform PV there. In the CMW layer (Figs. 2-14j~l), the thickness also decreases to the south but with larger gradients than $\beta$, which is especially manifest at 1026.0 and 1026.2 kg/m$^3$ (Figs. 2-14j, k), consistent with the southward increase in PV. The southward decreases of the thickness are also evident in the upper pycnocline above the CMW (Figs. 2-14h, i). These results indicate that the thickness of all density layers decreases to the south in the east, favoring the spiral of velocity vectors and thus the northward shift of the gyre axis.

On the other hand, in the west, the layer thickness shows a southward increase or a nearly constant value near the climatological gyre axis in the main pycnocline between 1025.8 and 1026.8 kg/m$^3$ (Figs. 2-14b~f). These features are confined to the vicinity of the climatological gyre axis, suggesting that the strong Kuroshio Extension is a primary cause of the small gyre shift in the west. In fact, the mean map of geostrophic velocity vertically averaged in the upper 2000 m (Fig. 2-15) demonstrates that the small gyre shift occurs only along the strong Kuroshio Extension.

It is interesting to note that the gyre shift occurs non-uniformly in the vertical in the east (Fig. 2-11). The northward shift is relatively small near the surface, in the CMW layer between 300 m and 500 m depths, and at depths deeper than 900 m, and in contrast, it is large between these layers, equivalently in the upper and lower main pycnoclines.

These features are also confirmed from the zonal section of the vertical gradient of the climatological gyre axis (Fig. 2-13a). The vertical gradient of the climatological gyre axis is calculated from the differences in positions of the climatological gyre axis between the adjacent depths, and the large gradient means the large northward shift of the gyre. Figure 2-13 clearly displays the small shift in the low-PV CMW layer embedded between the upper and lower pycnoclines.

I investigate the vertical non-uniform shift of the gyre axis, by looking into velocity structure in the vicinity of the gyre axis. Here, I diagnose the observed gyre shift by decomposing it into two components related to vertical and horizontal shears of zonal flow. Since the climatological gyre axis with the high appearance rate is generally in good agreement with the gyre axis of the time mean section (Fig. 2-10), here I focus on the positions of zero mean zonal velocity as the gyre axis. This enables us to decompose the change in position of the gyre axis with depth (d$y$/d$z$) as below

$$\left.\frac{dy}{dz}\right|_{u=0} = -\left.\frac{\partial u}{\partial z}\right|_{u=0} \Big/ \left.\frac{\partial u}{\partial y}\right|_{u=0}, \qquad (2\text{-}5)$$

where $\partial u/\partial z$ and $\partial u/\partial y$ are the vertical and horizontal shears of zonal flow, respectively. For convenience, multiplying both sides of the equation by minus, I will refer to the left hand side (- d$y$/d$z$) as the change in the gyre axis (positive means a northward shift with depth). This equation means that smaller vertical shear and larger horizontal shear would be related to smaller meridional shift. Figure 2-16 shows all vertical profiles of these variables between 150°W and 170°W and their averages. The change in the gyre axis (Fig. 2-16a) captures well two peaks around 250 m and 600 m depths in the pycnocline with the dip between the two peaks.

On which shears is the vertical non-uniformity of the gyre shift dependent? To address this point, I first prepare smoothed profiles of the shears by fitting the mean vertical

profile to a following Gaussian function with the least squares method between 100m and 1000m,

$$\left.\begin{aligned}\frac{\partial u}{\partial z}_{smth} &= A_1 + B_1 \exp\left(-\frac{z^2}{a_1^{\,2}}\right)\\ \frac{\partial u}{\partial y}_{smth} &= A_2 + B_2 \exp\left(-\frac{z^2}{a_2^{\,2}}\right)\end{aligned}\right\}, \qquad (2\text{-}6)$$

where $A_{1,2}$, $B_{1,2}$, and $a_{1,2}$ are coefficients of the Gaussian function. The results are shown by red lines in Figs. 2-16b and c. These smoothed profiles produce the gentle shift of the gyre axis with no notable peaks (a red line in Fig. 2-16a). Then, using these smoothed and original profiles, I calculate two combinations,

$$-\left(\frac{dy}{dz}\right)_{\partial u/\partial z} = \frac{\partial u}{\partial z}_{orig} \Big/ \frac{\partial u}{\partial y}_{smth}, \qquad (2\text{-}7)$$

and

$$-\left(\frac{dy}{dz}\right)_{\partial u/\partial y} = \frac{\partial u}{\partial z}_{smth} \Big/ \frac{\partial u}{\partial y}_{orig}, \qquad (2\text{-}8)$$

where the subscript of the left hand side denotes the variable of the original profile. The results are shown by blue and green lines in Fig. 2-16a, respectively.

The $(dy/dz)_{\partial u/\partial z}$ shows the two peaks in the pycnocline and the dip between the peaks, reproducing well the observed change of the gyre axis. In contrast, though having weak peaks at depths of 200 m and 500 m, the $(dy/dz)_{\partial u/\partial y}$ exhibits more gentle change of the gyre axis, which is rather similar to the profile computed from both smoothed shears (see a red line in Fig. 2-16a). This result indicates that the vertical shear of zonal flow is a major factor for the observed non-uniformity of the gyre shift. Because the vertical shear of zonal flow is related to the meridional gradient of density ($\partial\rho/\partial y$) based on the thermal wind relationship, the large gyre shift in the pycnocline is considered due to the large meridional density gradient of the pycnocline and the small shift in the CMW layer

due to the horizontal uniformity of the CMW. Although the properties of the CMW actually changes to the downstream as seen from the PV maps in Fig. 2-12, the CMW can be still recognized as a relatively uniform water mass from the meridional section in Fig. 2-11b and the horizontal changes in density are smaller within the CMW compared to in the main pycnoclines.

## 2.5 Summary and discussion

In this chapter, the mean structures of the North Pacific subtropical gyre were investigated to focus on the gyre axis, using Argo float observations and several wind stress products. The gyre axes of depth-integrated geostrophic circulation and the vertical structure of the gyre axes both show differences between the regions east and west of about 180°.

Depth-integrated geostrophic circulation shows two gyre axes about 25°N and 30°N in the eastern basin, which correspond well to those of the wind-driven circulation. The two gyre axes are created by a local cyclonic wind stress curl anomaly between 145°W and 125°W, probably due to southeasterly wind anomalies there. It is expected from the Sverdrup balance that the two gyre axes would extend further to the west across the subtropical gyre, but the actual geostrophic circulation shows only one gyre axis around 30°N to the west, suggesting some discrepancy with the Sverdrup balance in the west.

Why are not the two ocean gyre axes stretched to the western basin, as expected from the Sverdrup balance? This may boil down to why barotropic Rossby waves forced by the cyclonic wind stress curl anomaly do not propagate to the west. One possible explanation is that Rossby waves actually propagate to the west, but the wind-driven circulation is masked by the Kuroshio recirculation gyre, where the transport is dominated by

nonlinear dynamics. The recirculation is seen from depth-integrated dynamic height contours veering sharply from the eastward-flowing Kuroshio Extension to the southwest in the region west of about 180° (Fig. 2-1). The recirculation is characterized by strong barotropic motions with a depth-averaged velocity of about 5~10 cm/s near the south of the Kuroshio Extension (Yoshikawa et al. 2004; Chen et al. 2007), which is much larger than a typical Sverdrup velocity with the order of 0.1 cm/s. Figure 2-15 shows a large depth-averaged geostrophic velocity in the region south of the Kuroshio Extension west of 180° in comparison to that in the east, though the magnitude of the velocity about 1~2 cm/s is much smaller than the observations of Yoshikawa et al. (2004) and Chen et al. (2007) probably due to the spatial smoothing of the MOAA GPV.

In the eastern basin, the two ocean gyre axes are located slightly to the south by a few degrees latitude, compared to the gyre axes of the wind-driven circulation (Fig. 2-6). This might be due to the advection by the Sverdrup flow itself. The Sverdrup theory expects the ocean circulation set up only by Rossby wave propagations, and thus does not include the effect of the mean Sverdrup flow on Rossby waves. The actual ocean gyre axis may be displaced to the south due to the southwestward mean flow in the eastern region.

The vertical structures of the gyre axis are also quite different between the east and the west of about 180°. The gyre axis shows a prominent northward shift with depth in the east, where a broad weak zonal flow is dominant and the thickness of density layers decreases to the south. On the other hand, in the west, the gyre axis lies just along the southern flank of the strong barotropic-like Kuroshio Extension jet with no remarkable northward shift. It is suggested that the Kuroshio Extension may disrupt the meridional continuity of PV around the jet and thus prevents the gyre axis from shifting to the north. The Kuroshio Extension is a strong jet and its typical speed is larger than baroclinic

Rossby waves propagating at these latitudes. For example, first baroclinic Rossby waves have a speed of about 3~5cm/s there (Chelton et al. 2011). As a consequence, wind-generated Rossby waves cannot travel into the Kuroshio Extension to the west of 170°E, hampering the adjustment of the ocean structure to the wind-driven circulation.

The PV used in the present study does not consider the contribution from relative vorticity. For a large-scale circulation, relative vorticity is reasonably negligible, but in the region of a strong flow such as the Kuroshio Extension, some attention might be needed. Qiu et al. (2006) analyzed CTD and shipboard acoustic Doppler current profiler (ADCP) measurements and pointed out that the inclusion of relative vorticity decreases and increases PV along the southern and northern sides of the Kuroshio Extension jet, respectively, and as a result the PV maximum along the jet is intensified with its position shifted slightly to the north. The effect of relative vorticity disappears immediately away from the jet. Thus, relatively vorticity may not change qualitatively our findings of the southward decrease in PV from the KE region across the gyre axis in the main pycnocline in the west.

Despite the large southward decrease in the thickness of the CMW layers (Figs. 14j~l), the northward shift of the gyre axis is relatively small there. This suggests that, although the southward decrease in the layer thickness is necessary for $\beta$ spiral and the northward shift of the gyre axis, there are other factors that affect the magnitude of the gyre axis shift. In fact, this study found that smaller shift of the gyre axis is due to the horizontal uniformity of the CMW, which shows dynamical effects of the CMW on the subtropical gyre. Most traditional studies on mode waters may have put emphasis on their characteristics as a heat reservoir memorizing wintertime ocean-atmosphere interaction (e.g., Hanawa and Sugimoto 2004). In contrast, some recent studies have revealed important dynamical roles of mode waters in ocean circulation, and they show that mode

waters can generate a narrow surface jet through the transportation of low PV water (e.g., Kobashi and Kubokawa 2012). The present study may present another different way that mode waters can affect large-scale ocean circulations.

Table 2-1. Summary of the information for each wind stress dataset used in the present study.

| Dataset | Types | Analysis period | Spatial resolution |
|---|---|---|---|
| JRA | Reanalysis | Jan. 2001~ Dec. 2011 | T106 Gaussian grid (approximately 1.125°) |
| J-OFURO | Satellite observations | Jan.2001~ Dec. 2008 | 1° |
| NCEP1 | Reanalysis | Jan. 2001~ Dec. 2011 | T62 Gaussian grid (approximately 1.9°) |
| NCEP2 | Reanalysis | Jan. 2001~ Dec. 2011 | T62 Gaussian grid (approximately 1.9°) |
| MERRA | Reanalysis | Jan. 2001~ Dec. 2011 | ½° latitude × ⅔° longitude |
| HR | Ship observations | Monthly climatology from 1890~1976 | 2° |

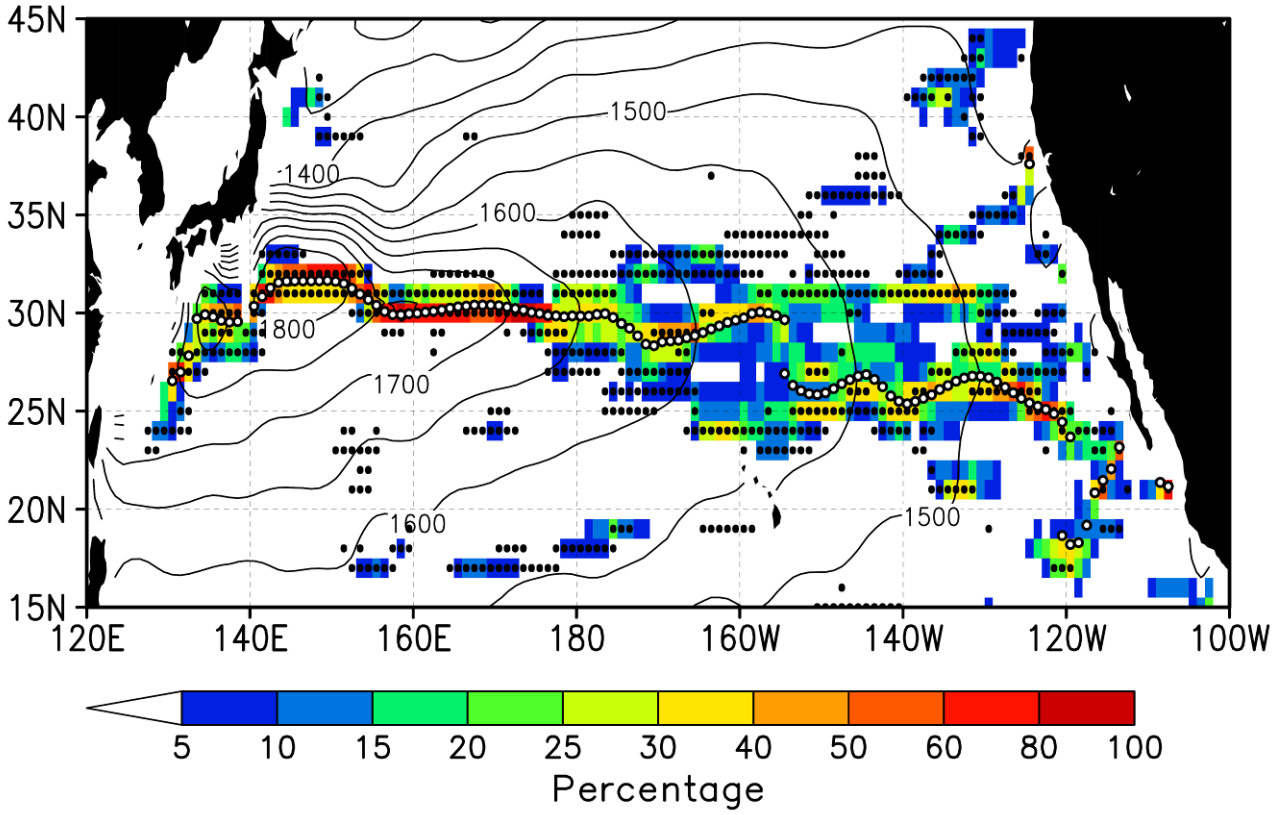


Fig.2-1. Mean depth-integrated dynamic height ($m^2$) and the rate of the appearance of the gyre axis (color). Open circles denote the position of the gyre axis determined from the mean depth-integrated dynamic height. Black dots denote the grid points where the appearance rate of the gyre axis is statistically significant at the 95 percentile confidence interval.

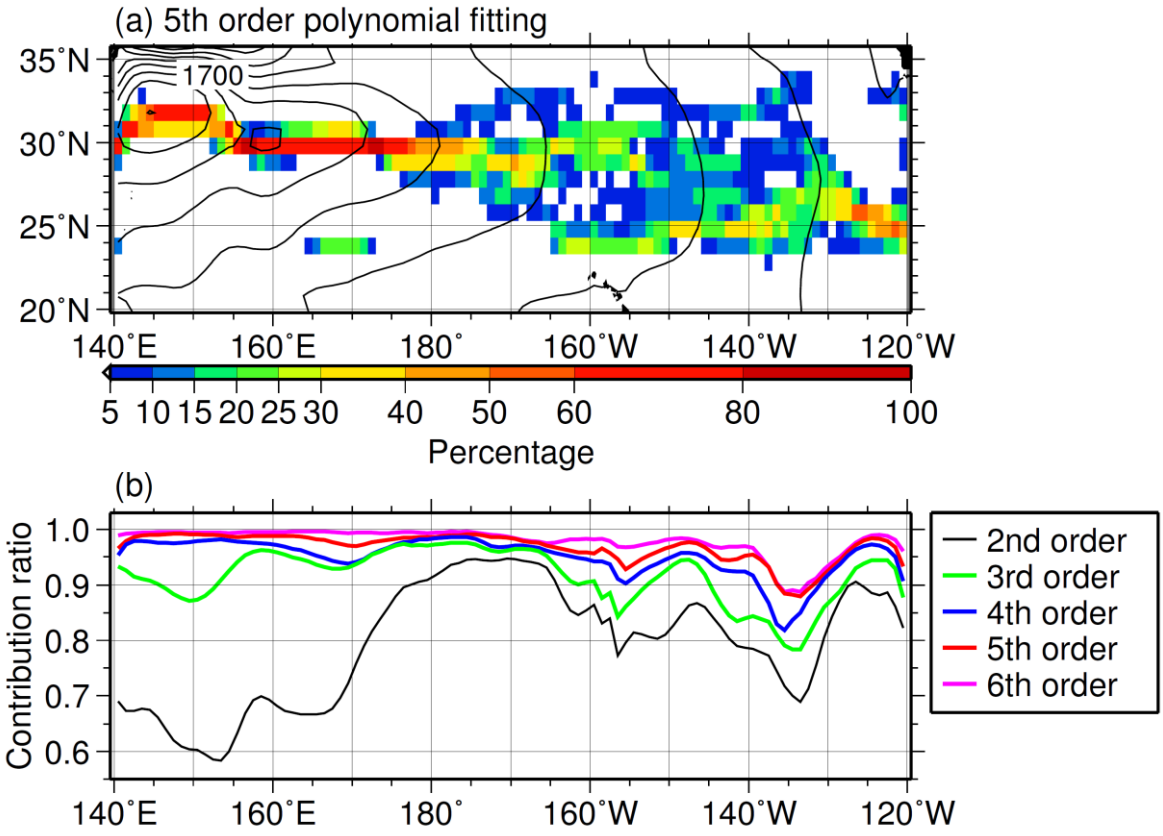


Fig.2-2. (a)Same as in Fig. 2-1, but calculated from a 5th order polynomial curve fitting to a monthly meridional profile of the depth-integrated dynamic height in the latitude range of 20°~35°N at each longitude, and (b) the mean contribution ratio of each fitting of 2nd to 6th order polynomials at each longitude (see the text for details).

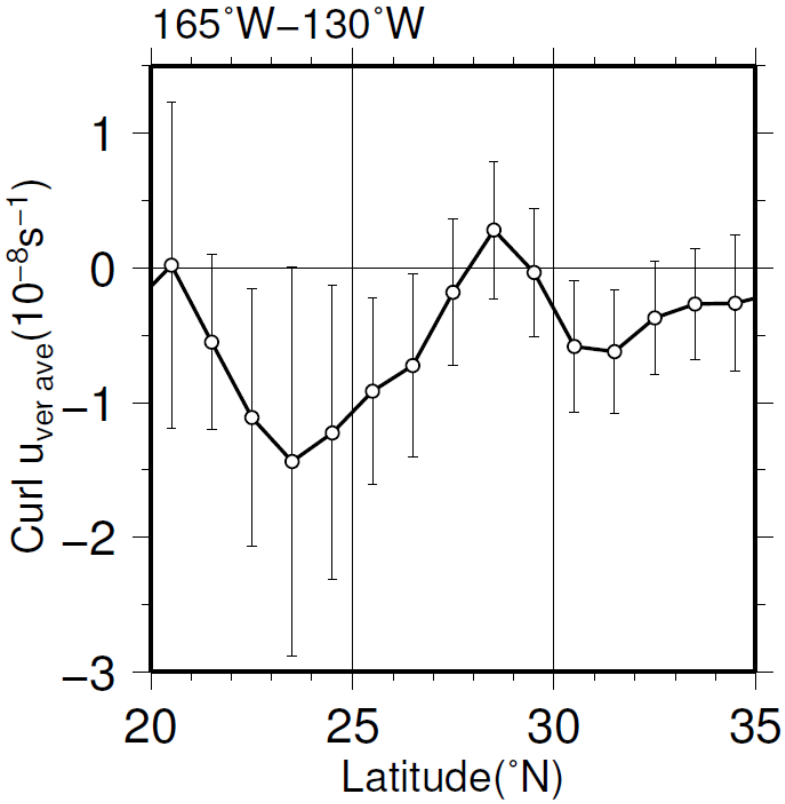


Fig.2-3. Relative vorticity of the depth-averaged geostrophic velocity between the surface and 2000 m, zonally averaged between 165°W and 130°W. The error bars denote the standard deviation.

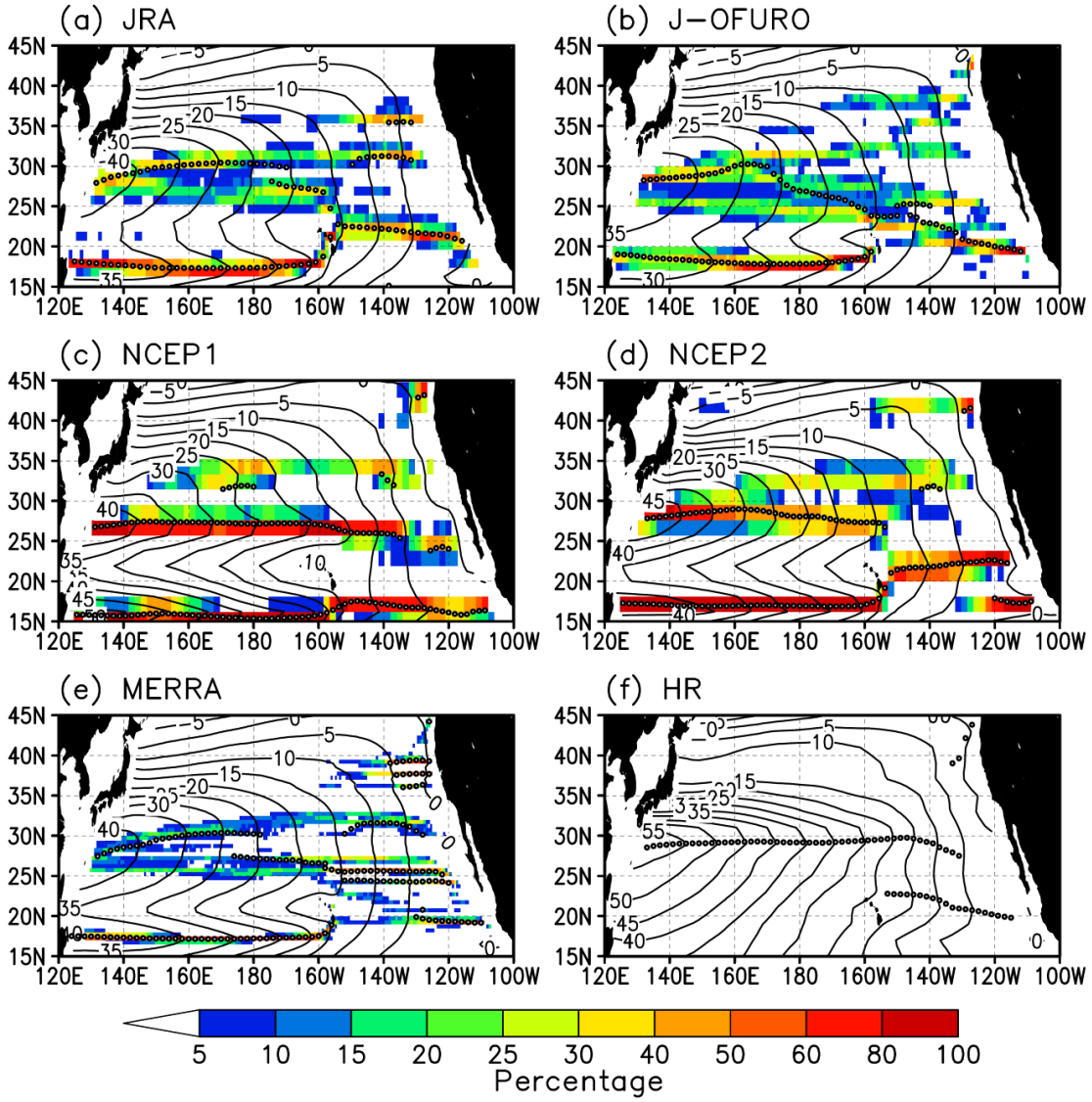


Fig.2-4. Mean wind-driven transport (Sv) and the rate of the appearance of the gyre axis (color), calculated from (a) JRA, (b) J-OFURO, (c) NCEP1, (d) NCEP2, (e) MERRA and (f) HR. Open circles denote the position of the gyre axis determined from the mean wind-driven transport, plotted every about 2° longitude interval.

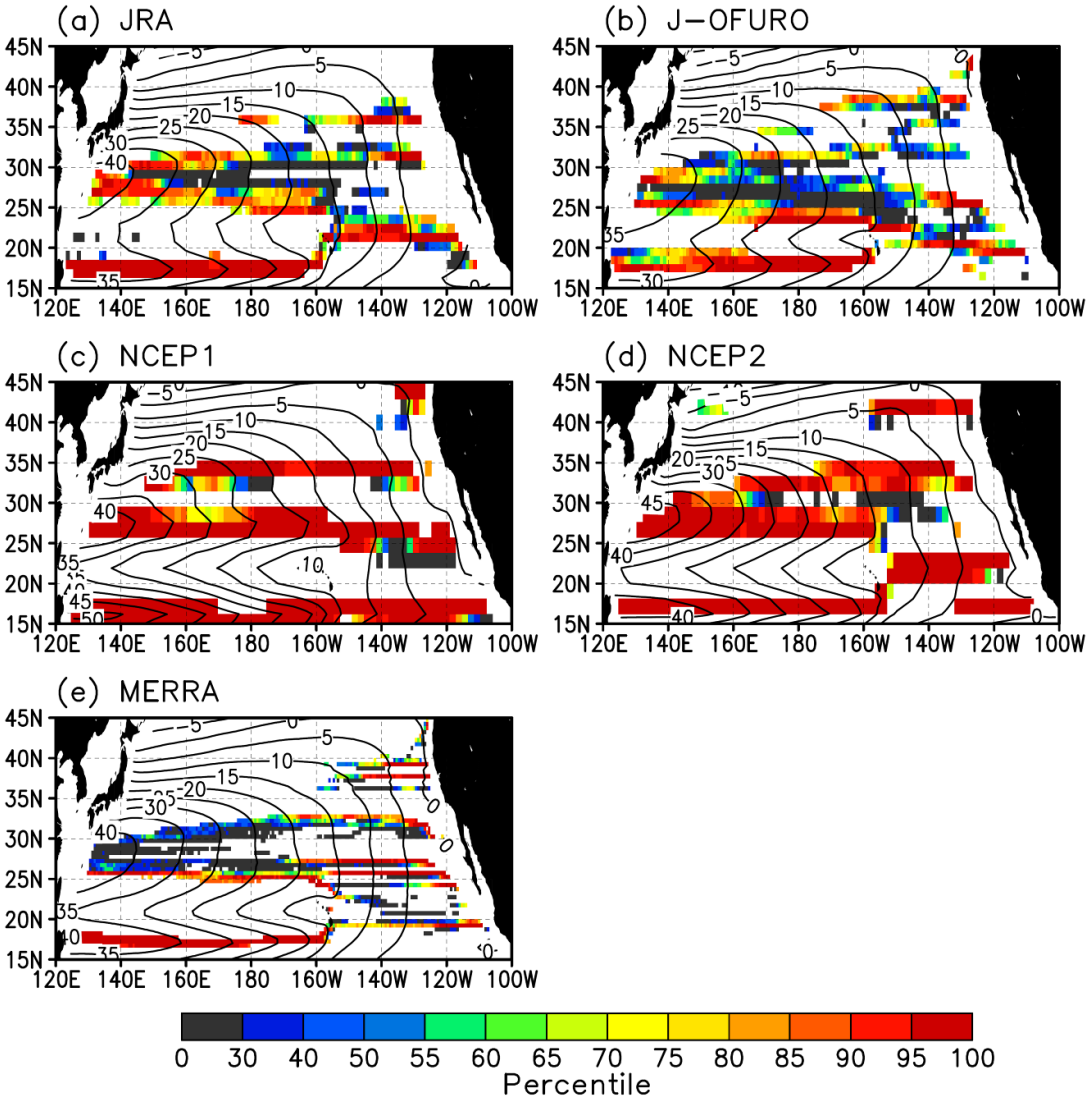


Fig.2-5. Percentile of the rate of the appearance of the gyre axis among 1000 appearance rate maps generated by the bootstrap method (see the text for detail), for (a) JRA, (b) J-OFURO, (c) NCEP1, (d) NCEP2 and (e) MERRA, shown only at the grid points with the appearance rate more than 5% in Fig. 2-4. Contours are the mean wind-driven transport (Sv), the same as in Fig. 2-4.

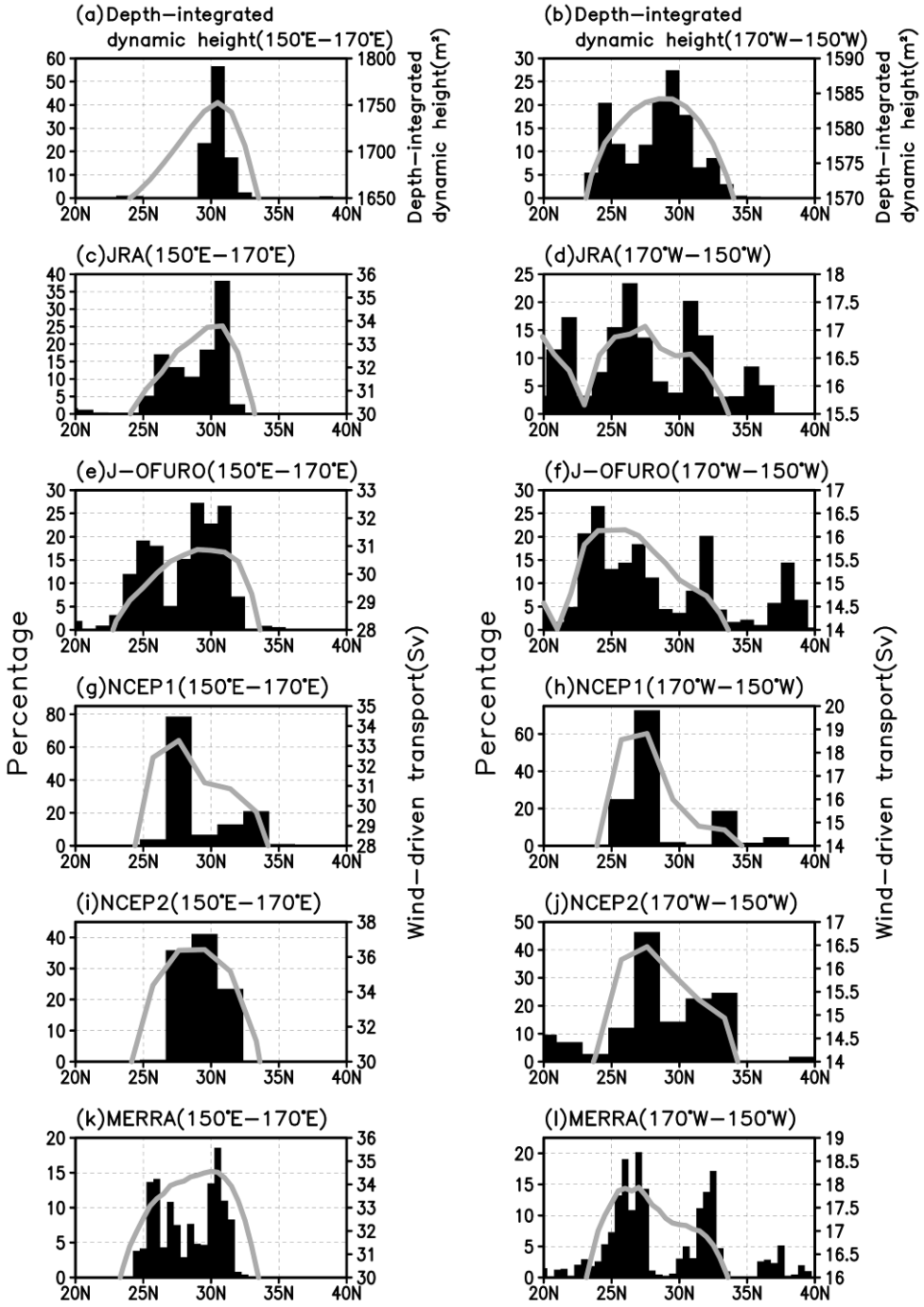


Fig.2-6. Rates of the appearance of the gyre axis of (a, b) the depth-integrated dynamic height and (c~l) the wind-driven transport, averaged between 150°E and 170°E (left) and between 170°W and 150°W (right). Gray curves denote the zonal mean values in each longitudinal range.

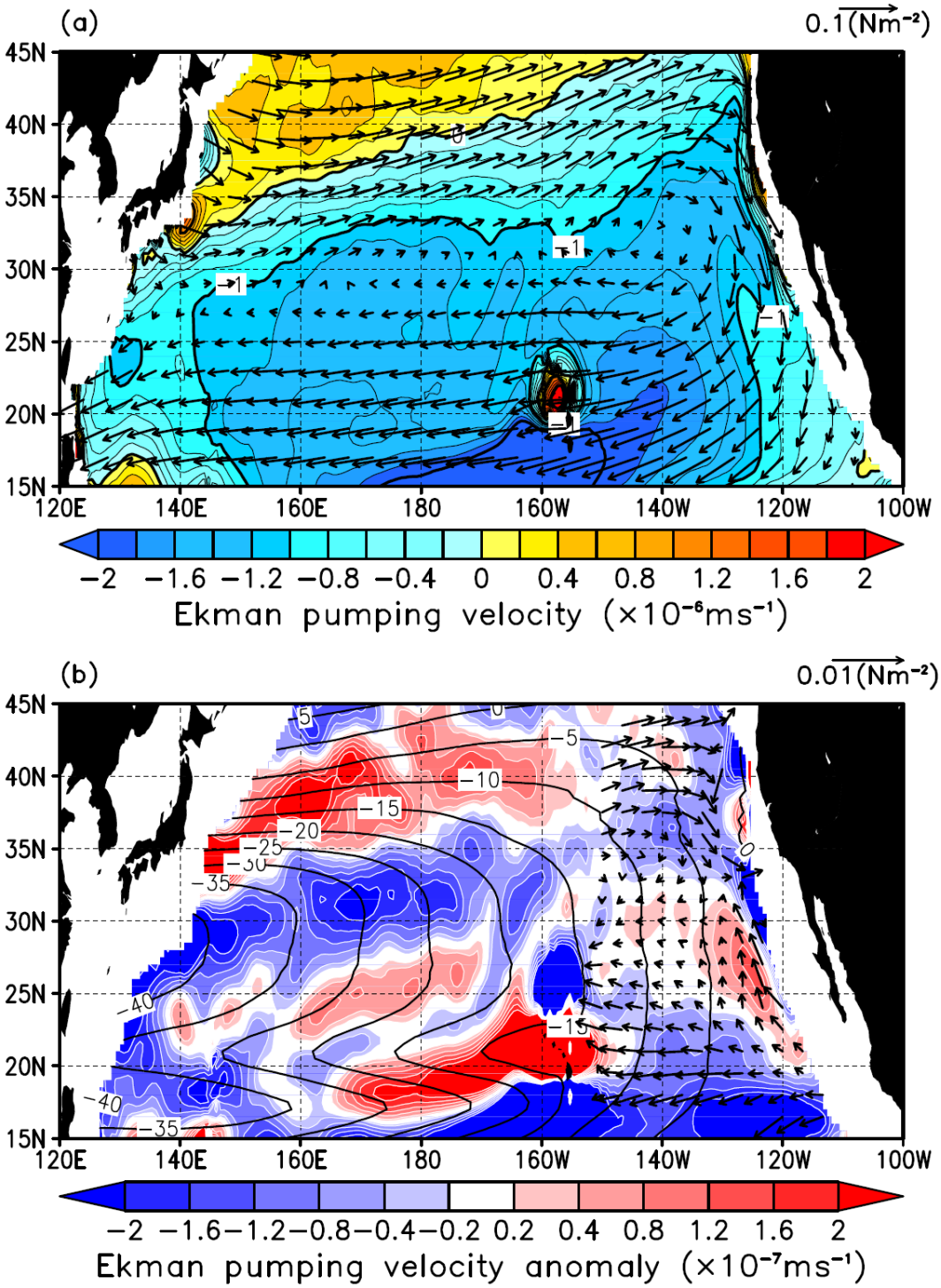


Fig.2-7. (a) Ekman pumping velocity ($w_{EK}$) and wind stress vector from the MERRA, and (b) their anomalies obtained by a meridional high-pass filter. The wind stress vector anomaly is shown only for the east of 150°W. Black contours in the lower panel indicate the mean wind-driven transport.

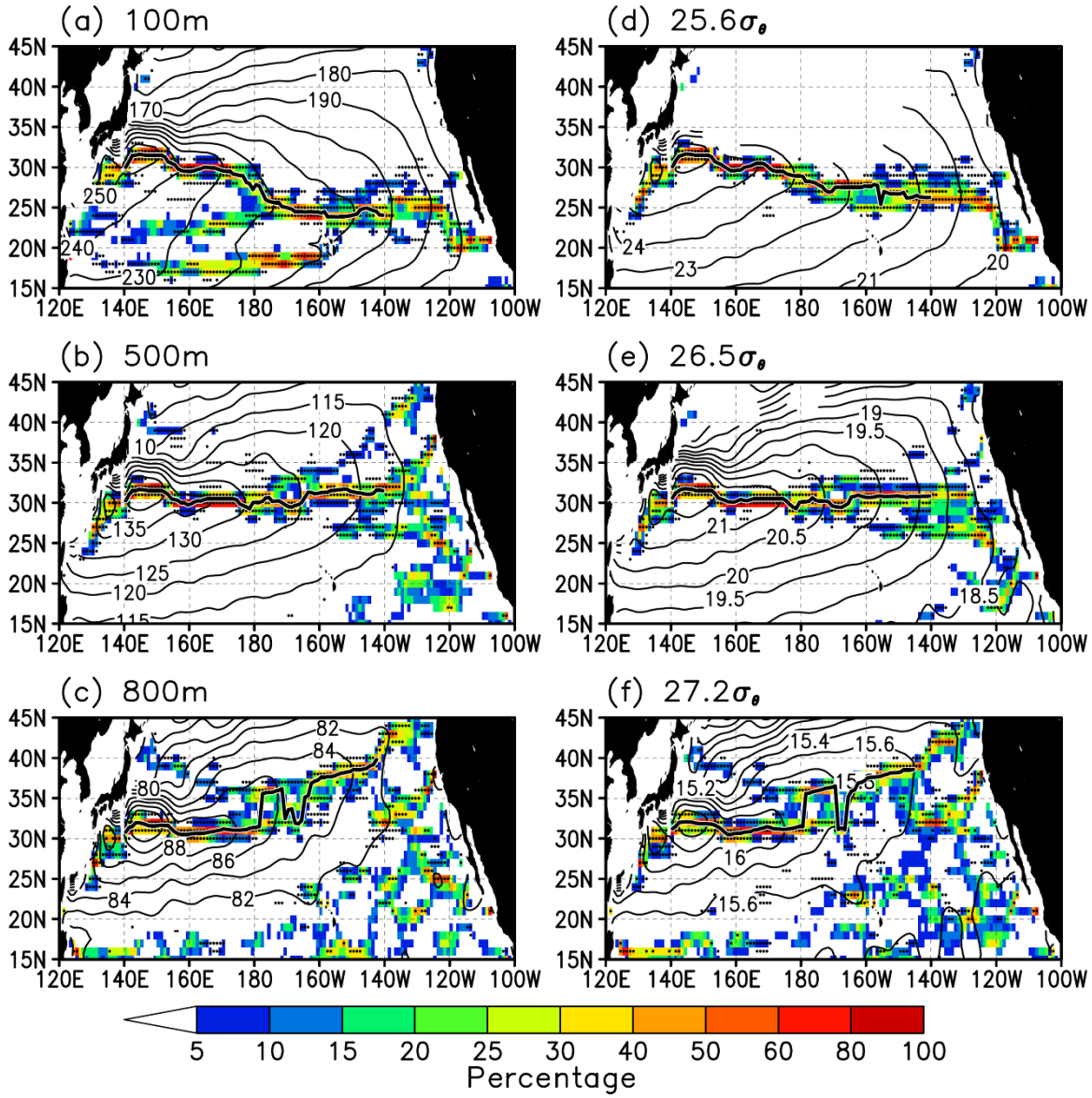


Fig.2-8. Mean dynamic heights at (a) 100 m, (b) 500 m, and (c) 800 m depths and acceleration potential on (d) 1025.6, (e) 1026.5, and (f) 1027.2 kg/m$^3$ density surfaces. Color indicates the appearance rates of the gyre axis. Thick black lines show the position of the climatological gyre axis determined from the appearance rate (see the text for details). Black dots denote the grid points where the appearance rate is statistically significant at the 95 percentile confidence interval.

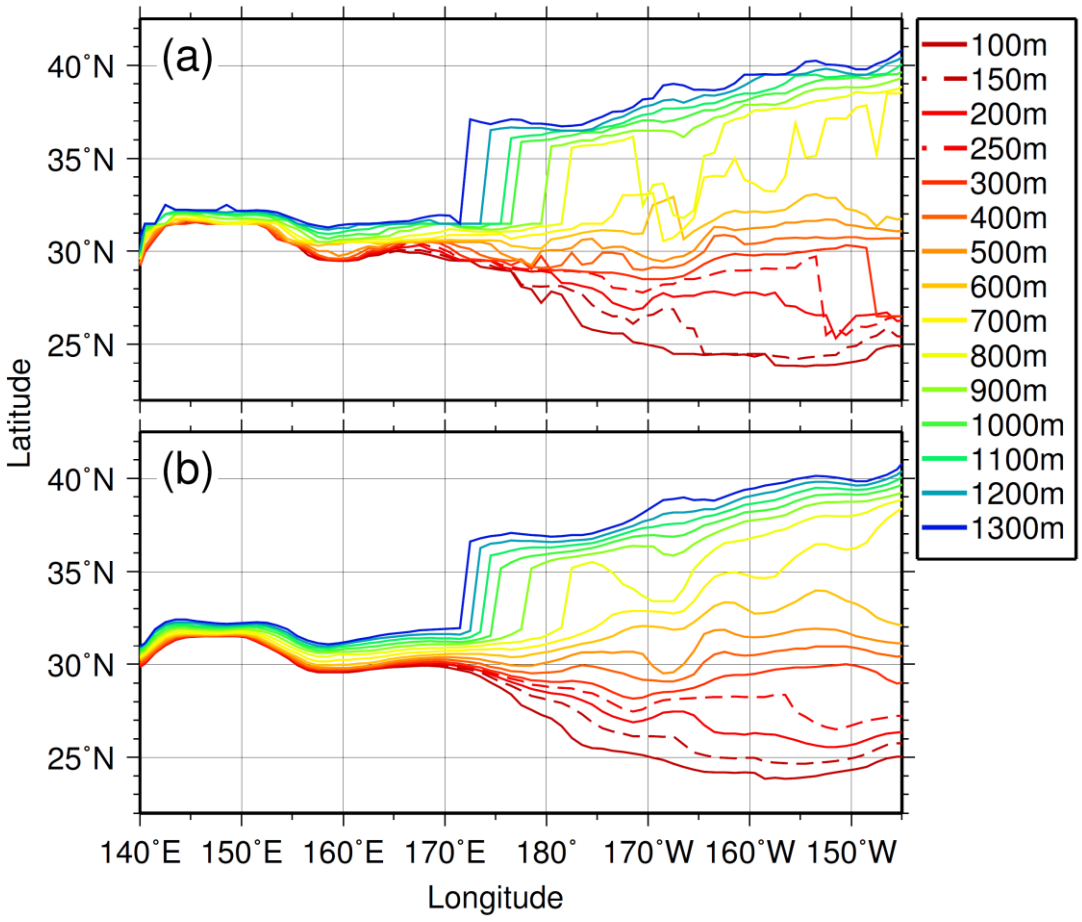


Fig.2-9. Distribution of the gyre axis at different depths, determined from (a) the rate of the appearance of the gyre axis and (b) the mean dynamic height maps.

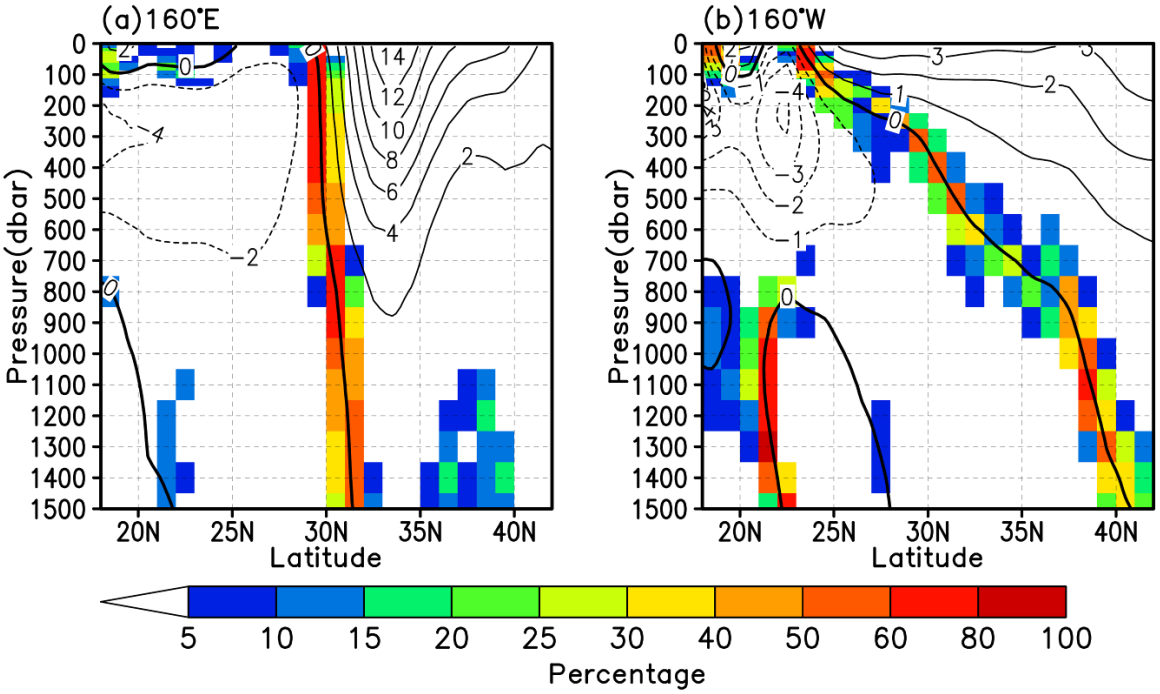


Fig.2-10. Meridional sections of the rate of the appearance of the gyre axis (color) and the zonal geostrophic velocity (cm/s) along (a) 160°E and (b) 160°W.

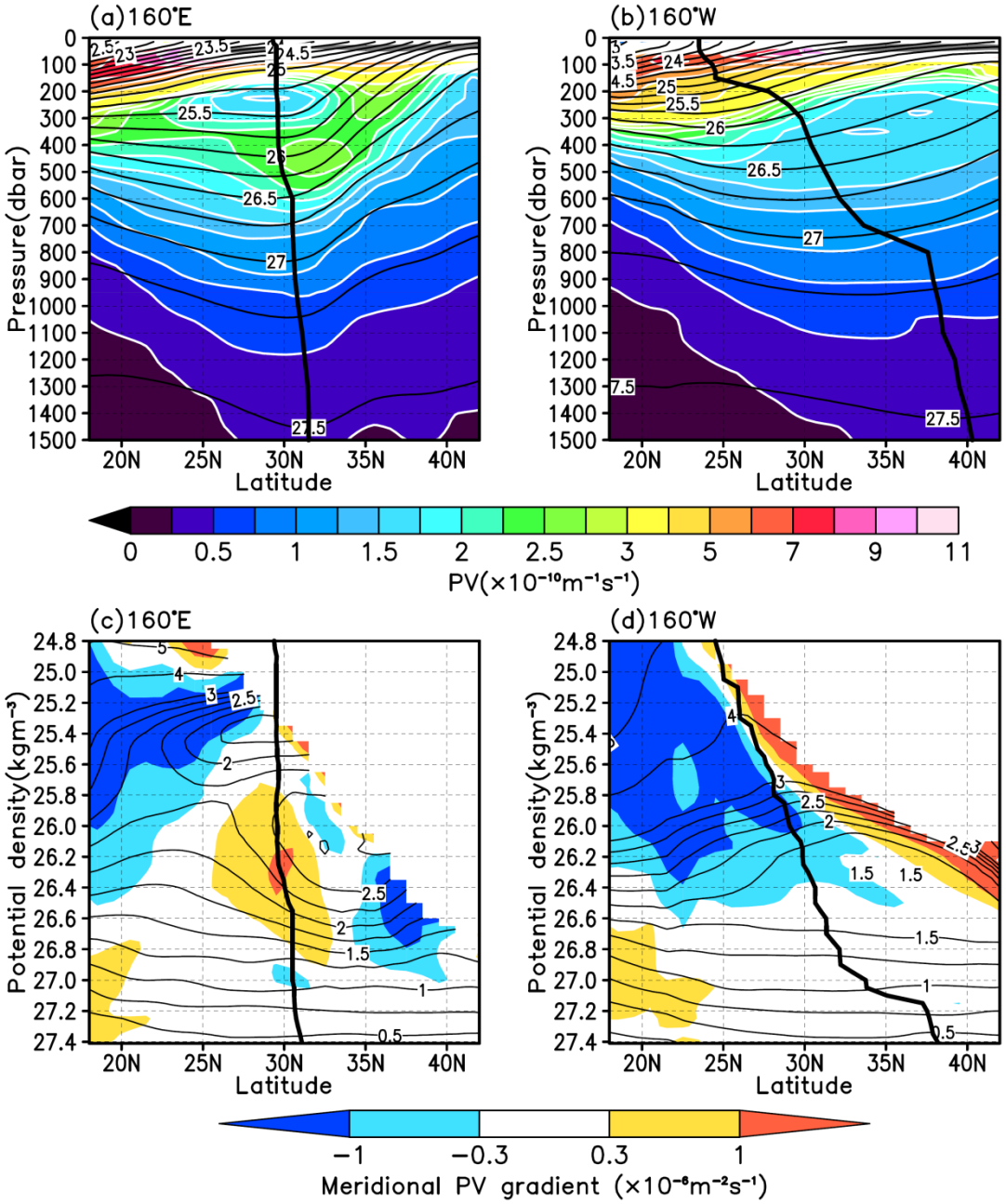


Fig.2-11. (a, b)Meridional sections of PV (color) and potential density (black contours), and (c, d) PV (black contours) and its meridional gradient (color) on the vertical co-ordinate of potential density along (a, c) 160°E and (b, d) 160°W. Thick black lines show the climatological gyre axis. In the lower panels, the area where the density is less than the winter sea surface density is masked out.

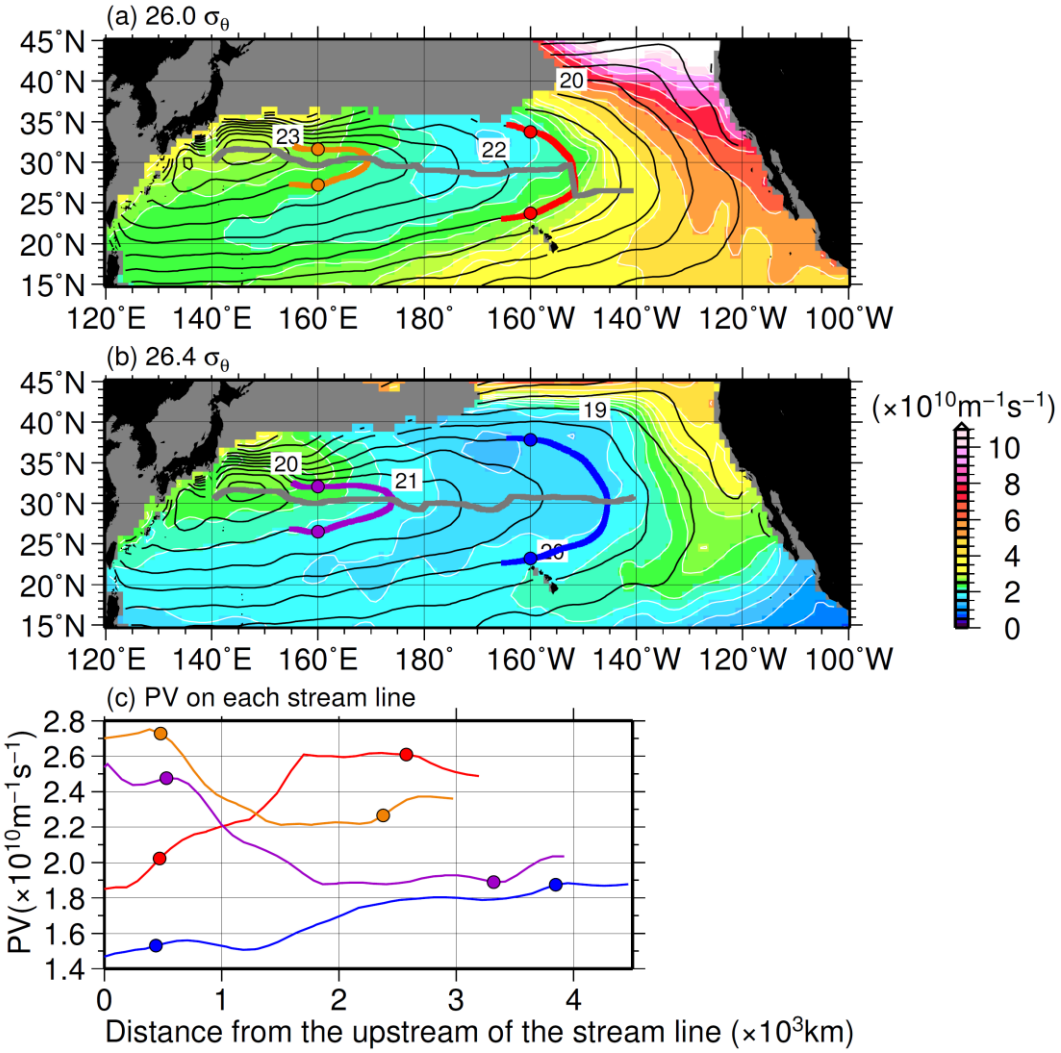


Fig.2-12. Maps of mean PV (color) and acceleration potential relative to 2000 dbar (black contours) at the isopycnal surfaces of (a) 1026.0 and (b) 1026.4 kg/m$^3$. Gray lines denote the climatological gyre axis. Light shade indicates the area with the winter sea surface density heavier than each isopycnal. Red (blue) and orange (purple) lines are the isolines of the acceleration potential of 21.5 (20.0) and 23.5 (21.5) m$^2$s$^{-2}$ at the isopycnal surface of 1026.0 kg/m$^3$ (1026.4 kg/m$^3$) across 160°W and 160°E, respectively. (c) Changes in PV along each streamline in (a) and (b). Closed circles are point at the intersection of each streamline with 160°W and 160°E.

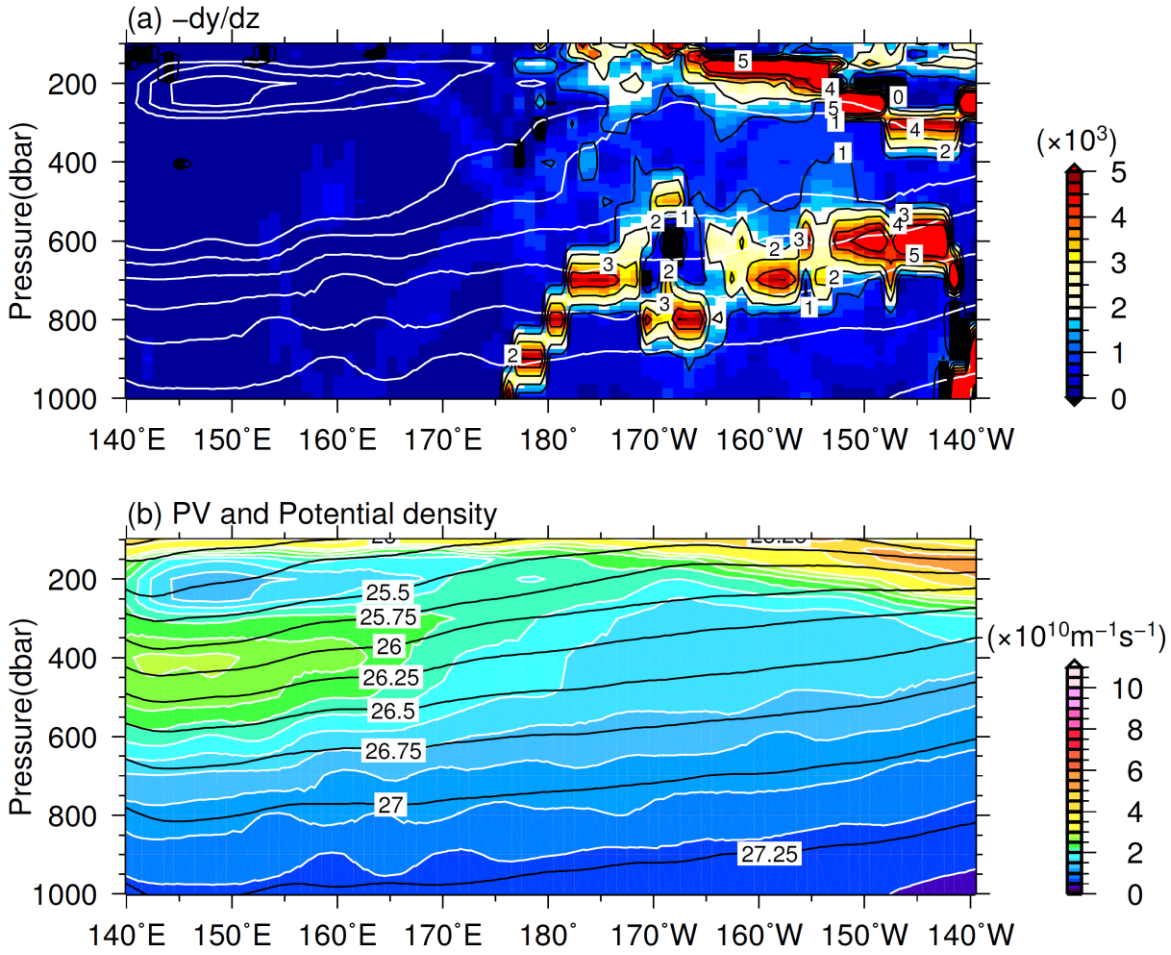


Fig.2-13. Zonal sections of (a) the change in position of the climatological gyre axis with depth (color) and (b) PV (color) and potential density (black contours) averaged between 27.5°N and 32.5°N. White contours in the upper panel show the PV less than $2 \times 10^{-10}$ $m^{-1}s^{-1}$ with contour intervals of $0.25 \times 10^{-10}$ $m^{-1}s^{-1}$.

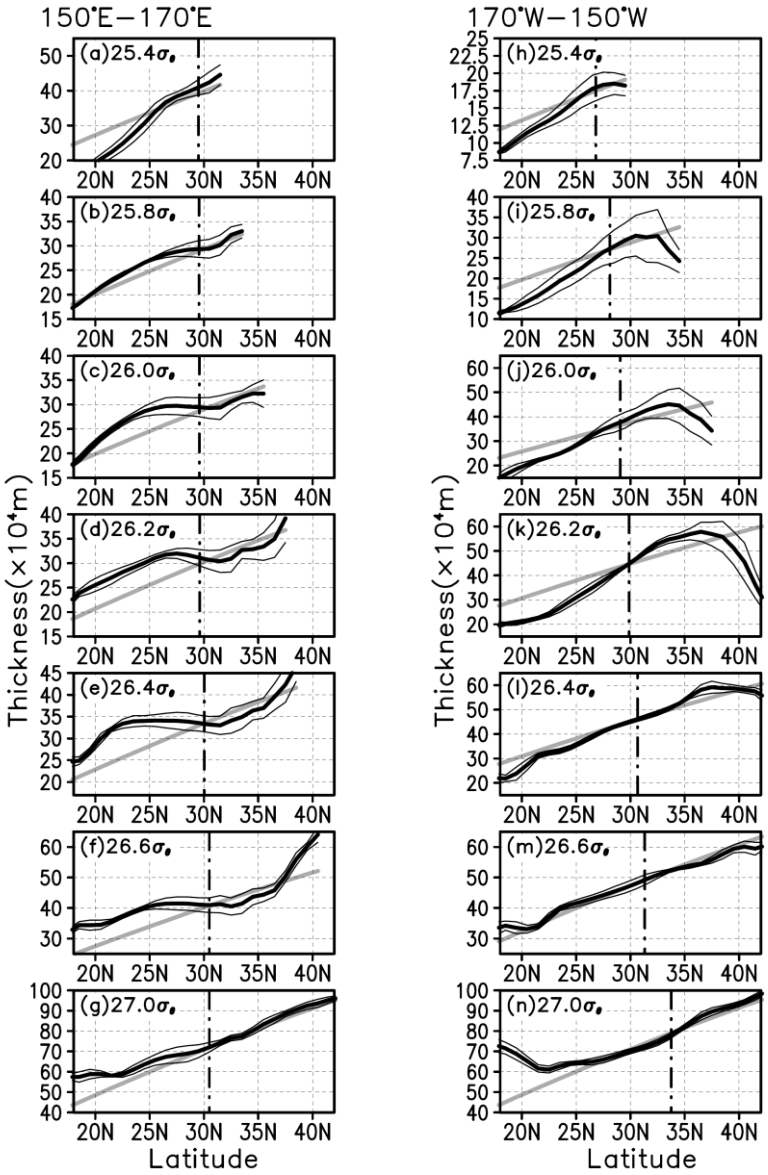


Fig.2-14. Meridional distribution of the layer thickness zonally averaged (a~g) between 150°E and 170°E and (h~n) between 170°W and 150°W at (a, h) 1025.4, (b, i) 1025.8, (c, j) 1026.0, (d, k) 1026.2, (e, l) 1026.4, (f, m) 1026.6 and (g, n) 1027.0 kg/m$^3$ surfaces. The thin black lines indicate the standard deviation. The gray lines show the layer thickness calculated by averaging PV within a 2° latitude bin in the vicinity of the gyre axis and then dividing it into *f*. The broken lines are the position of the climatological gyre axis at the 160°E for (a~g) and 160°W for (h~m).

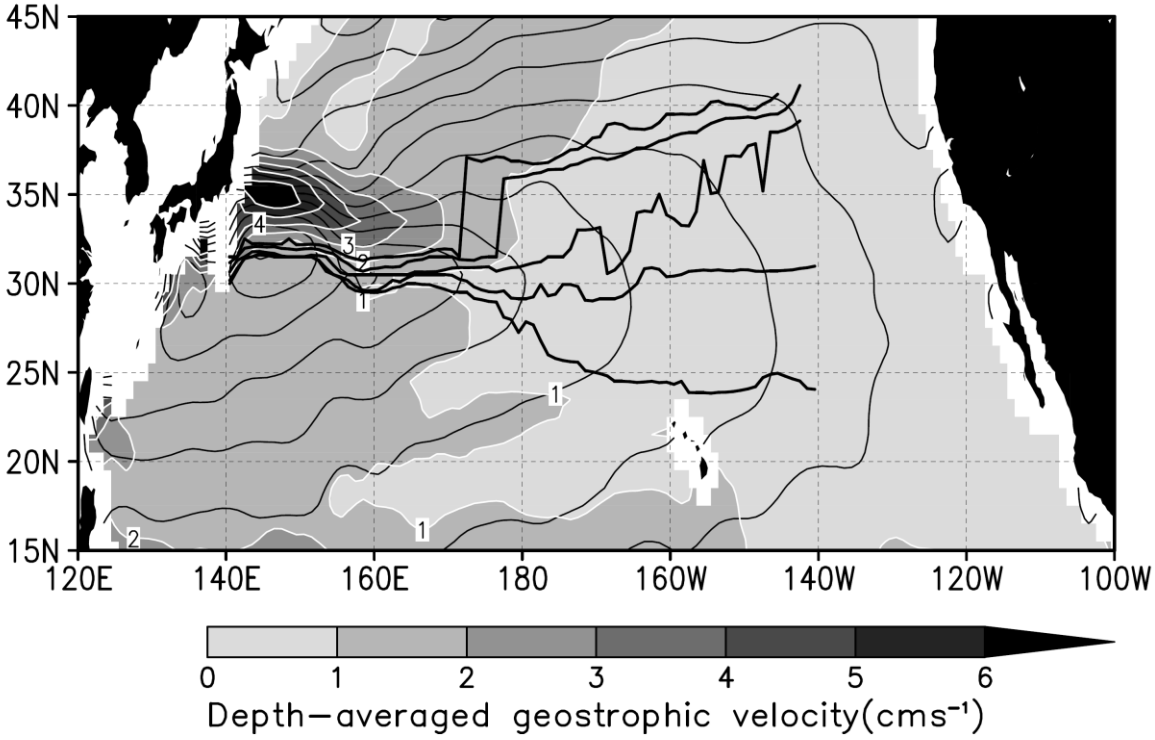


Fig.2-15. Depth-averaged geostrophic velocity between the surface and 2000 m (shade). The thin contours are the mean depth-integrated dynamic height, the same as in Fig. 2-1. The thick black lines denote the climatological gyre axis at 100 m, 400 m, 700 m, 1000 m and 1300 m in Fig. 2~9a.

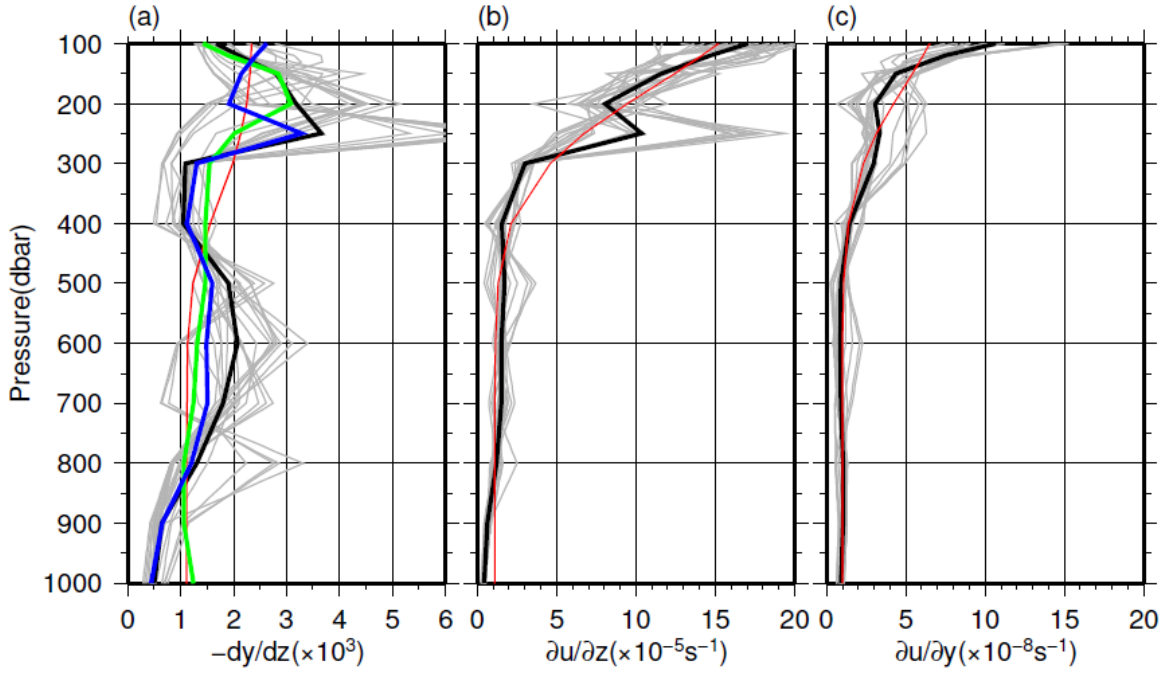


Fig.2-16. Vertical profiles of (a) the change in position of the gyre axis with depth, (b) the vertical and (c) horizontal shears of zonal flow along the gyre axis. Grey lines indicate profiles at each longitude between 150°W and 170°W, and thick black lines indicate the mean profiles. Red curves in (b) and (c) show the smoothed profiles obtained by fitting the mean profile to a Gaussian function, and a red curve in (a) is calculated from theses smoothed profiles. Blue and green curves in (a) indicate the $-(dy/dz)_{\partial u/\partial z}$ and $-(dy/dz)_{\partial u/\partial y}$, respectively (see the text for details).

# Chapter 3
# Temporal variations of the North Pacific subtropical gyre

## 3.1 Introduction

The temporal variations of surface circulation have been investigated with a particular focus on the western subtropical gyre of the North Pacific on the time scales from seasonal to decadal, using mainly satellite altimetry sea surface height data (e.g. Qiu 2002b). Recently, the accumulation of the Argo profiling float data enabled us to investigate the variability of basin-scale ocean circulation at subsurface depths. Giglio et al. (2012) reported that the variations of meridional geostrophic transport are consistent with the meridional Sverdrup transport that are zonally integrated between 150°E and 180°, and the strength and position of the North Pacific subtropical gyre have interannual variations with time scales of 6~8 years from an empirical orthogonal function analysis of sea surface height and depth-integrated dynamic height referenced to 2000db, using Argo data and atmospheric reanalysis data in the period from 2004 to 2011 and satellite sea surface data from 1993 to 2010. But the variations of ocean circulation in the eastern North Pacific have not been investigated in detail so far.

In the eastern part of the North Pacific subtropical gyre, the existence of the anticyclonic circulation centered at the northeast of the Hawaiian Islands, which is known as the Eastern gyral (Sverdrup et al. 1942), has been suggested. Toyoda et al. (2004) showed that using eddy-permitting ocean general circulation model, the formation region of the ESTMW (Hautala and Rommich 1998) is in a good agreement with the position of the anticyclonic circulation similar to the Eastern gyral, and the low PV input associated with

the ESTMW has the tendency to produce an anticyclonic circulation. Aoki and Kutsuwada (2008) showed that the anticyclonic rotation exists in the upper layer above the ESTMW, using the World Ocean Database 2005 (Boyer et al. 2006). But the formation and variations of this anticyclonic circulation have not been fully investigated.

In Chapter 2, the gyre axis, which is defined as a large-scale boundary between eastward motions on the northern part of the subtropical gyre and westward motions on the southern part from the mean vertical-integrated geostrophic circulation, displays the two gyre axes about 25°N and 30°N in the east of 170°E, indicating local cyclonic circulation embedded in the background of basin-scale anticyclonic circulation of the subtropical gyre.

Figure 3-1 shows the mean map of relative vorticity of depth-integrated geostrophic velocity referenced to 2000 dbar averaged from 2004 to 2013. Although the North Pacific subtropical gyre is characterized overall by anticyclonic circulation, namely negative relative vorticity, there are three local cyclonic regions; the STCC region (120°E~170°E, 20°N~25°N), the Hawaiian Lee countercurrent region (120°E~160°W, 20°N) and the eastern region between the meridional two gyre axes in the eastern North Pacific (170°W~130°W, 25°N~30°N). As for the STCC and Hawaiian Lee countercurrent regions, Kobashi and Xie (2012) and Sasaki et al. (2013) reported the formation of the local cyclonic wind field due to the ocean front using the observations and a high resolution model, respectively. These cyclonic wind fields are considered to be partly responsible for the cyclonic circulations.

On the other hand, in the eastern cyclonic region, where there is the eastern STCC (Kobashi et al. 2006) in the southern side of the local cyclonic region, the relationship between the local cyclonic ocean circulation and wind field has not been examined in detail. In addition, the southern region of this cyclonic circulation seems to correspond to

the local anticyclonic circulation of the Eastern gyral. The study in Chapter 3 examines the temporal variations of the depth-integrated circulation with the particularly focus on the local ocean cyclonic and anticyclonic circulations in the eastern part of the subtropical gyre and the vertical structure of the gyre axis.

The rest of this chapter is organized as follows. Section 3.2 describes the ocean and atmospheric data used and the analysis method used in this chapter. In Section 3.3, the periodicity and spatial characteristic of the ocean circulation and the relationship with a wind-driven circulation are shown. In Section 3.4, I will show year-to-year variations of the vertical structure of the gyre axis, and then describe the relationship with the variations of the velocity and potential vorticity structures. Section 3.5 gives summary and discussion.

## 3.2 Data and methods

### 3.2.1 Ocean data

This chapter uses monthly temperature and salinity data of the MOAA GPV from January 2004 to May 2014. In Chapter 2, I used the same MOAA GPV dataset, but analyzed the long-term mean from 2001 to 2011, without examining in detail on the distribution and numbers of the Argo floats. Figure 3-2 shows the number of Argo float profiles at each year in the North Pacific subtropical gyre. It increased remarkably from 2004 and has been more than 10000 profiles per year since 2005. Measurement locations at each year are shown in Fig. 3-3. The Argo profiles in the western North Pacific are densely distributed than in the central and eastern regions all the time. But since 2004,

the Argo float observations in the eastern and central regions seem to have sufficient observation densities to capture the temporal variations of the large-scale ocean circulation.

The Argo float gridded data is available from various research institutes. Giglio et al. (2012) used Rommich and Gilson's (2009) Argo gridded dataset. There are also other datasets such as the product of International Pacific Research Center (IPRC) and Institut français de recherche pour l'exploitation de la mer (IFREMER) and so on. The differences between these datasets are mapping methods and source data. To make comparison of Argo gridded datasets, Roemmich and Gilson's Argo grid dataset is also used in the present study. The horizontal and vertical resolution of this dataset is 1° and 58 layer at 0~2000m, respectively. This dataset is gridded by an optimal interpolation with latitude-dependent decorrelation scales. The first guess field of this optimal interpolation is the monthly mean value calculated from only Argo float data from 2004 to 2009 (Roemmich and Gilson 2009).

### 3.2.2 Atmospheric data

The present study used the monthly-mean sea level pressure and wind stress data of the European Centre for Medium-Range Weather Forecasts (ECMWF) Interim Reanalysis (ERA-Interim; Dee et al. 2011). The spatial grid spacing of ERA-Interim is 0.75°. Brunke et al. (2011) evaluated the performance of various atmospheric reanalysis data, and found that as for wind stress data, the ERA-Interim has the best performance among other products. In this study, to verify the difference between the reanalysis data and observations, a high-resolution version of J-OFURO based on satellite observations was used. The spatial resolution of this dataset is 0.5°. The period analyzed in this study is the same as that of the ocean data, but the J-OFURO covers only from 2004 to 2008

I first calculated monthly climatologies from the 10-year data from 2004 to 2013 for each variable. Monthly anomalies from the long-term climatology were calculated and then were smoothed by applying a 13-month running mean filter. This temporal filter was used to highlight interannual variations.

## 3.3 Variations of the vertical-integrated geostrophic circulation

### 3.3.1 Periodicity

I calculated the time series of the relative vorticity of the depth-integrated velocity averaged in the northwest (NW), northeast (NE) and southern (S) regions in Fig. 3-1, where cyclonic rotation is predominant for the two northern regions and anticyclonic rotation for the southern region in the time mean field (Fig. 3-4). The relative vorticity indicates distinct interannual variations. The meridional and zonal differential components of the relative vorticity are shown in Fig. 3-4 by red and blue lines, respectively. The interannual variations of the relative vorticity in the three regions are mainly attributable to changes in zonal velocity (red lines in Fig. 3-4). The relative vorticity of the depth-integrated velocity in the NW region shows positive values in the periods of 2005~2007 and 2011~2012, and negative values in the period of 2008~2009. The time series in the NE region is similar to that in the NW region but seems to lead by about 1 year. On the other hand, the S region looks out-of-phase with the NW region.

These relationships are confirmed from Fig. 3-5. The correlation between the relative vorticity in the NW and NE regions takes a maximum when the NE region leads the NW region by 1 year (Fig. 3-5a). On the other hand, the lag correlation between the NW and S regions shows the largest negative coefficient without lag times. This result indi-

cates the variation in the S region is in reverse phase with that in the NW region. The lag correlation between these regions also suggests the periodicity of about 5 years.

The periodicity of the relative vorticity of depth-integrated velocity was examined from spectral analysis for the time series in the NW and NE regions. Figure 3-6 shows the ensemble-average power spectra of the relative vorticity estimated from raw spectra of the observed time series at each grid in each region. A significant peak at a period of 5 years can be identified in all the regions. In the NE region (Fig. 3-6b), although another peak appears at periods of about 12 months, it is not statistically significant. The peak at period of 5 years in the NW region (Fig. 3-6a) is slightly larger than that in the NE region (Fig. 3-6b). Therefore, I focus on the interannual variations in the NW region.

### 3.3.2 Spatial characteristics

Figure 3-7 shows the time-latitude section of depth-integrated dynamic height, depth-integrated zonal velocity and relative vorticity of depth-integrated velocity, zonally averaged between 155°W and 145°W in the NW region. The 5-year variations of the relative vorticity is obvious from positive cyclonic rotation at 26~30°N in the periods of 2004~2007 and 2011~2012 and weak cyclonic or anticyclonic rotation in 2009~2010 and 2013 (Fig. 3-7c). The cyclonic rotation at 26~30°N appears almost in coincidence with anticyclonic rotation to the south at 23~26°N in the S region.

The depth-integrated zonal geostrophic velocity (Fig. 3-7b) shows that the simultaneous appearance of the cyclonic rotation in the NW region and the anticyclonic rotation in the S region is closely related to the variations of eastward transport around 26°N near the boundary of the NW and S regions. The area of the eastward transports has 3° width

in latitude, which seems to propagate southward with time from 30°N, and appear to be enhanced around 26°N in 2005~2006 and 2012. The similar southward propagation of the eastward jets has been reported by Richards et al. (2006) from variations of zonal velocity at 400m depth in an ocean general circulation model (Their Fig. 3).

The temporal variations of the eastward transport around 26°N are related with the meridional gradient of depth-integrated dynamic height (Fig. 3-7a). The meridional maximum of depth-integrated dynamic height tends to move to southward with time. These characteristics are common to the results from Roemmich and Gilson's Argo dataset (Fig. 3-8).

I investigate the difference of the vertical structures around 150°W between cyclonic vorticity years and other years (Figs. 3-9, 10). The density and velocity are smoothed with a 13-month running mean to remove seasonal variations and then are averaged at cyclonic years (2004~2007, 2011~2012) and other years (2008~2010, 2013) in the NW region. Figure 3-9 shows the composite meridional sections of zonal velocity, zonally averaged between 155°W and 145°W. As can be seen in Fig. 3-9, the zonal velocity around 26°N is seen to the vertically coherent eastward flow anomaly from sea surface to 1500m. The vertically coherent change of density along the southern side of 26°N is thought to be the cause of the vertically coherent eastward flow at 26°N (Fig. 3-10). In particular, the density at upper of 200m in the southern (northern) side of 26°N siginificantly decreased (increased) in the cyclonic years (Fig. 3-10a). The significant difference between the cyclonic years and other years along the southern side of 26°N can be confirmed above the upper pycnocline and at depths deeper than 800m (Fig. 3-10c).

I investigate the difference of the horizontal map of the depth-integrated circulation between the cyclonic years and other years. Figure 3-11 shows the composite maps of the relative vorticity of depth-integrated velocity for the cyclonic years and other years and

their difference. In the cyclonic years there is a zonally-extending pair of cyclonic rotation at 26~30°N and anticyclonic rotation at 23~26°N (Fig. 3-11a). On the other hand, they are obscure in the other years (Fig. 3-11b). The difference of the relative vorticity are statistically significant in the NW and NE regions and the S regions

I calculate the composite map of the depth-integrated zonal velocity to investigate the relationship of the flow fields to the cyclonic and anticyclonic rotations (Fig. 3-12). The northern cyclonic rotation and southern anticyclonic rotations in the eastern subtropical region are associated with relatively strong eastward flow between them. This eastward flow is centered at 26°N, 150°W with 3° in meridional width and from 165°W to 140°W for the cyclonic years (Fig. 3-12a). On the other hand, for the other years, the westward zonal velocity is seen to the south of 30°N and the west of 140°W (Fig. 3-12b). The difference map in Fig. 3.12c shows that a statistically significant eastward flow anomaly around 26°N reachs to 160°E in the cyclonic years. For the cyclonic rotation years (other years), the zero lines of zonal velocity, which corresponds to the gyre axis in Chapter 2, tend to be located to the south (north) at least toward the eastern side of 160°E.

To investigate the cause of the eastward transport at 26°N, I prepare the composite map of the depth-integrated dynamic height (Fig. 3-13). The difference map between the cyclonic years and other years in Fig. 3-13c reveals statistically significant differences in the southern region of the eastward transports at 26°N (170°W~140°W, 23°N~25°N) and the Kuroshio recirculation region in the western North Pacific (130°E~150°E, 25°N～30°N), showing a general pattern with negative anomaly in the northern side of the subtropical gyre and positive in the southern side. This result indicate that the variations of the eastward flow at 26°N is caused predominantly by the variations of the depth-integrated dynamic height in the southern side.

Which temporal variations of the southern and northern region of 26°N cause changes in the eastward flow near 26°N? To approach this point, I first calculated the time series of the zonal velocity based on the geostrophic relation from the difference between the depth-integrated dynamic height meridionally averaged in the southern side (23°N~26°N) and northern side (27°N~30°N) of this eastward flow, and then they are compared to the actual time series of the depth-integrated zonal geostrophic velocity along 26°N (Fig. 3-14). The correlation coefficient at each longitude between them is statistically significant at all longitudes (Fig. 3-14c). This result indicates that the eastward flow along 26°N is well reproduced by the depth-integrated dynamic height.

Next, I prepare the long-term mean of the depth-integrated dynamic height in each longitude range in the northern and southern regions of 26$^{o}$N. Then I compute the two time series of the zonal velocity assuming geostrophy from the long-term mean of the southern (northern) region and the original northern (southern) depth-integrated dynamic height (Fig. 3-15c,d). The correlation coefficient at each longitude between these time series and the actual depth-integrated zonal velocity along 26°N is shown in Fig. 3-15a,b. In the region of 180~140°W, the correlation coefficient calculated from the mean dynamic height of the northern region (Fig. 3-15a) is generally higher than that from the southern region (Fig. 3-15b). Although the time series from the mean dynamic height of the northern region is almost coincide with that of actual depth-integrated zonal velocity along 26°N, they seem to be not necessarily in agreement since 2011.To the west of 180°, the correlation coefficient becomes high for the time series from the mean dynamic height of the southern region (Fig. 3-15b). The results indicate that the variations of the zonal velocity at 26°N in the western region are determined predominantly by those of the depth-integrated dynamic height in the northern region, where is close to the latitudinal band of the center of Kuroshio recirculation.

Lagged regression maps between the depth-integrated dynamic height and its area-mean at (23°N~25°N, 155°W~145°W) appear to generally propagate southward from the northern side of the subtropical gyre (Fig. 3-16). This southward propagation is clearly seen from the lagged regression maps of the depth-integrated zonal velocity (Fig. 3-17), which shows that the zonal structures with 3° in meridional width and more than 20° in longitudinal length propagate southwestward from 30°N. These characteristic of southwestward propagation resemble the structure and variation of zonal jets and striations in the eastern part of the North Pacific (Richards et al. 2006, 2008; Maximenko et al. 2008; Melnichenko et al. 2010; Nonaka et al. 2012) and South Pacific (Kessler and Gourdeau 2006; Taguchi et al. 2012). In fact, these northeast-southwest propagations of the zonal velocity anomaly can be also confirmed from the time-latitude section of zonal velocity (Fig. 3-7) and the yearly maps of its anomaly (Fig. 3-18).

### 3.3.3 Relationship with the wind-driven circulation

To compare between depth-integrated geostrophic circulation and wind-driven circulation, I observe the time series of wind-driven transport, zonal wind-driven transport and relative vorticity of the wind-driven transport zonally averaged between 155°W and 145°W (Fig. 3-19). The variations of the eastward flow around 26°N as such the depth-integrated zonal velocity can be confirmed from the zonal wind-driven transport. The eastward flow around 26°N is evident in 2003~2006, 2009~2011 and propagated to the southward. To compare with the satellite observation wind stress data, the time series calculated from J-OFURO in the same way as ERA-Interim is also checked (Fig. 3-20). Although spatially fine scales differ, the variations of the eastward flow around 26°N, which propagated southward and was strengthened in 2006, is almost consistent with the

ERA-Interim. These satellite results corroborate the variations of the eastward flow based on the ERA-Interim.

The time series of the zonal wind-driven transport averaged in the region of 25~27°N and 155°W~145°W is compared to that of the depth-integrated zonal velocity (Fig. 3-21). Although they show similar fluctuations, the time series of the zonal wind-driven transports appear to lead the depth-integrated zonal velocity time series. The leads are confirmed from Fig. 3-21b, which indicates that the maximum correlation between them occurs when the zonal wind-driven transport leads the depth-integrated zonal velocity time series by 1 year. The results indicate that the depth-integrated geostrophic circulation around 26°N in the eastern subtropical gyre can be explained by wind-driven circulation with a 1 year lag. This time lag corresponds to about pi/2 of the dominant variations of about 5 years. We will discuss the mechanism later in Section 3.5.

I analyze the composite map of the Ekman pumping velocity for eastward flow years (2004~2006, 2009~2011) and other years (2007~2008, 2012~2013) (Fig. 3-22). The Ekman pumping velocity in the southern region of 26°N is enhanced for the eastward flow years (Fig. 3-22c), consistent with the result that the variations of the eastward flow around 26°N are mainly caused by the depth-integrated dynamic height in the southern region of 26$^{o}$N (Section 3.3.1).

Difference between the sea level pressure in the eastward wind-driven transport years and other years shows positive and negative anomaly in the western and eastern subtropical gyre, respectively (Fig. 3-23). These regions may correspond to the subtropical high and Ogasawara high. The results indicate that strong negative Ekman pumping velocity anomaly in the southern side of 26°N in the eastern region is not due to the large scale atmospheric variations, probably due to local atmospheric forcing

## 3.4 Variations of the vertical structures of geostrophic circulation

In this section, I first describe to the interannual variation of the gyre axis at each depth. Next, I investigate the vertical structures of the velocity and potential vorticity, and then describe the relationship with the northward shift of the gyre axis.

The year-to-year variations of the gyre axis are shown at each depth in Fig. 3-24. As seen from the mean distribution of the gyre axis in Chapter 2, the northward shift of the gyre axis with depth occurs mainly to the east of 170$^{o}$E almost every year. To the west of 170$^{o}$E, there is little change in positions of the gyre axis with depth, but a careful look shows a weak but recognizable change in the position of the gyre axis after 2010.

The vertical structures of the gyre axis around 170°E seem to be related to the strong eastward-flowing Kuroshio Extension (shades in Fig. 3-24). Figure 3-25 shows the time-latitude section of the depth-integrated zonal velocity anomaly zonally averaged between 165°E and 175°E. The meridional extent of the northward shift of the gyre axis with depth is related with the depth-integrated zonal velocity anomaly of the Kuroshio Extension around 30°N. When the northward shift of gyre axis is small in 2007~2008, the Kuroshio Extension around 30°N is strong, while it is weak when the northward shift of gyre axis is large in 2009~2010. The signals are seen uniformly in the vertical from the sea surface to deep layer at 1500m depth (Fig. 3-26). The results indicate that the gyre axis structures in the downstream of the Kuroshio Extension is dominated by the strength of the barotropic flow of the Kuroshio Extension. In the southern side of 30°N, the depth-integrated zonal velocity anomaly propagates to southward as such 3.3.1. This southward propagation may be related to the signals of zonal velocity anomaly shown in Section 3.3.1.

Next, I investigate the distribution of the gyre axis at each depth in the eastern subtropical gyre. Figure 3-27 shows the meridional section of zonal geostrophic velocity at 160°W in each year. In the east of 170°E, the interannual variations of the gyre axis are noticeably seen at 200~600m in which the vertical gradient and the position of the gyre axis vary from year to year. In the surface layer from sea surface to 400m depth, the gyre axis is located at about 25°N, perhaps associated with the strength and vertical extent of the eastern STCC. In the layer deeper than 1000m, the gyre axis almost stays at 40°N, showing less year-to-year variations.

In the mean field, I showed the relationship with the CMW characterized by the low PV and the northward shift of the gyre axis (Section 2.4). We may expect that higher (lower)-PV CMW could cause more uniform (non-uniform) northward shift of the gyre axis with depth. I investigate the relationship between the temporal changes of the vertical structure of the gyre axis and CMW. I first observe the PV map on the 1026.2 $kgm^{-3}$ isopycnal surface as representative density surface of the CMW (Fig. 3-28), which reveals year-to-year variations of the horizontal structure and strength of low PV CMW. Although the low PV appears to be supplied from the outcrop region in 2005 and 2010, the PV around 30°N and 170°W~150°W in the downstream side of the outcrop region is relative high in 2010. It is thought that the low PV water in the previous year was advected toward the downstream and dissipated.

The meridional sections of the PV and zonal velocity in each year at 160°W are shown in Fig. 3-29. When the PV in the depth at 200~800m of the CMW layer is relatively lower (higher), the northward shift of the gyre axis tends to be smaller (larger). In 2006~2008, the PV at 200~600m depth is generally low around 30°N, and the northward shift of the gyre axis with depth is also small. In 2009 and 2012, it was an opposite situation. But the relationship between the CMW and the gyre shift in 2010, 2011 and 2013 is

not consistent with the above-mentioned story. The results imply that the northward shift of the gyre axis with depth is related to not only by the intensity of PV of the CMW but also by other ocean structures.

In the western subtropical gyre, the relationship between the northward shift of the gyre axis and the PV structures is not clear (Fig. 3-30). The relatively higher PV water of the pycnocline at depths of 300~600 m around 30°N is relatively higher (lower) in 2009~2012 (2005~2008). The PV of STMW above the pycnocline appears to vary with the out of phase to it. When the northward shift of the gyre axis is large, the velocity in the upper layer of the Kuroshio Extension tends to be weak. The results indicate that the variations of the northward shift of the gyre axis are determined predominantly by the variations of barotropic flow of Kuroshio Extension rather than the PV structures.

## 3.5 Summary and discussion

In this chapter, the temporal variations of the depth-integrated circulation of the North Pacific subtropical gyre were investigated with a focus on the local cyclonic rotation in the eastern subtropical gyre, which found from an analysis of the mean current field in Chapter 2. I also investigated the vertical structures of the gyre axis and their relationship with velocity and potential vorticity structures.

The cyclonic rotation between the two gyre axes of the depth-integrated dynamic height in the east of 170°W shows interannual variations with a period of about 5 years and no significant seasonal variations. The anticyclonic rotation is seen to the south of the cyclonic rotation area, varying coincidentally with the cyclonic rotation. I investigated the two local cyclonic rotation regions, the NW and NE regions, with a local peak of the relative vorticity of the depth-integrated geostrophic velocity. The variations of the

relative vorticity of the depth-integrated velocity in the NE region lead to those of the NW region by about 1 year, which suggests that they may be affected by a westward-propagating baroclinic Rossby wave.

To examine the horizontal and vertical characteristic of the cyclonic rotations in the eastern subtropical gyre, I calculated the composite sections and maps. The results show that the cyclonic and its associated anticyclonic rotations to the south were caused by a vertically coherent eastward flow in 26°N near the boundary of them and this eastward flow is mainly associated with the variations of the depth-integrated dynamic height in the southern region of the eastward flow. Lagged regression analysis indicated that the signals of depth-integrated dynamic height and zonal velocity anomaly were propagated southwestward from the northeastern subtropical gyre and were enhanced along around 26$^{o}$N.

Comparison between the depth-integrated zonal velocity and zonal wind-driven transport indicates that the depth-integrated geostrophic circulation was explained in terms of wind-driven circulation, though there is a time lag between them; the variations of the wind-driven transport lead the depth-integrated zonal velocity by 1 year. When the eastward wind-driven transport at 26°N was obvious, the Ekman pumping velocity along the southern side was enhanced, causing strong vertically-integrated eastward geostrophic flow. It is found that the interannual variations of the cyclonic and anticyclonic circulation were induced by local wind changes rather than by large-scale atmospheric forcing.

Taguchi et al. (2012) indicated from an analysis of a coupled atmosphere-ocean general circulation model that the variations of striation of depth-integrated zonal velocity in the South Pacific subtropical region was consistent with that of the zonal Sverdrup transport with lag by 1 year. He suggested that coincidence of striation between

depth-integrated velocity and Sverdrup transport was caused by positive air-sea feedback via SST. The equatorward propagation speed of the striation showed by Taguchi et al. (2012) was 0.18~0.56 $cms^{-1}$, which was consistent with the propagation speed estimated from the present study (0.42 $cms^{-1}$), though the latitude range is different, and 1 year lag between the eastward flow of depth-integrated zonal velocity and the Sverdrup transport was also consistent with the result of present study (Fig. 3-21).

Why is there the time lag between the depth-integrated zonal velocity and the zonal wind-driven transports? We take a look back at the barotropic vorticity equation (Eq. 1-6) and consider a time-dependent Sverdrup relation. Here, I assume a balance between the time-dependent terms of the relative vorticity and the forcing due to the Ekman pumping,

$$\frac{\partial \zeta}{\partial t} \approx \frac{f}{D} w_E . \qquad (3\text{-}1)$$

Since the time change of the relative vorticity in the eastern region is mainly attributed to the change of the zonal velocity (Section 3.3.1), Eq. (3-1) is approximated as follow:

$$\frac{\partial u}{\partial t} \approx \frac{f}{D} w_E . \qquad (3\text{-}2)$$

This equation suggests that the temporal variations of the depth-integrated geostrophic circulation can be explained by the form of the temporal integration of the Ekman forcing. To verify their relationship, I calculated the temporal integration of the wind-driven transport that may be regarded to correspond to the Ekman pumping velocity in Eq. (3-2) (Fig. 3-1). The change of the integrated zonal wind-driven transports is almost in agreement with that of the depth-integrated zonal velocity. The result suggests that the time rate of the change in the eastward flow responds to the wind stress curl forcing.

The above-mentioned discussion considered only the response to the local wind forcing at the same place, but the eastward flow could also form due to the infusion of

the higher PV into the southern region of the eastward flow at 26°N. This infused PV could be formed by the Ekman pumping at the outcrop of isopycnal surfaces, which are usually located to the upstream side of 26°N. We need to further examine the mechanism of the time changes in the eastward flow in detail.

The eastward flow anomaly propagated southwestward seems to be enhanced around 26°N on the year-to-year time scales, and the local intensification plays an essential role in the formation of the local cyclonic and anticyclonic circulations and the in-between depth-integrated eastward flow. Kobashi and Xie (2012) pointed out that the interannual variations of the STCC in spring in the western subtropical gyre are associated with an overlying local cyclonic wind curl, and the changes in the cyclonic wind curl is induced by the sea surface temperature (SST) front anchored by the STCC itself. On the other hand, the present study finds the changes in the depth-integrated eastward flow along the eastern STCC in response to the local cyclonic wind curl. Since the eastern STCC also has a SST front, there may be possible feedback between the atmosphere and ocean, that is, the changes in the SST front give rise to those of the wind curl forcing, and then they again change the eastward flow. Further analysis will be needed to understand the whole process of the changes in the eastward flow. The year-to-year variations of the northward shift of the gyre axis with depth were seen both in the eastern and western regions of 170°E. In the downstream region of the Kuroshio Extension, the northward shift of the gyre axis was large after 2009, which was related to the strength of the Kuroshio Extension. On the other hand, in the eastern part of the subtropical gyre, I found that the variations of the position of the gyre axis were large at subsurface layer of the 200~800m depth, small at depth of 0~200m and deeper than 1000m. The position of the gyre axis in the upper layer was located in the southern edge of the eastern STCC. I suggested that

the position of the gyre axis in the upper layer in the eastern subtropical gyre was associated with vertical extent and meridional position of the eastern STCC.

I investigated the relationship between the variations of the gyre axis and PV structures in the eastern and western subtropical gyres. In the eastern region, when the CMW is located near the position of the mean gyre axis, the northward shift of the gyre axis with depth tend to be small in the CMW layer, but such relationship is not always seen. The results suggested that the vertical structures of the gyre axis are affected not only by the intensity and distribution of the CMW but also by other ocean structures. On the other hand, in the west at 160°E, I found that the northward shift of the gyre shift is related to the upper velocity of Kuroshio Extension rather than PV structures.

The quantitative analysis for the temporal variations of the vertical structure of the subtropical gyre will be necessary for a further understanding in the future.

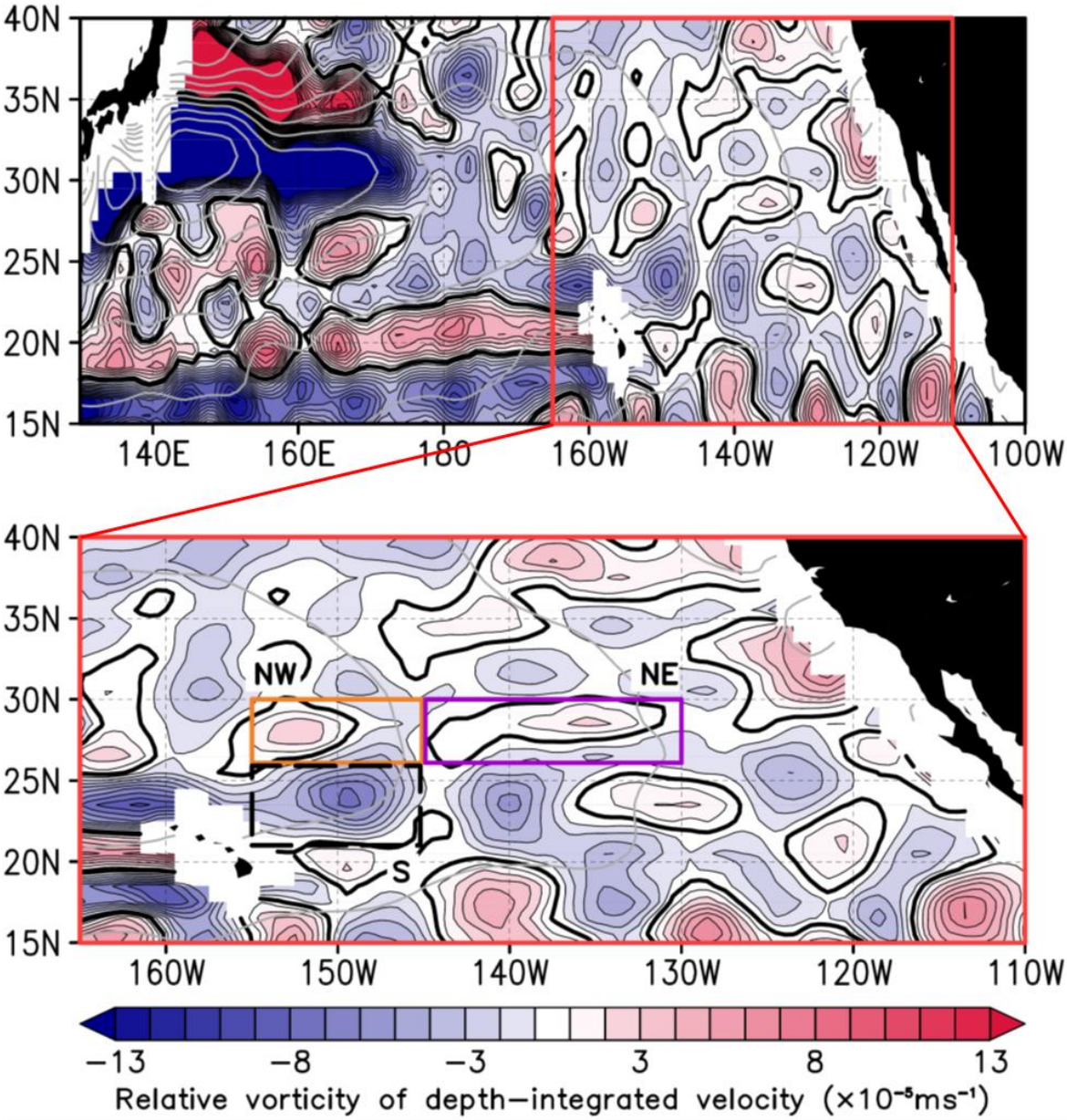


Fig.3-1. Mean map of relative vorticity of depth-integrated geostrophic velocity referenced to 2000 dbar, averaged for the period from 2004 to 2013. Gray contours indicate depth-integrated dynamic height ($m^2$). The rectangles are used in Fig. 3-4.

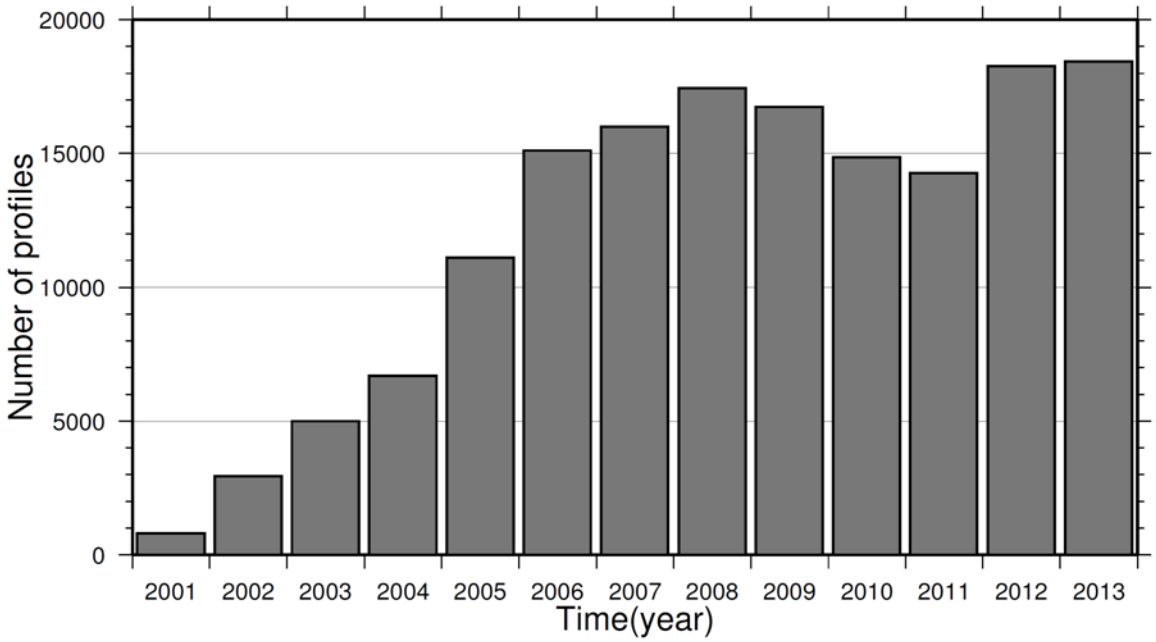


Fig.3-2. Number of Argo profiling floats in the North Pacific subtropical region (15°~45°N, 120°E~100°W).

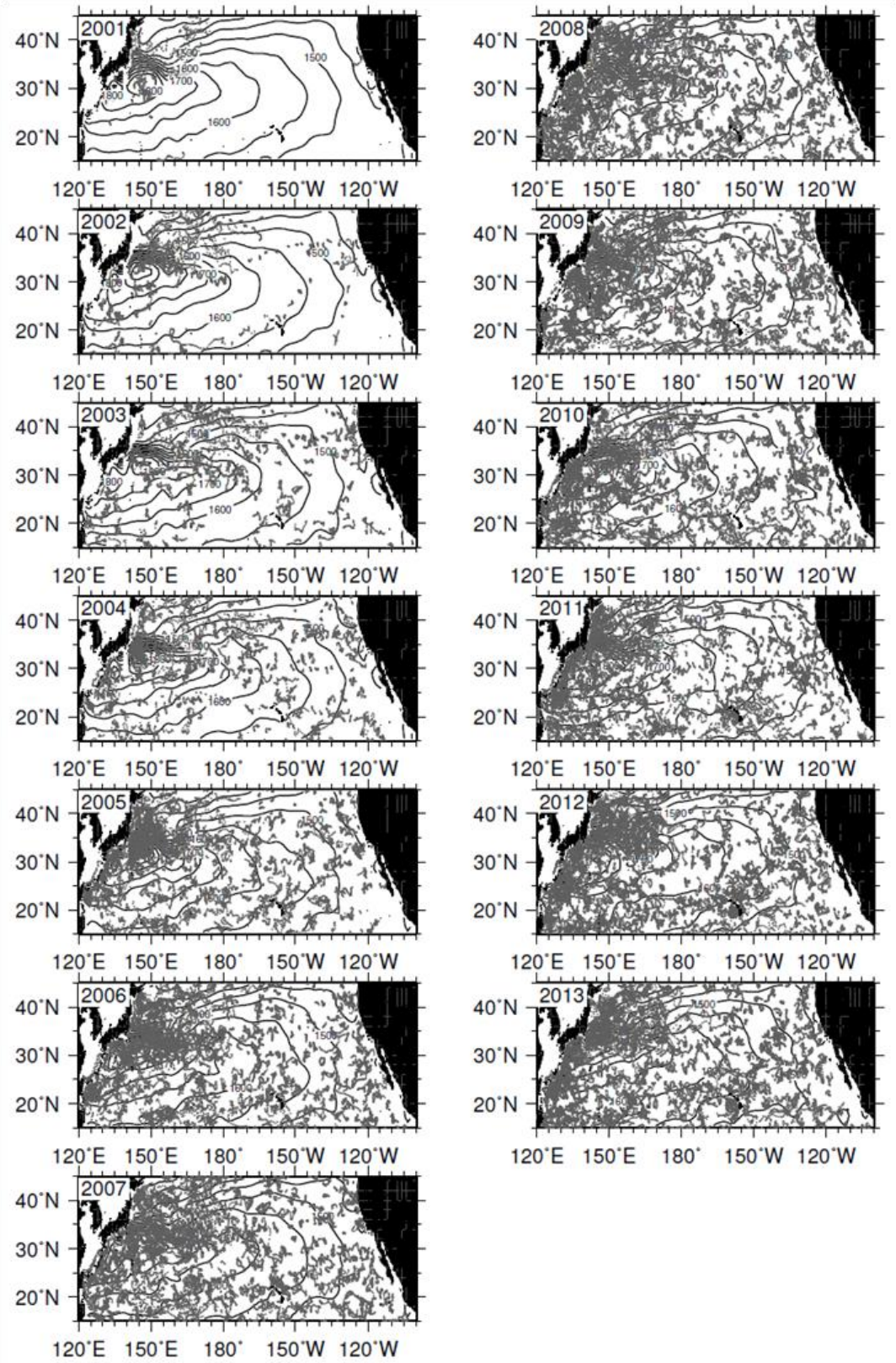


Fig.3-3. Spatial distributions of Argo profiling floats at each year. The upper left number in each panel show the year. Contours indicate depth-integrated dynamic height referenced to 2000 dbar from the MOAA GPV.

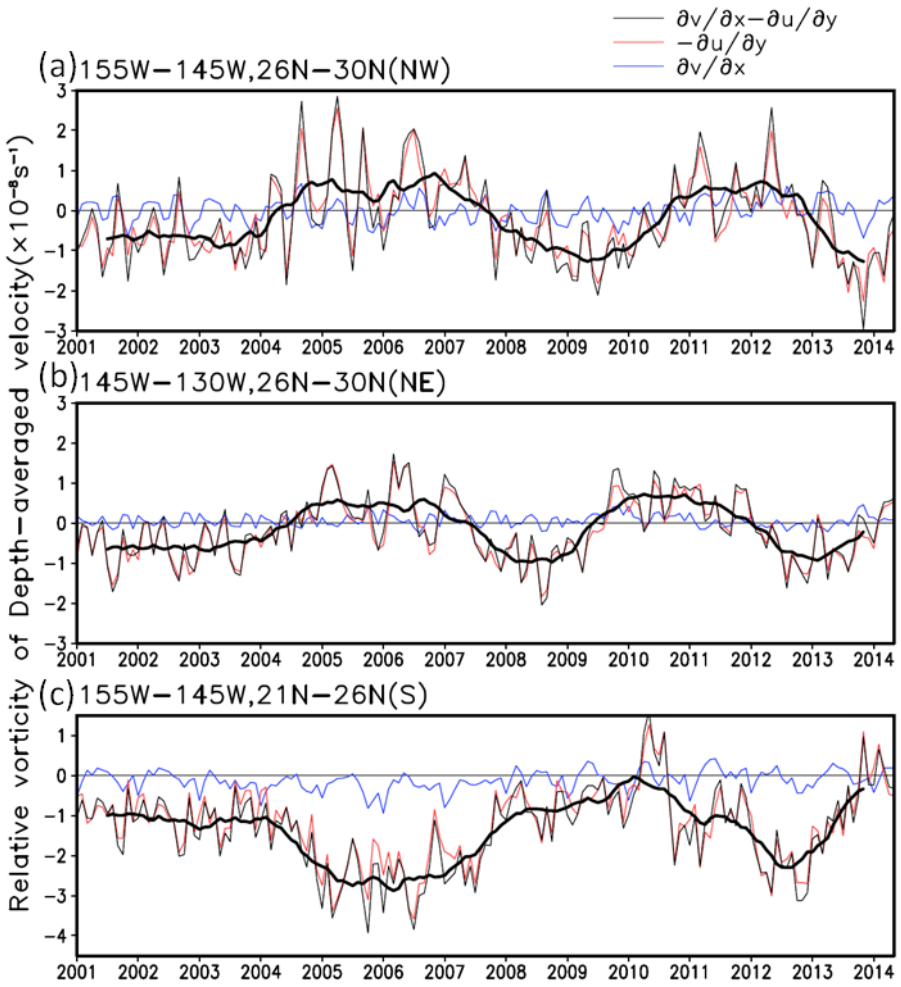


Fig.3-4. Time series of the relative vorticity of depth-averaged geostrophic velocity averaged in the (a) NW, (b) NE and (c) S regions. Black and red (blue) lines indicate relative vorticity and its meridional (zonal) differential term, respectively. Thick black lines indicate a 13-month running mean of the relative vorticity. .

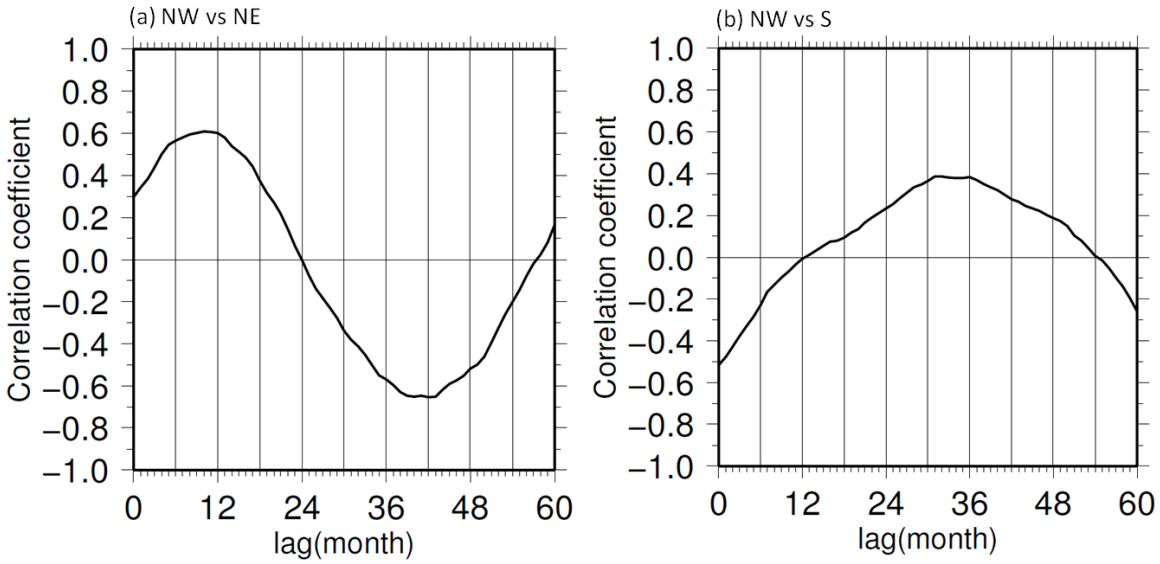


Fig.3-5. Lagged correlation between the time series of the relative vorticity of depth-averaged velocity in the (a)NW and NE regions (Figs. 3-4a, b) and the (b)NW and S regions (Figs. 3-4a, c). Here, the lagged correlation is estimated from the time series of 13 month running mean values (thick black lines in Fig. 3-4). A positive lag denotes the lead by the NW time series. With the number of degrees of freedom estimated as 6 from Fig. 3-4, the correlation is significant at 90% confidence level when $|r| > 0.51$.

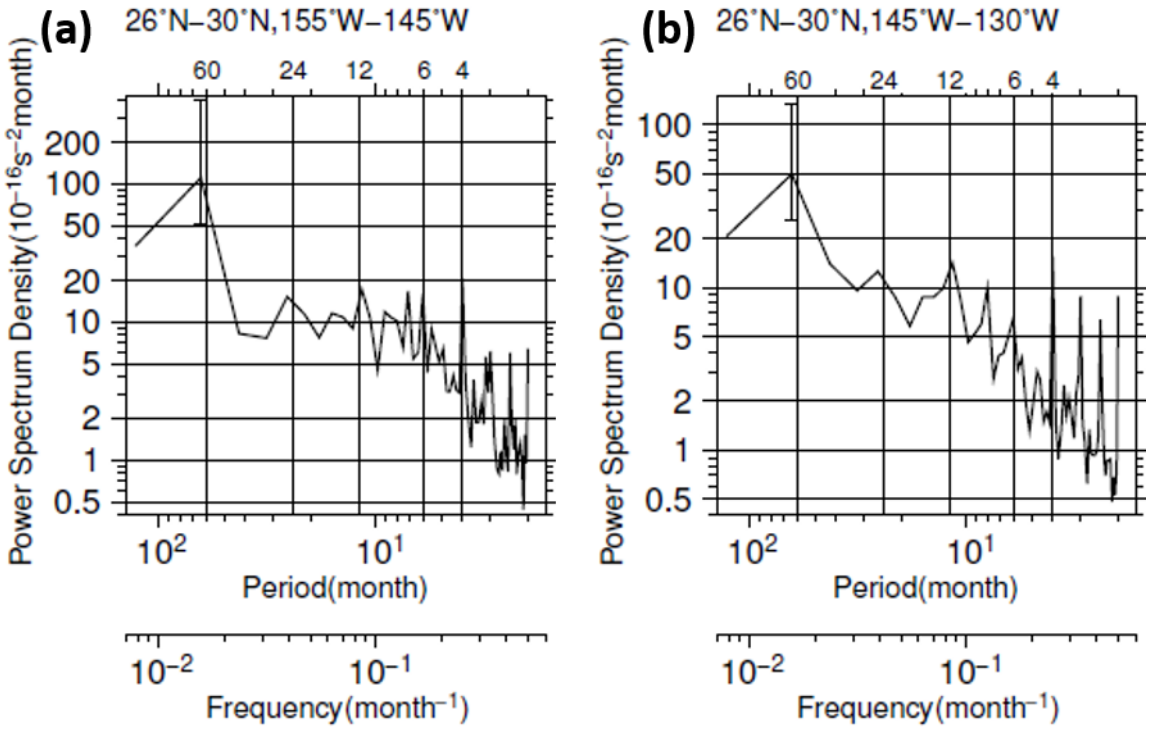


Fig.3-6. Ensemble mean power spectra of the relative vorticity of depth-integrated velocity in the (a)NW and (b)NE regions. Error bars are 95% confidence interval with 12 degrees of freedom. The vertical lines denote 4, 6, 12, 24 and 60 months.

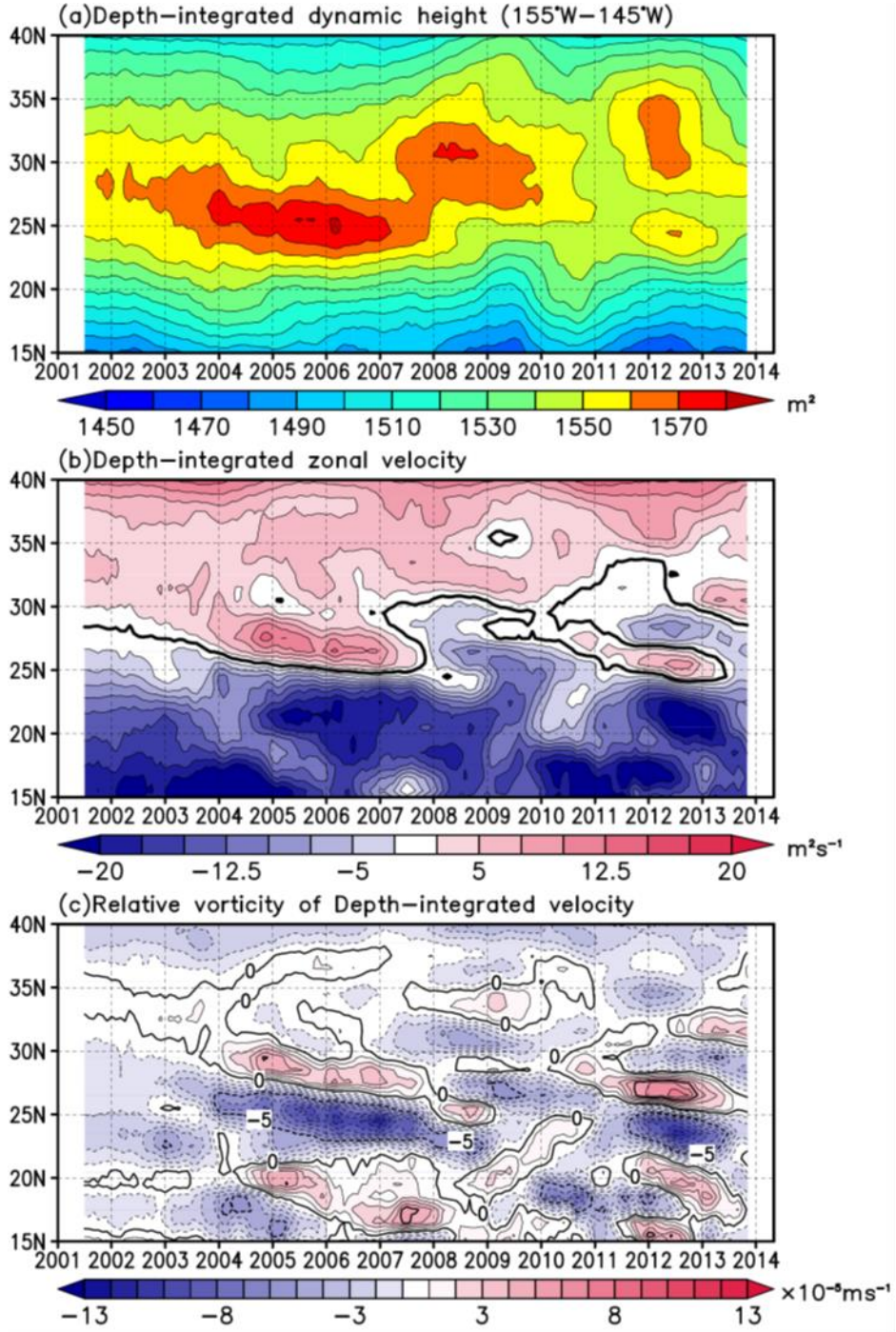


Fig.3-7. Time series of (a) depth-integrated dynamic height, (b) depth-integrated zonal geostrophic velocity and (c) Relative vorticity of depth-integrated geostrophic velocity, zonally averaged between 155°W and 145°W.

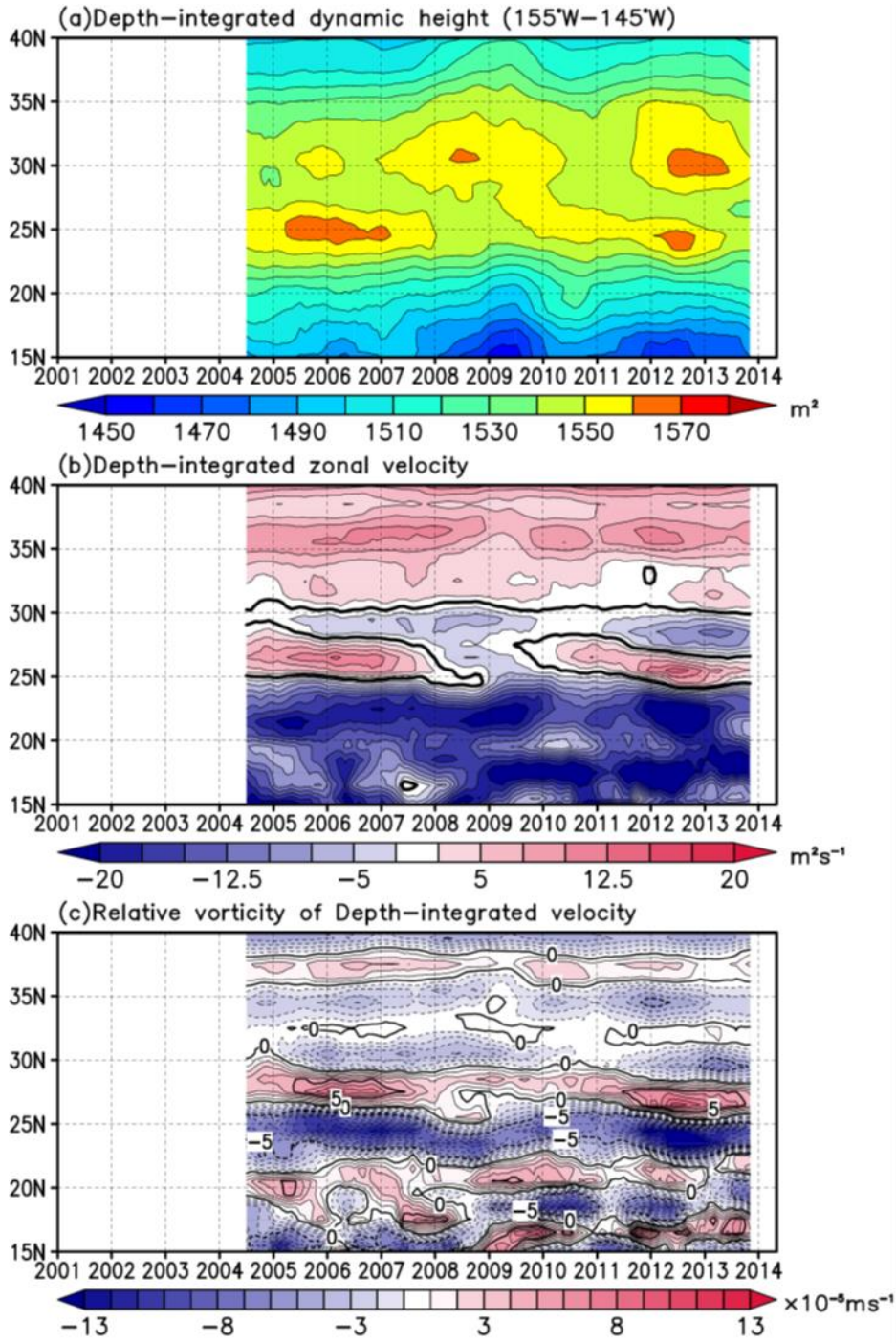


Fig.3-8. Same as in Fig. 3-7, but calculated by using Roemmich and Gilson Argo dataset.

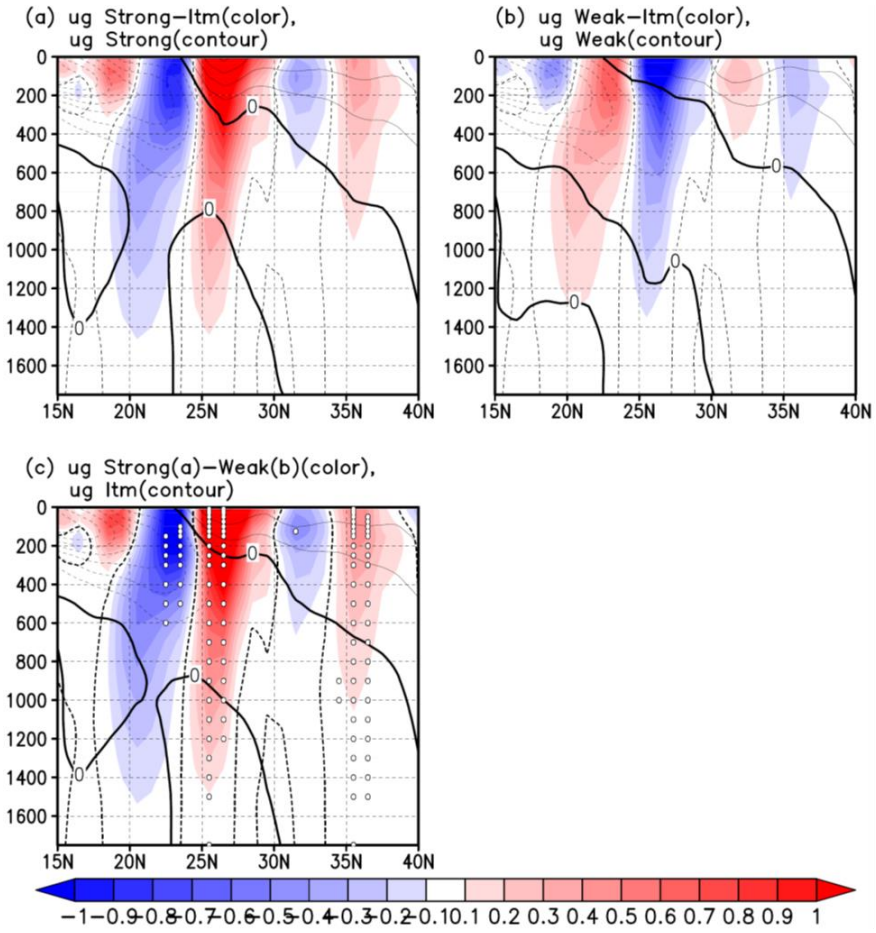


Fig.3-9. (a) Latitude-depth sections of zonal geostrophic velocity ($cms^{-1}$, contours) during the local cyclonic rotation years of 2004~2007 and 2011~2012 and its anomaly from the mean from 2004 to 2013(color shading), zonally averaged between 155°W and 145°W. The geostrophic velocity is referenced to 2000 dbar. (b) Same as (a) except for during the other years of 2008~2010 and 2013. (c) The difference between the maps in zonal geostrophic velocity of (a) local cyclonic years and (b) non-local cyclonic years (color) and its annual mean from 2004 to 2013 (contours). In (c) the open circles show significant difference at 90 % confidence limit.

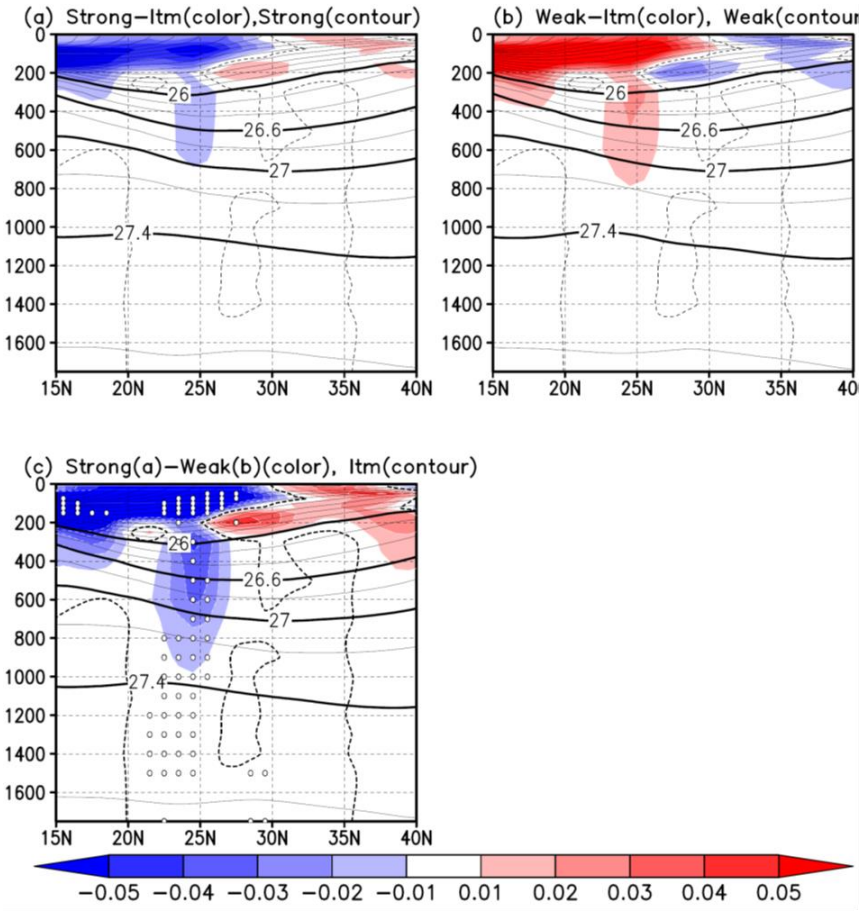


Fig.3-10. Same as in Fig. 3-9, but for density.

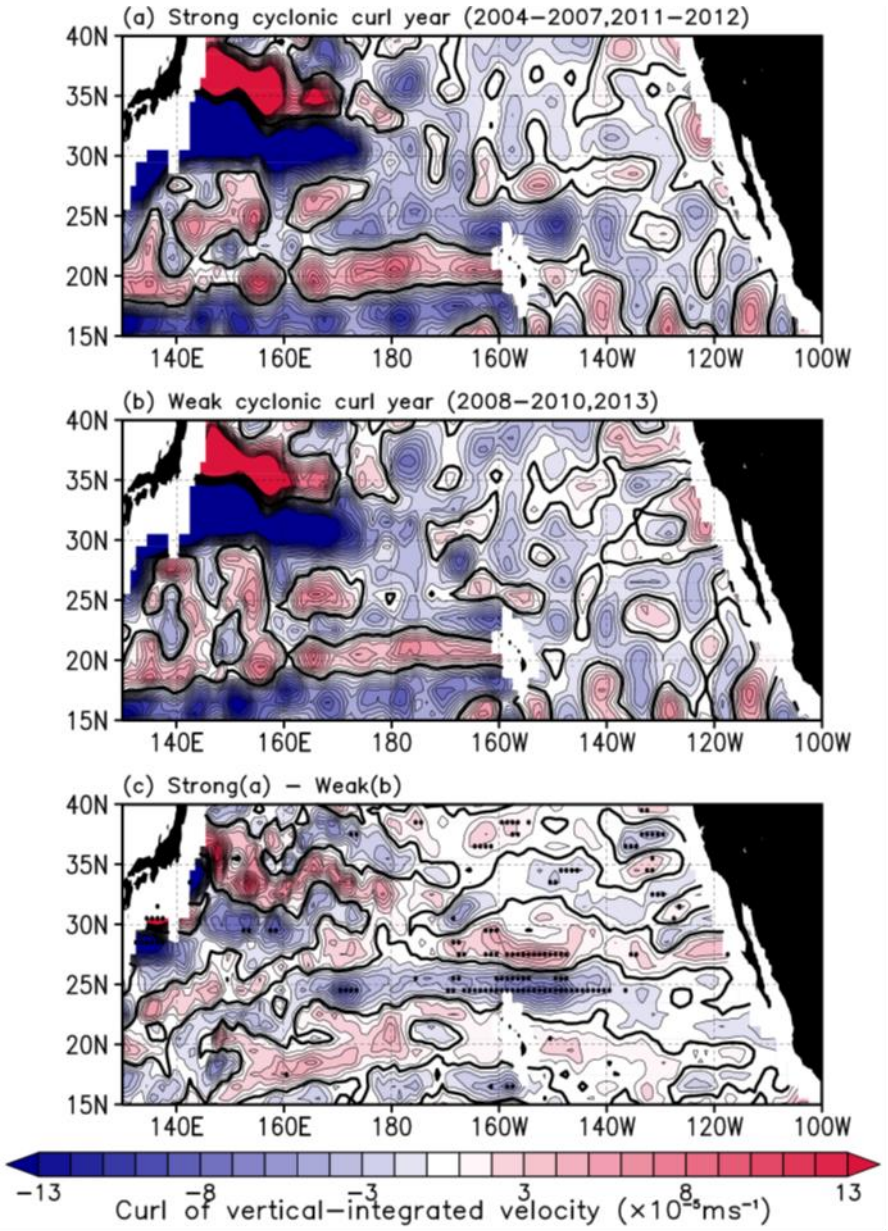


Fig.3-11. Composite maps of relative vorticity of the depth-integrated geostrophic velocity in (a) the local cyclonic rotation years (2004~2007 and 2011~2012) and (b) the other years (2008~2010 and 2013). (c) Difference between the maps of the relative vorticity of the depth-integrated geostrophic velocity in the (a) local cyclonic rotation years and (b) the other years. In (c), black dots show significant difference at 90% confidence limit.

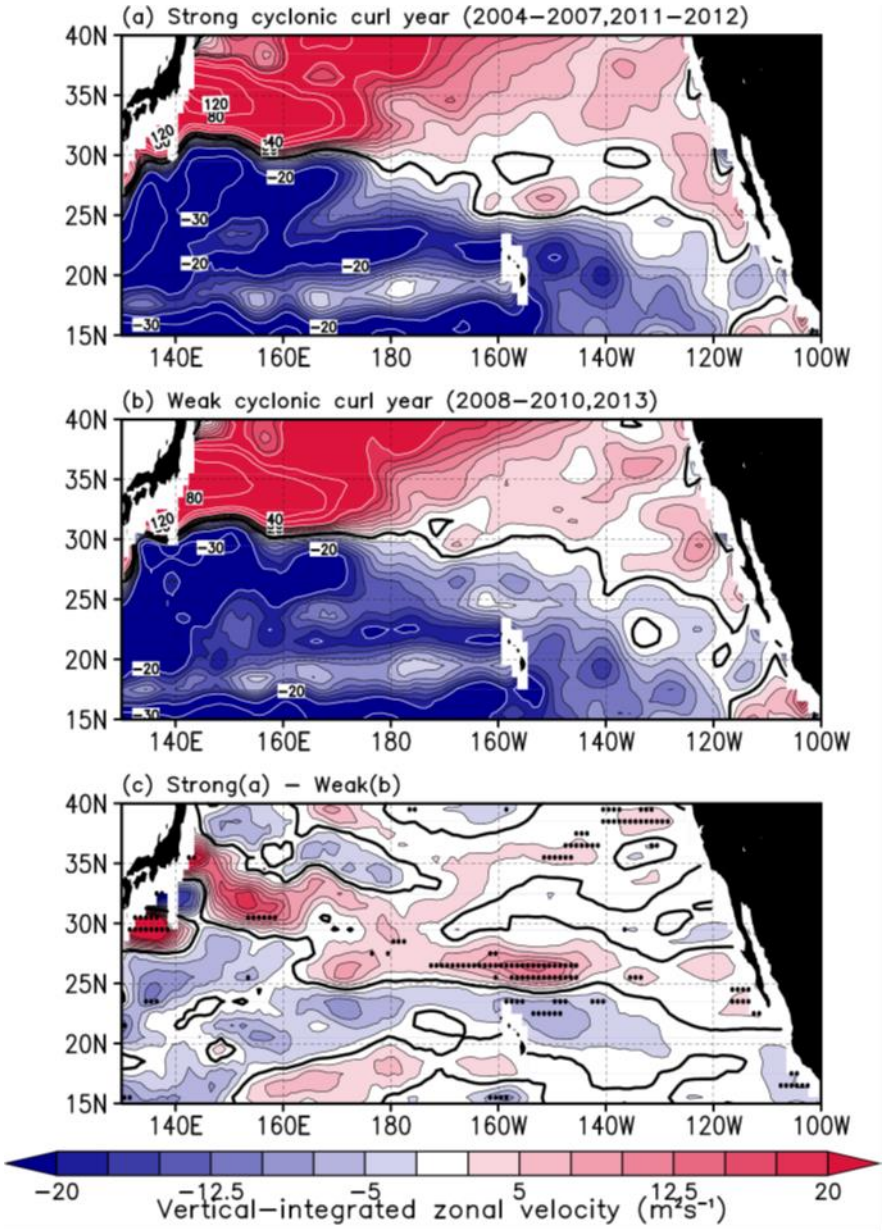


Fig.3-12. Same as in Fig. 3-11, but for the depth-integrated zonal velocity.

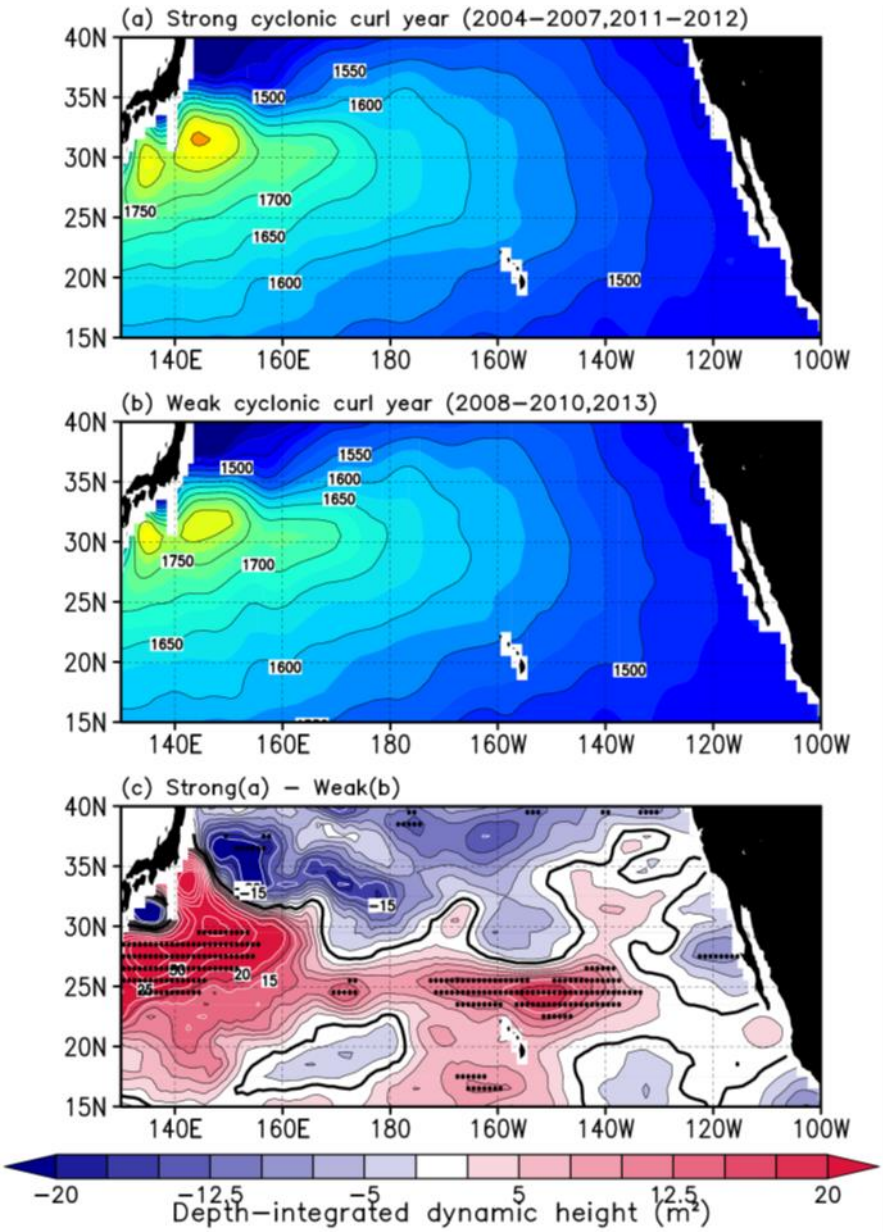


Fig.3-13. Same as in Fig. 3-11, but for the depth-integrated dynamic height.

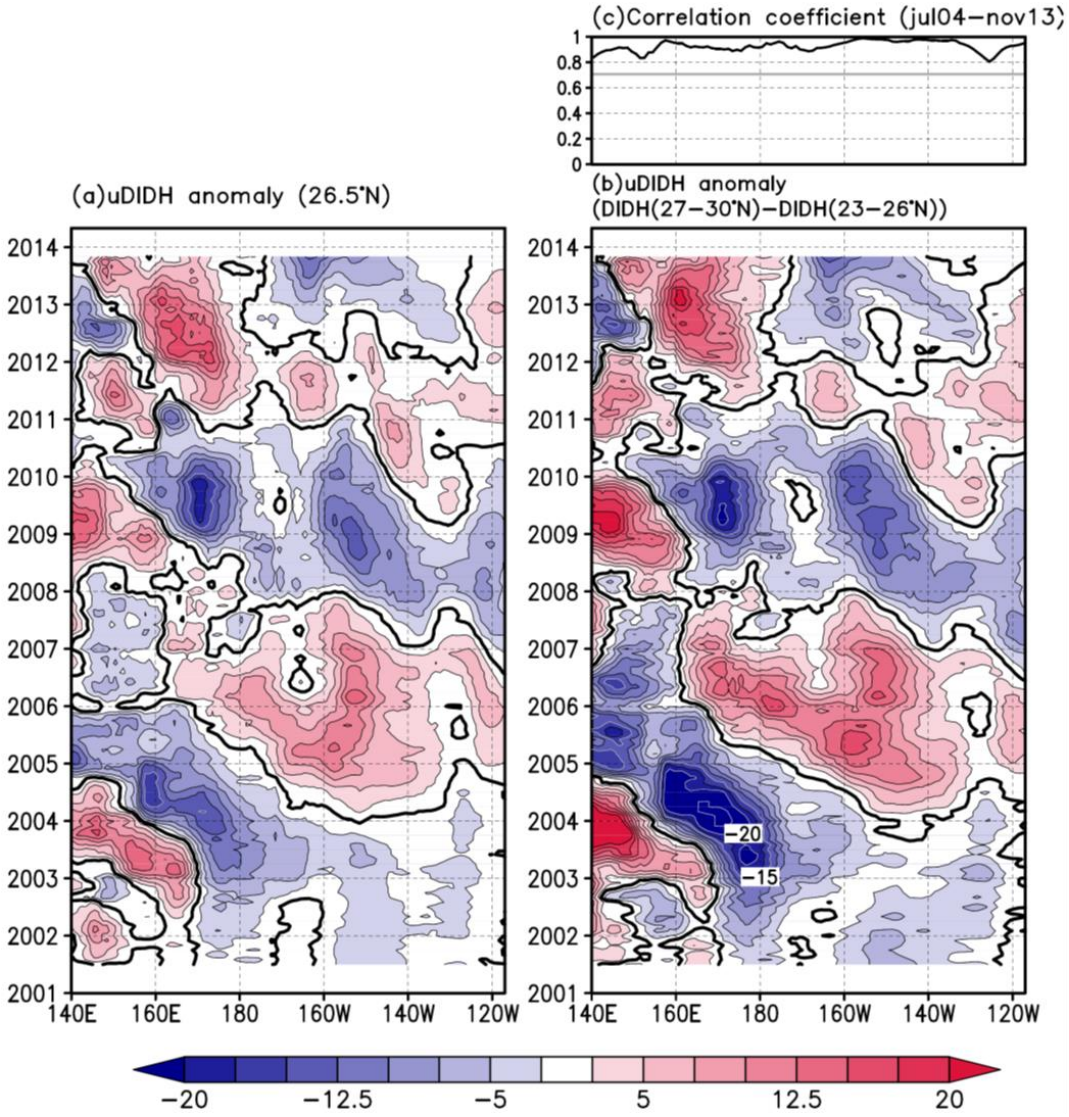


Fig.3-14. (a) Longitude-time section of the depth-integrated zonal velocity anomaly along 26°N. (b) Same as (a) but calculated based on the geostrophy from the difference between the depth-integrated dynamic height meridionally averaged in the southern side (23°N~26°N) and the northern side (27°N~30°N). (c) The correlation coefficient at each longitude between the time series in (a) and (b). Correlation exceeding the gray line is significant at 95% confidence limit.

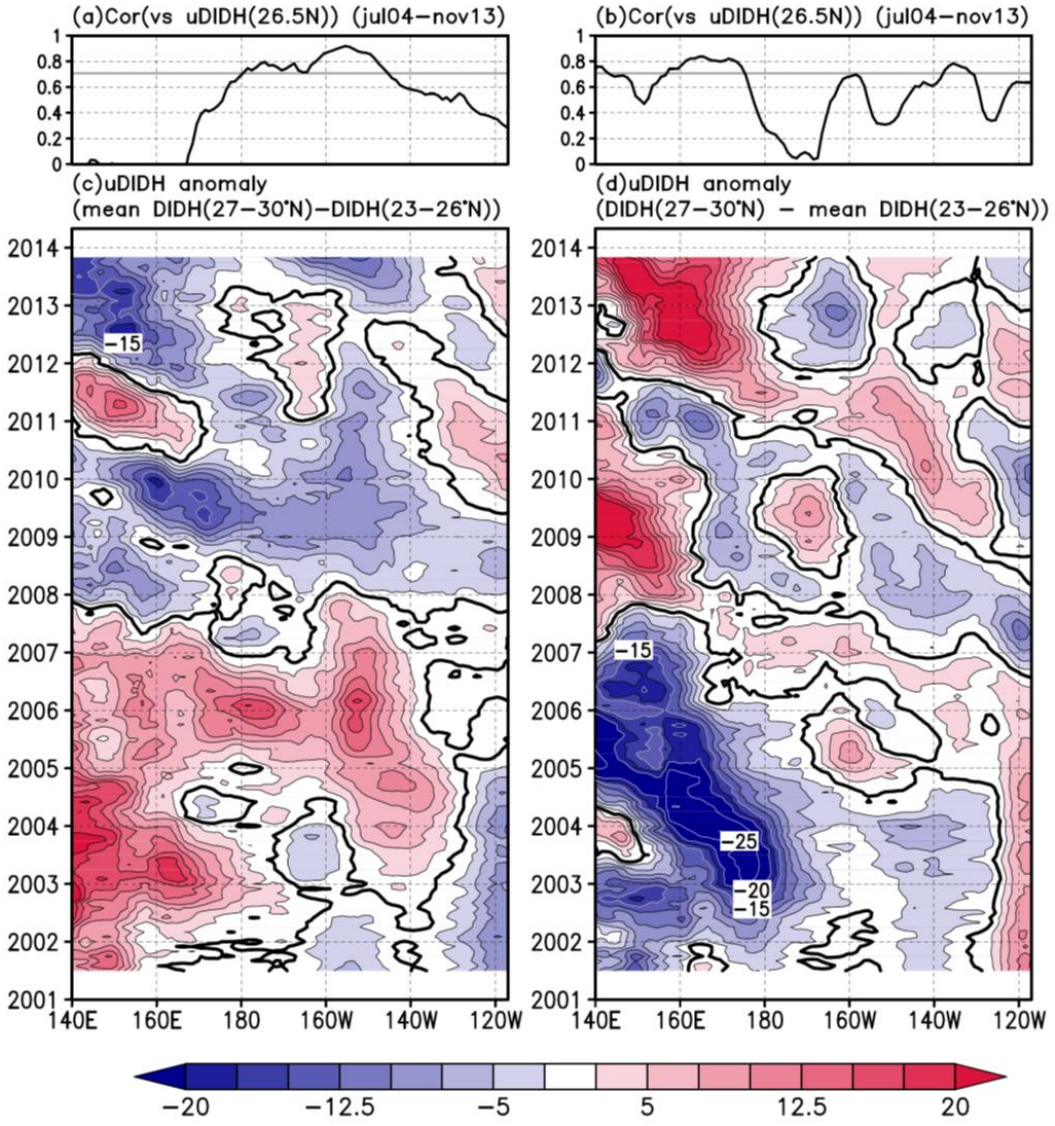


Fig.3-15. Same as in Fig. 3-14, but calculated from the combination of the depth-integrated dynamic height and its long-term mean in (c) the northern region and (d) the southern region. The correlation coefficient between the time series in (c) and (d) and the actual one along 26°N in Fig. 3-14a is shown in (a) and (b), respectively.

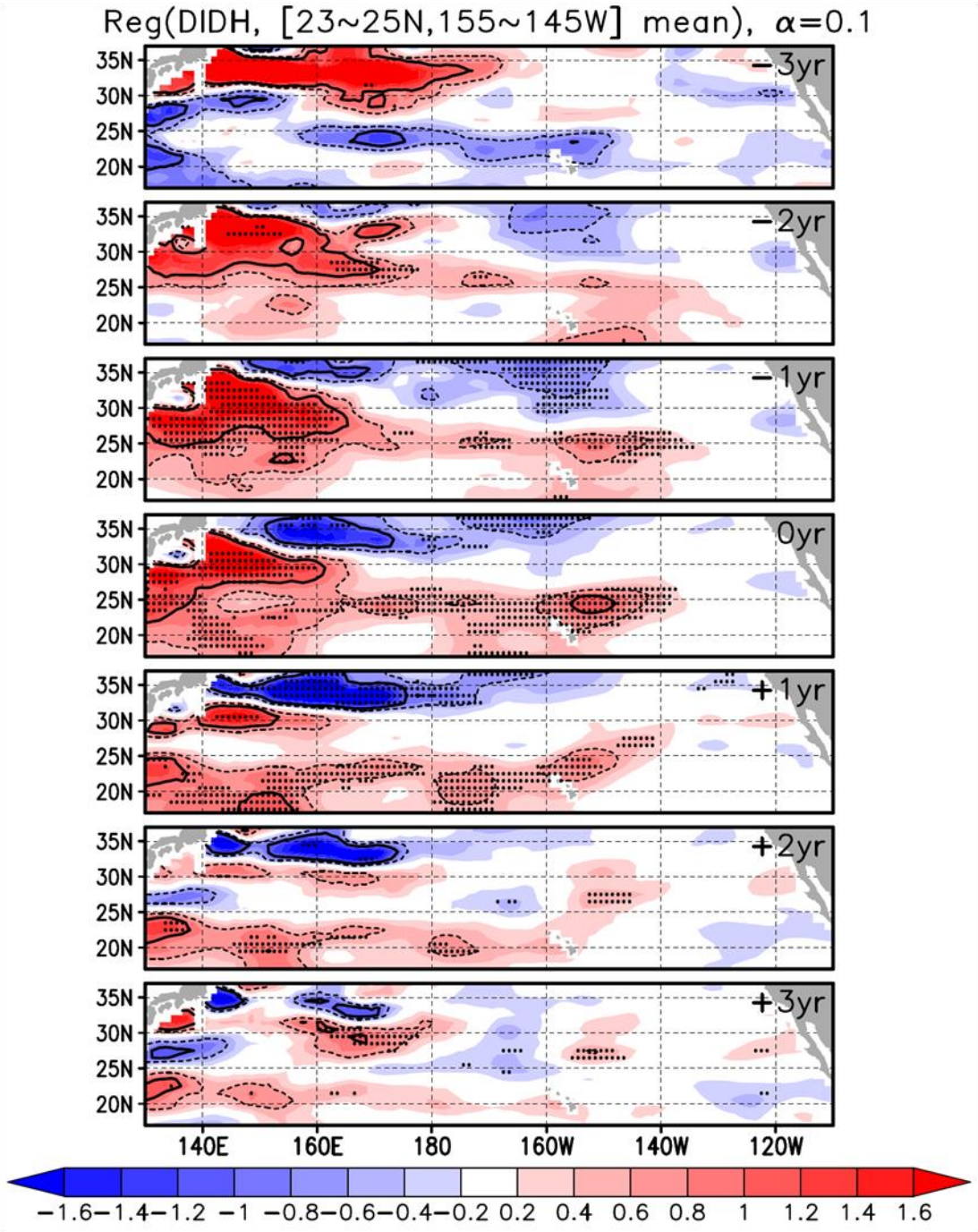


Fig.3-16. Lagged regression (shades) maps of interannually varying depth-integrated dynamic height onto the same field averaged at (23°~25°N, 155°~145°W) with lags of -3 to +3 years from the top to bottom. Thick and broken contours show the lagged regression = ±1 and 0.6. Grid points of significant regression at the 90% confidence limit are denoted by black dots.

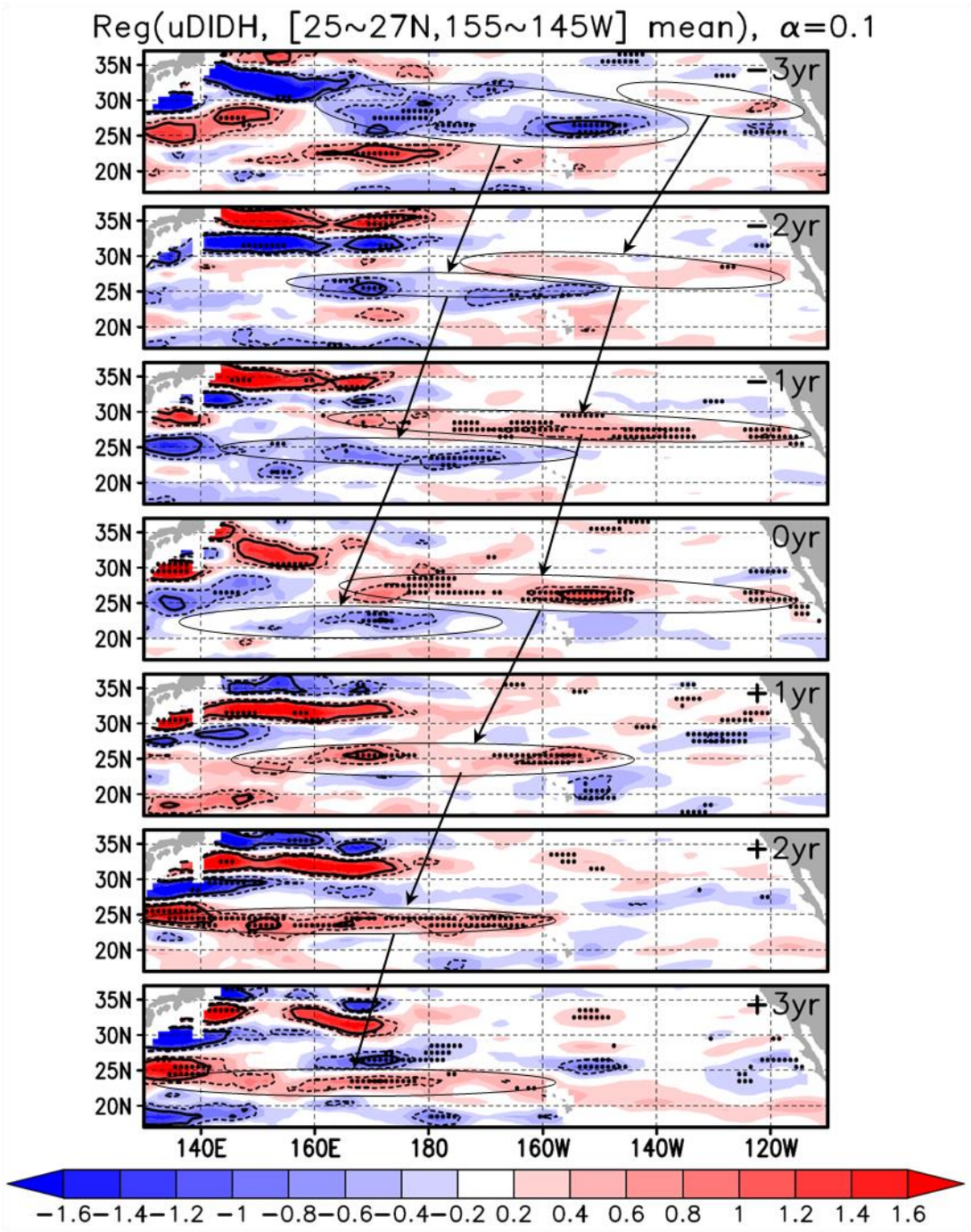


Fig.3-17. Same as in Fig. 3-18, but for depth-integrated zonal velocity. Arrows show the movement of zonal velocity signal traced by zonal structures from individual lagged regression maps.

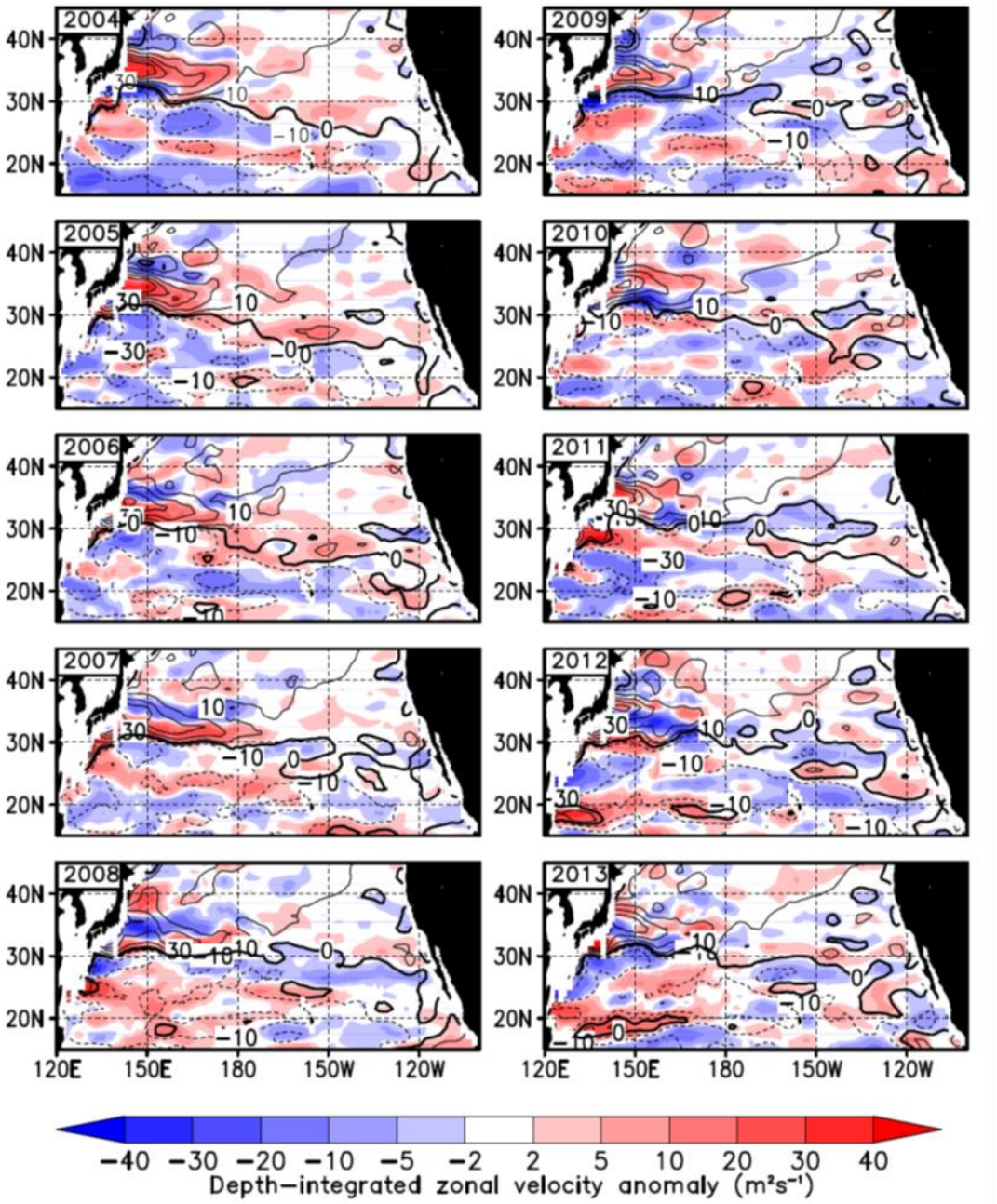


Fig.3-18. Yearly-mean distributions of the depth-integrated zonal velocity (contours) and its anomaly (color) from the mean from 2004 to 2013.

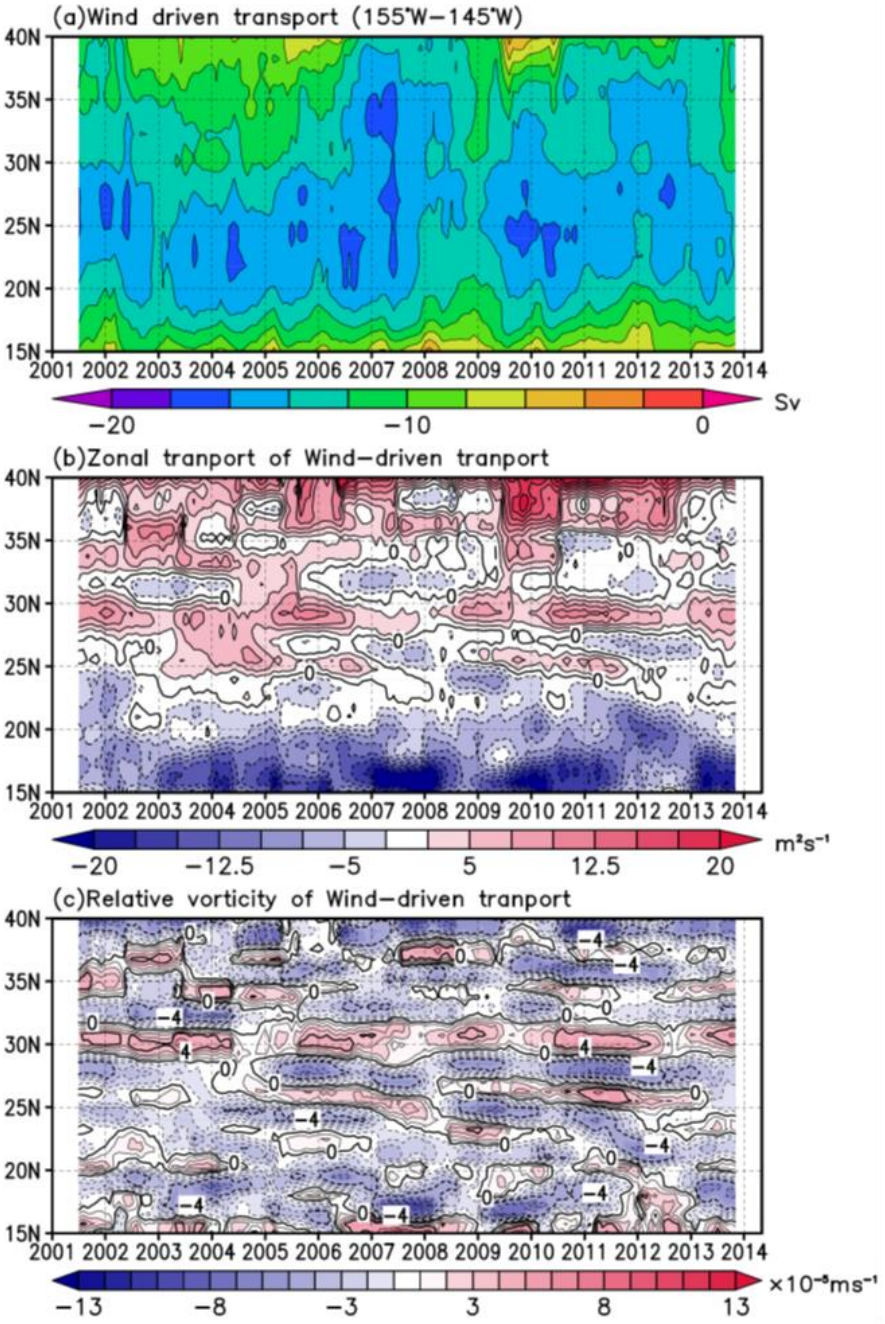


Fig.3-19. Time series of (a) wind-driven transport, (b) zonal wind-driven transport and (c) relative vorticity of wind driven transport, zonally averaged between 155°W and 145°W.

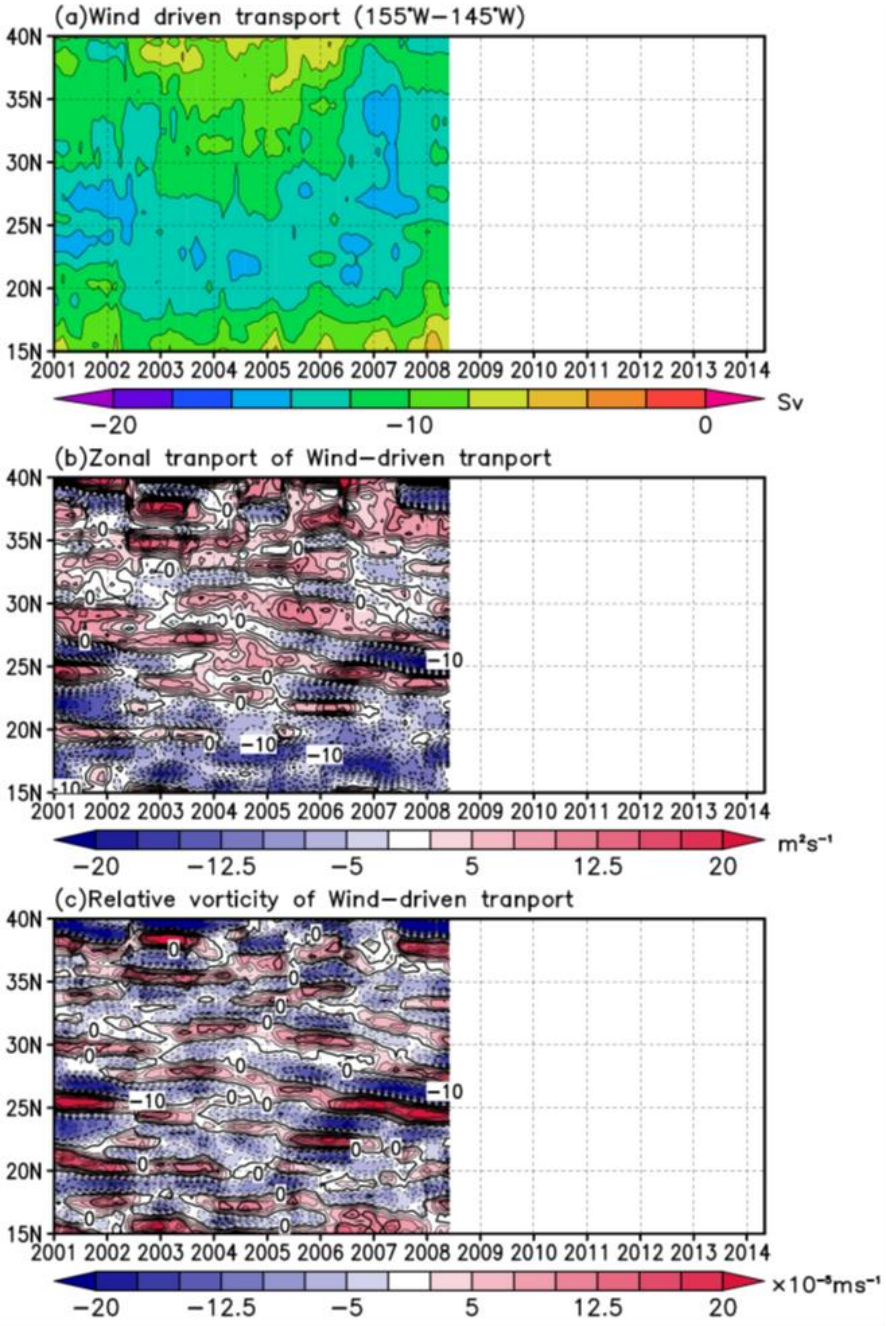


Fig.3-20 Same as in Fig. 3-19, but for J-OFURO high resolution version.

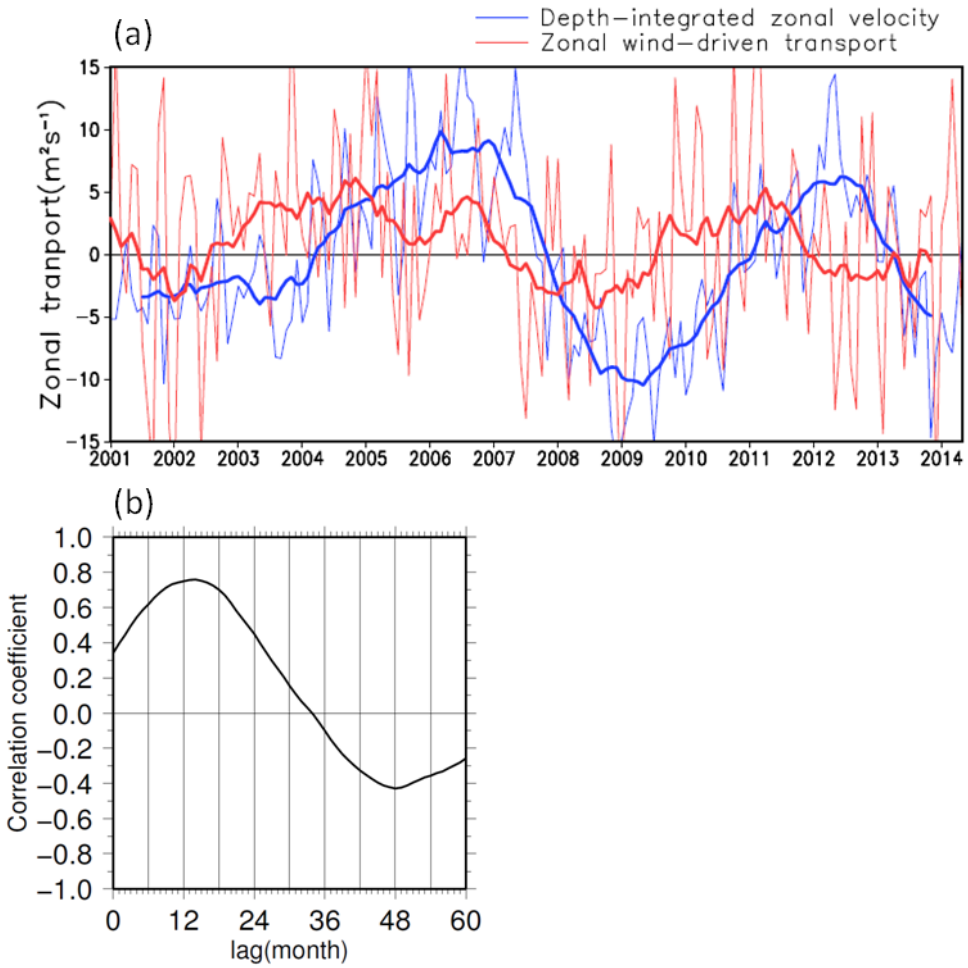


Fig.3-21. (a) Time series of the depth-integrated zonal velocity from MOAA GPV (blue lines) and zonal wind-driven transports from ERA-Interim (red lines) averaged in the region of 25~27°N and 155°W~145°W . Thick lines denote the 13month running mean. (b) Lagged correlation between the depth-integrated zonal velocity and zonal wind-driven transports. Here, lagged correlation is estimated from the time series of 13 month running mean values (thick red and blue lines). A positive lag denotes the lead by zonal wind-driven transports.

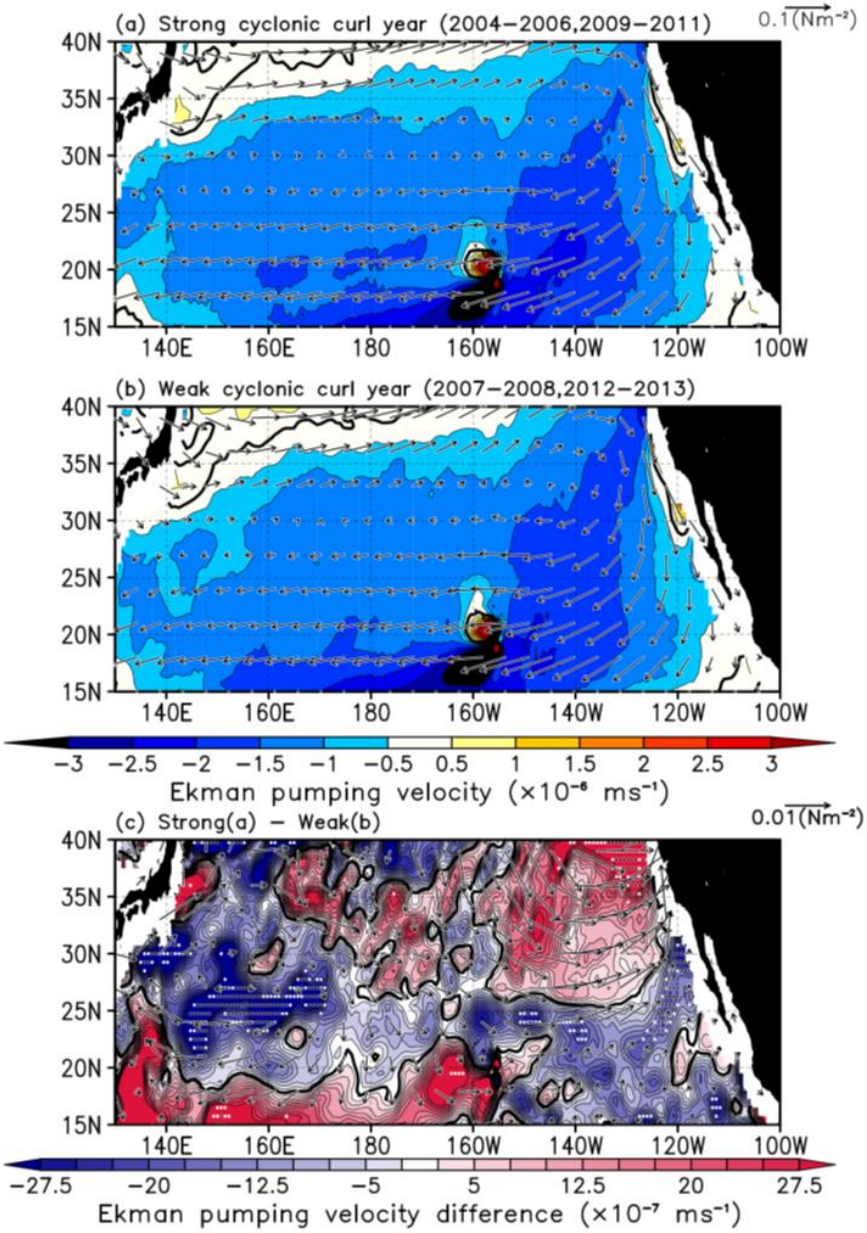


Fig.3-22 Composite maps of the Ekman pumping velocity (color) and wind stress vector in (a) the eastward flow years (2004~2006 and 2009~2011) and (b) the other years. (c) Difference between the maps in (a) and (b). In (c), white and black circles show significant difference at 85 and 90% confidence limit, respectively.

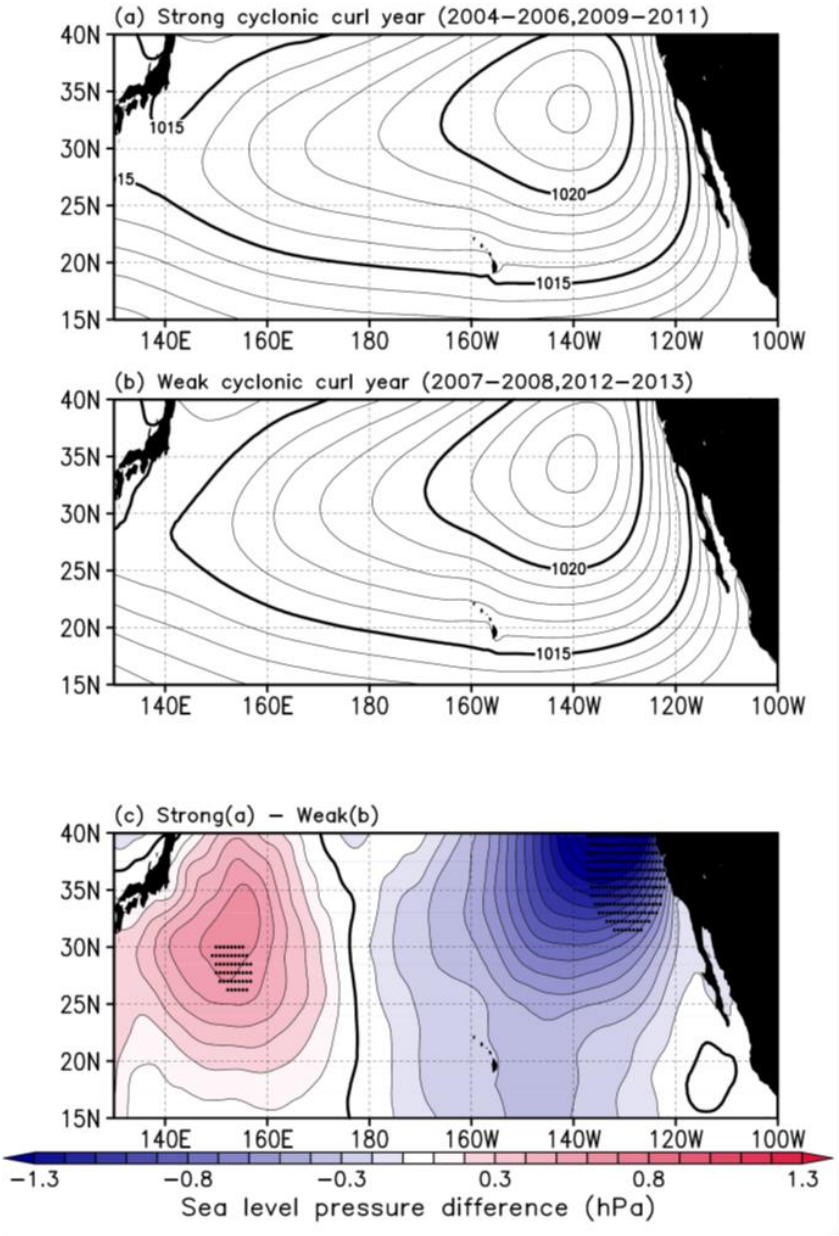


Fig.3-23 Same as in Fig. 3-22, but for the sea level pressure. In (c), black circles show significant difference at 90% confidence limit.

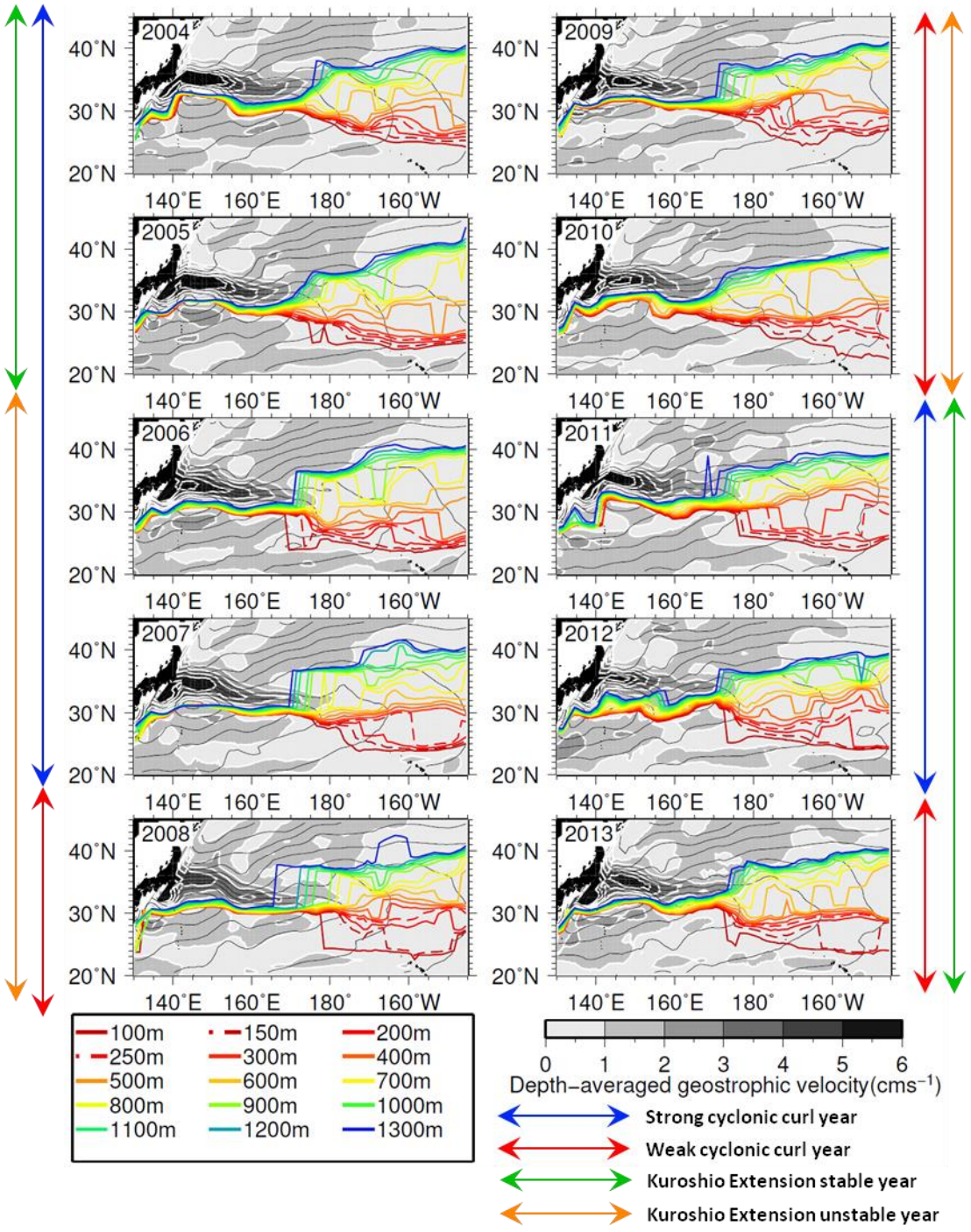


Fig.3-24. Yearly-mean distributions of the depth-averaged geostrophic velocity (shading) and depth-integrated dynamic height (contours) together with the gyre axis at different depths (color lines) from 2004 to 2013. Blue (red) and green (orange) arrows denote the strong (weak) cyclonic rotation years and Kuroshio stable (unstable) years, respectively.

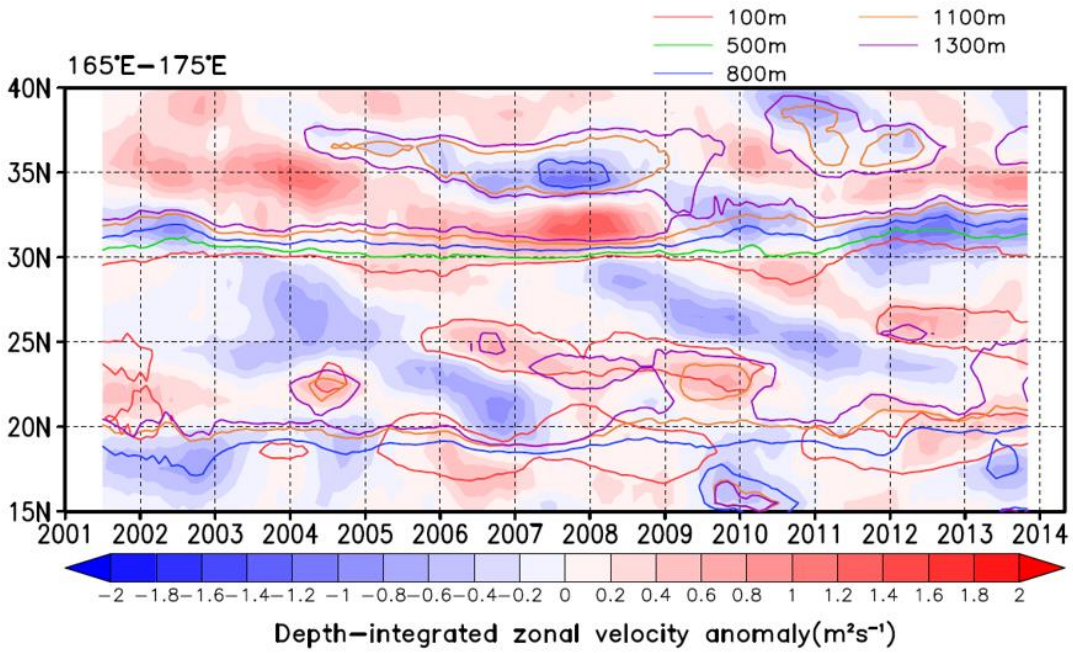


Fig.3-25. Time-latitude section of the depth-integrated zonal velocity zonally averaged between 165°E and 175°E. The color contours denote the zero lines of the zonal velocity at different depths.

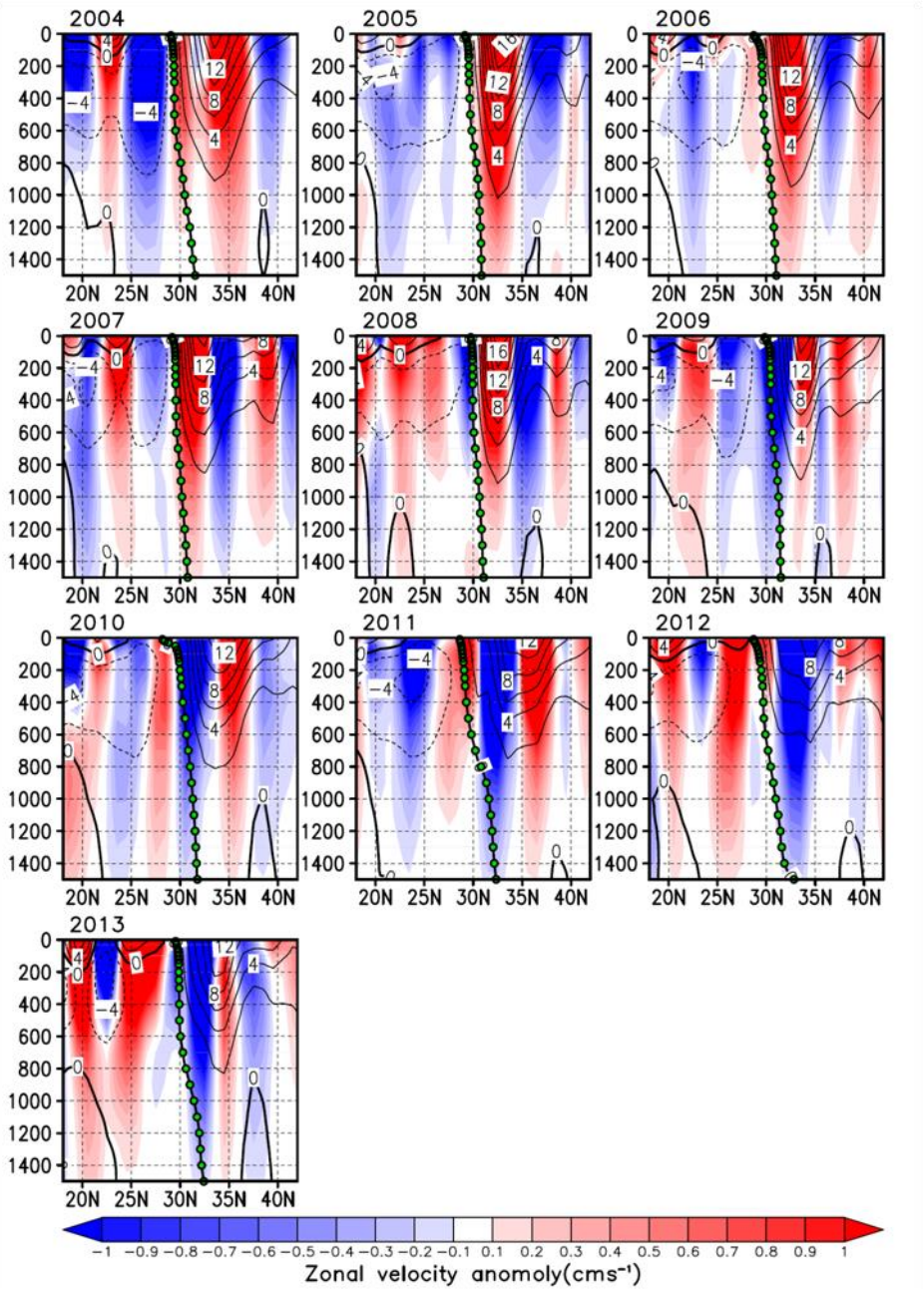


Fig.3-26. Yearly-mean latitude-depth section of zonal geostrophic velocity (contours) and its anomaly along 160°E. Green circles denote the gyre axis defined from the mean zonal velocity.

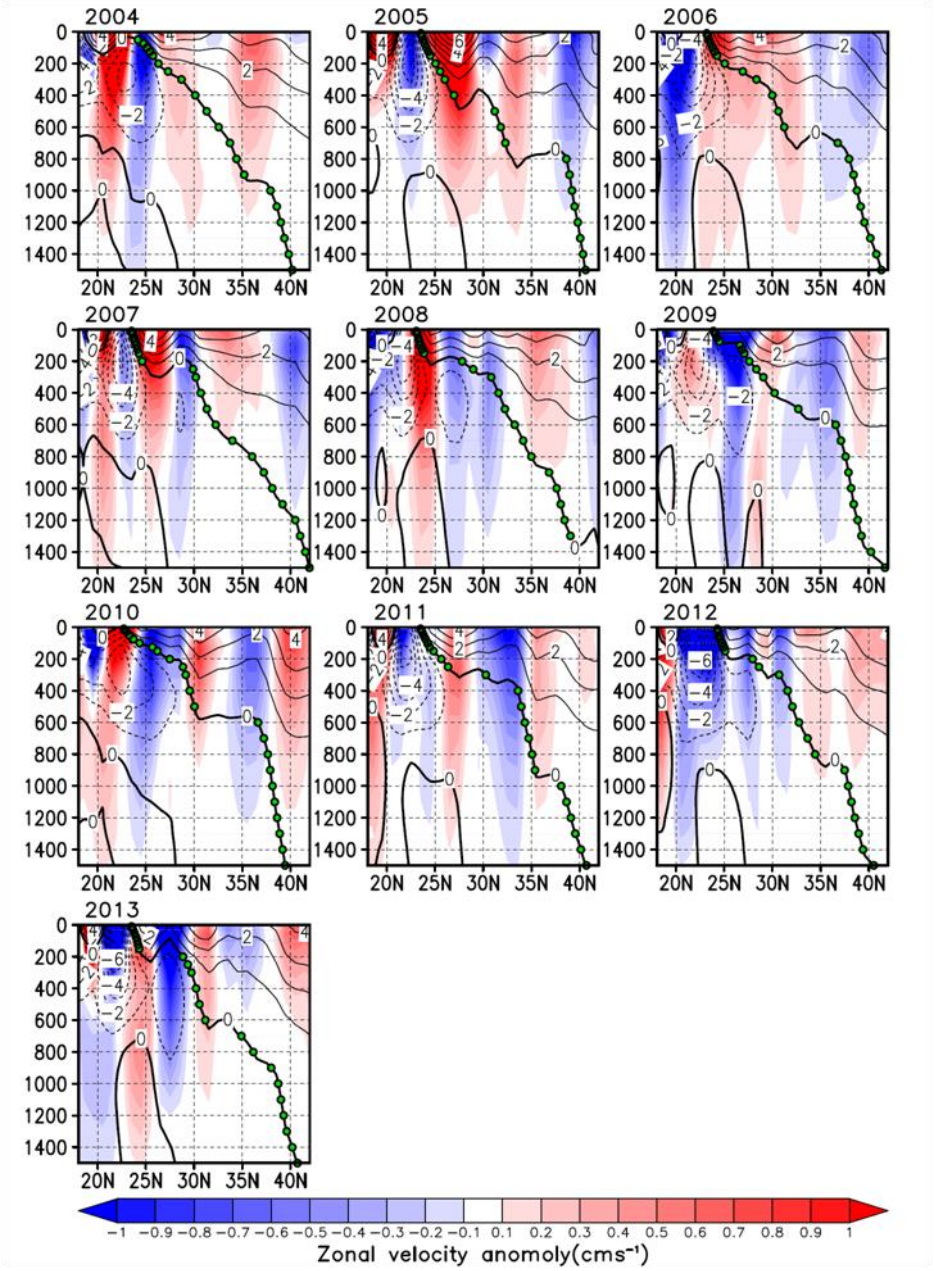


Fig.3-27. Same as in Fig. 3-26, but along 160°W

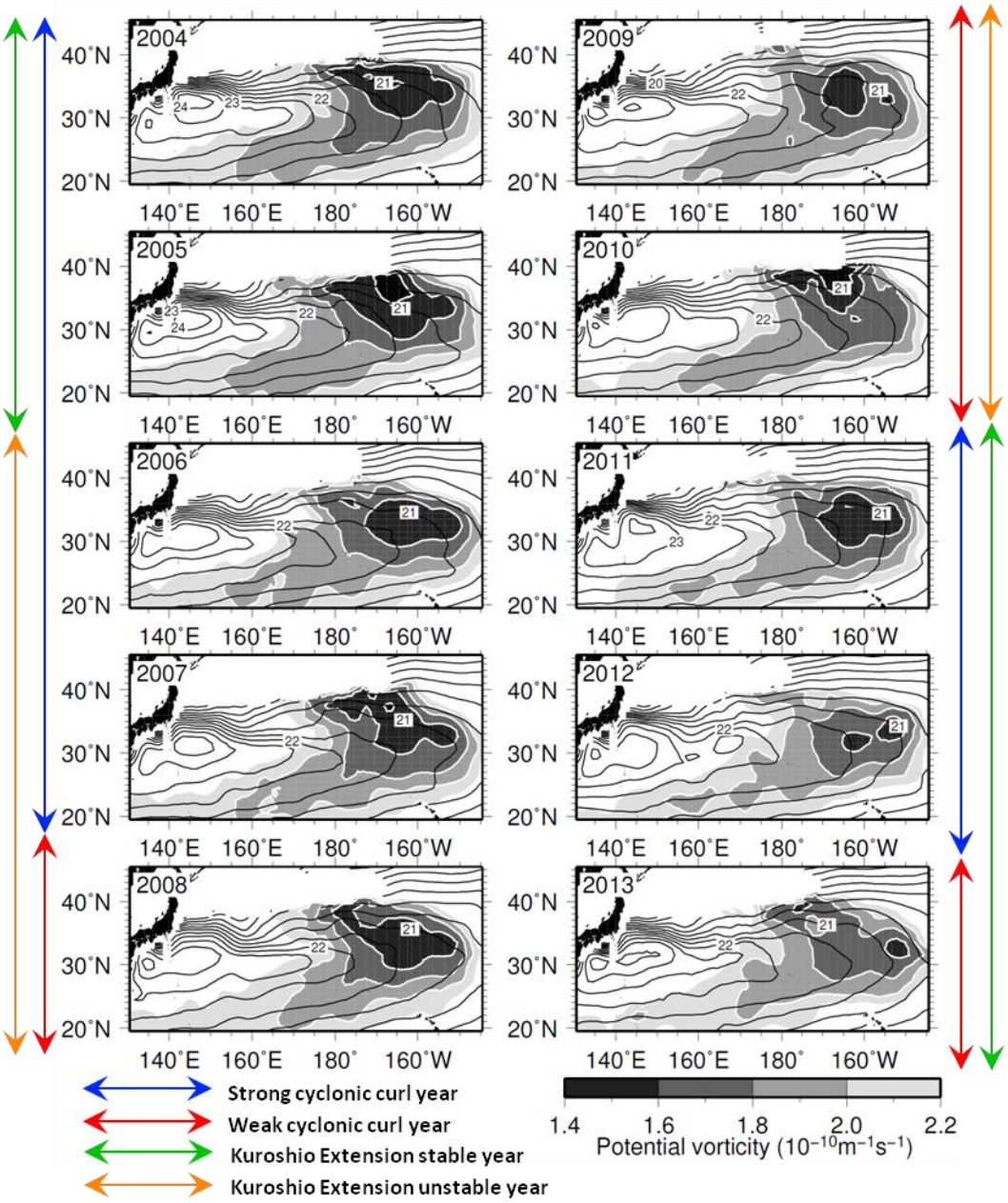


Fig.3-28. Same as in Fig. 24, but for PV (shading) and acceleration potential (contour) on 1026.2kg $m^{-3}$.

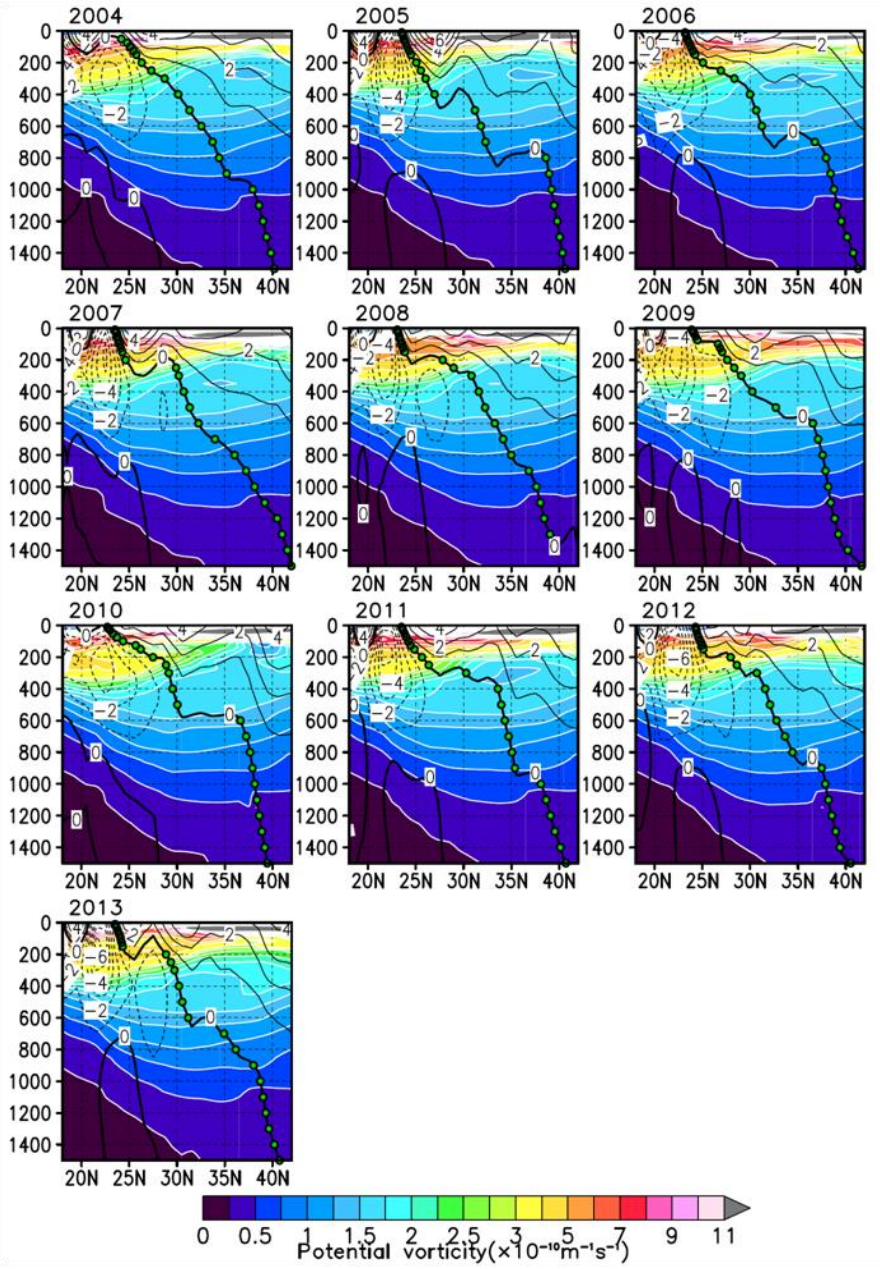


Fig.3-29. Same as in Fig. 3-27, but for PV (color).

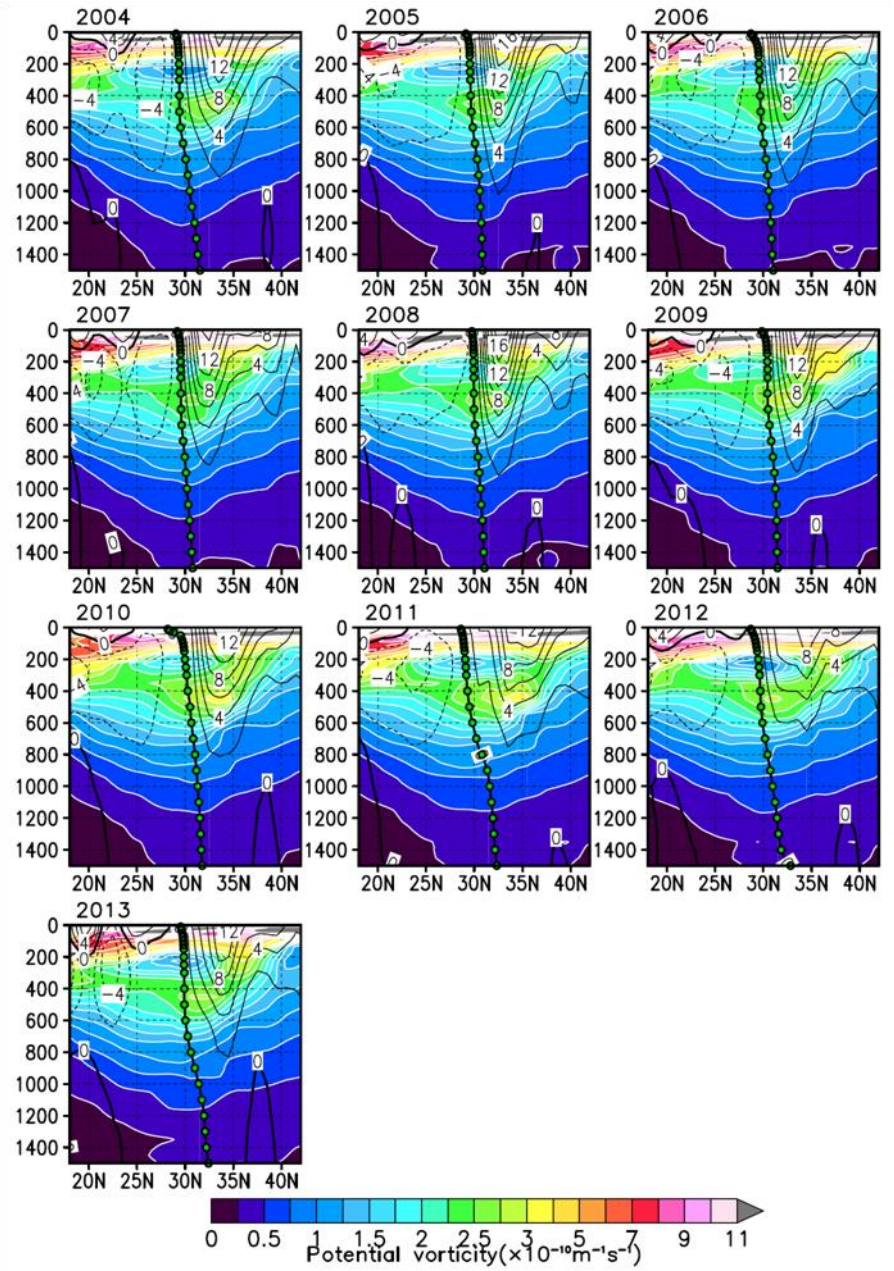


Fig.3-30. Same as in Fig. 3-29, but along 160°E.

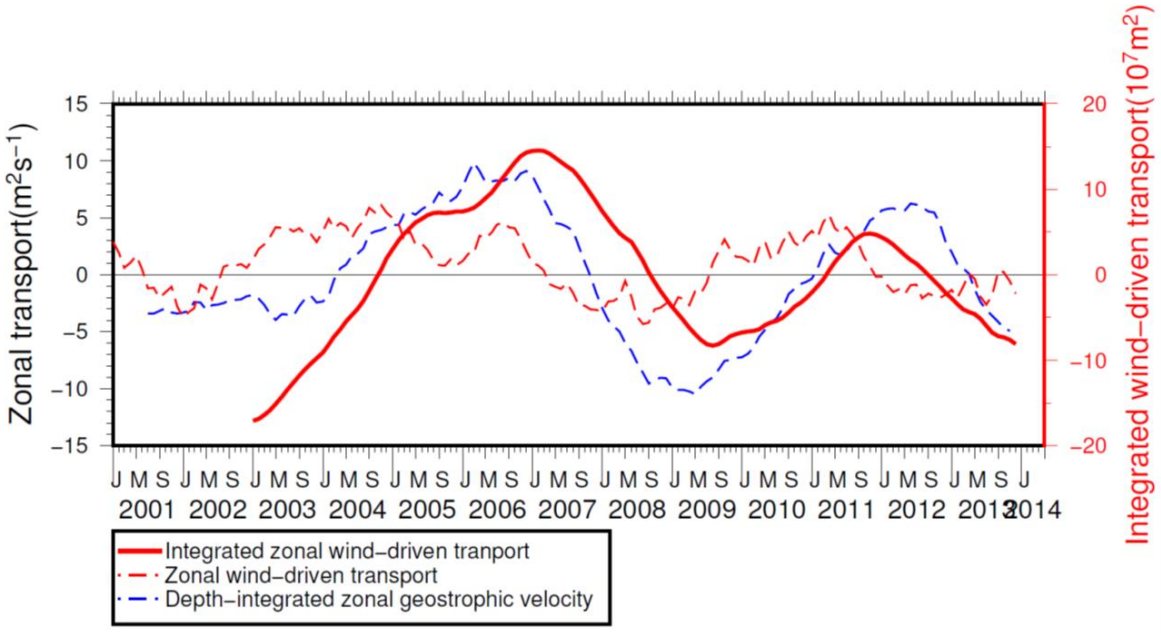


Fig.3-31. Same as Fig. 3-21, but for the time-integrated wind-drive zonal transport superimposed (thick red line). The linear trend was removed by a least-square fitting. Dashed red and blue lines are the same as the thick lines in Fig. 3-21. The correlation coefficient between the depth-integrated zonal geostrophic velocity (dashed blue line) and the integrated zonal wind-driven transport (thick red line) is 0.66 which is significant at the 90% confidence level ($r$=0.51).

# Chapter 4
# General conclusions

In this study, I have investigated the mean structures and temporal variations of the North Pacific subtropical gyre with a particular focus on the depth-integrated geostrophic circulation and the vertical structure of the geostrophic circulation by using Argo gridded datasets and several atmospheric reanalysis and satellite datasets.

In Chapter 2, the mean structures of the subtropical gyre were investigated by defining the gyre axis based on the horizontal pattern of the geostrophic circulation. The gyre axes of the depth-integrated geostrophic circulation and the vertical structure of the gyre axes both show the differences between the regions east and west of about 180° (Fig. 4-1). In the west, the gyre axis is strongly affected by the Kuroshio Extension jet and the Kuroshio recirculation, showing the discrepancy with the Sverdrup theory and the ventilated thermocline theory.

The mean depth-integrated geostrophic circulation shows the two gyre axes about 25°N and 30°N in the eastern basin, which correspond well to those expected from the wind-driven circulation calculated by the wind stress based on the Sverdrup theory. The two gyre axes are associated with a local cyclonic wind stress curl anomaly between 145°W and 125°W, probably due to southeasterly wind anomalies there. The Sverdrup theory expects that the two gyre axes would extend further to the west across the subtropical gyre, but the actual geostrophic circulation shows only one gyre axis around 30°N to the west, suggesting some discrepancy with the Sverdrup theory in the west. The difference in the west was considered to be associated with the strong barotropic motions of the Kuroshio recirculation where the nonlinear dynamics are predominant.

The vertical structures of the gyre axis are also quite different between the east and the west of about 180°. The gyre axis indicates a prominent northward shift with depth in the east, where a broad weak zonal flow is dominant and the thickness of density layers decreases to the south, favorable for the $\beta$ spiral. In addition, the PV on the CMW layers near the gyre axis increase to the downstream probably due to dissipation by mixing effects. On the other hand, in the west, the gyre axis lies just along the southern flank of the strong barotropic-like Kuroshio Extension jet with no remarkable northward shift. The high PV water in the pycnocline of the Kuroshio Extension is suggested to disrupt the meridional continuity of PV around the jet and thus prevents the gyre axis from shifting to the north.

The northward shift of the gyre axis with depth in the eastern part of the subtropical gyre occurs non-uniformly in the vertical, which is relatively small near the surface, in the CMW layer and at depths deeper than 900m, and in contrast, it is large in the upper and lower thermocline layers. I found that the small northward shift of the gyre axis in the CMW layer is due to the horizontal uniformity of the CMW from the analysis based on the vertical shears of the horizontal velocity. The results indicate the dynamical effect of the CMW on the large-scale circulations of the subtropical gyre.

In Chapter 3, the temporal variations of the depth-integrated circulation were first investigated with a focus on the eastern subtropical gyre. I found that there are two local rotations: one is the cyclonic rotation between the mean two gyre axes and the other is the anticyclonic rotation to the south. The latter seems to correspond to the Eastern Gyral that was first identified from historical data analysis by Sverdrup et al. (1942). I examined the variations of the two local rotations and their relationship with atmospheric forcings. Then, I investigated the year-to-year variations of the vertical structures of the gyre axis and their relationship with the structures of velocity and PV.

The local cyclonic and anticyclonic rotations both exhibit interannual variations with a period of about 5 years with no significant seasonal cycles. The composite analysis revealed that the two rotations are both caused by vertically coherent changes in the eastward flow around 26°N near the boundary of the two rotations. The changes in the eastward flow are mainly relating to those in the depth-integrated dynamic height to the south of the eastward flow through a geostrophic balance.

The depth-integrated zonal velocity of the eastward flow was compared with the zonal wind-driven transport calculated from surface wind data. Although there is a time lag of about 1 year, they are well correlated with each other. The time lag rough corresponds to the phase difference of $\pi/2$ of about 5-year variations, strongly suggesting that the time rate of the change in the eastward flow responds to the wind stress curl forcing, which was discussed in the context of the time-dependent Sverdrup theory. Indeed, the time-integrated wind stress curl is overall in agreement with the observed eastward flow without notable phase differences. The composite map of the Ekman pumping velocity indicates that the strong eastward flow is associated with local intensification of the Ekman pumping due to the changes in wind-stress curl to the south of 26°N. These results indicate that the interannual variations of the two local rotations are induced by the local wind changes rather than by large-scale atmospheric forcing. I have discussed the possible mechanism for the changes in the local Ekman pumping.

The lagged regression analysis shows that the signals of the depth-integrated dynamic height and the zonal velocity anomaly propagate southwestward from the northeastern subtropical gyre (Fig. 4-2). The eastward flow anomaly is enhanced around 26°N on the year-to-year time scales.

The year-to-year variations of the northward shift of the gyre axis with depth were seen both in the eastern and western regions of 170°E. In the downstream region of the

Kuroshio Extension, the northward shift of the gyre axis was large after 2009, which was related to the relatively weak Kuroshio Extension there. On the other hand, in the eastern part of the subtropical gyre, I found that the variations of the position of the gyre axis were large at the subsurface layer of 200~800 m depths, small at depths of 0~200 m and deeper than 1000 m. The position of the gyre axis in the upper layer was located in the southern edge of the eastern STCC. I suggest that the position of the gyre axis in the upper layer in the eastern subtropical gyre is associated with the vertical extent and meridional position of the eastern STCC.

I investigated the relationship between the variations of the gyre axis and PV structures in the eastern and western subtropical gyres. In the eastern region, when the CMW is located near the position of the mean gyre axis, the northward shift of the gyre axis with depth tends to be small in the CMW layer, but such relationship is not always seen. The results suggest that the vertical structures of the gyre axis are affected not only by the intensity and distribution of the CMW but also by other ocean structures. On the other hand, in the west at 160°E, I found that the northward shift of the gyre shift is related to the upper velocity of the Kuroshio Extension rather than PV structures. The more quantitative analysis for the temporal variations of the vertical structure of the subtropical gyre will be necessary for a further better understanding.

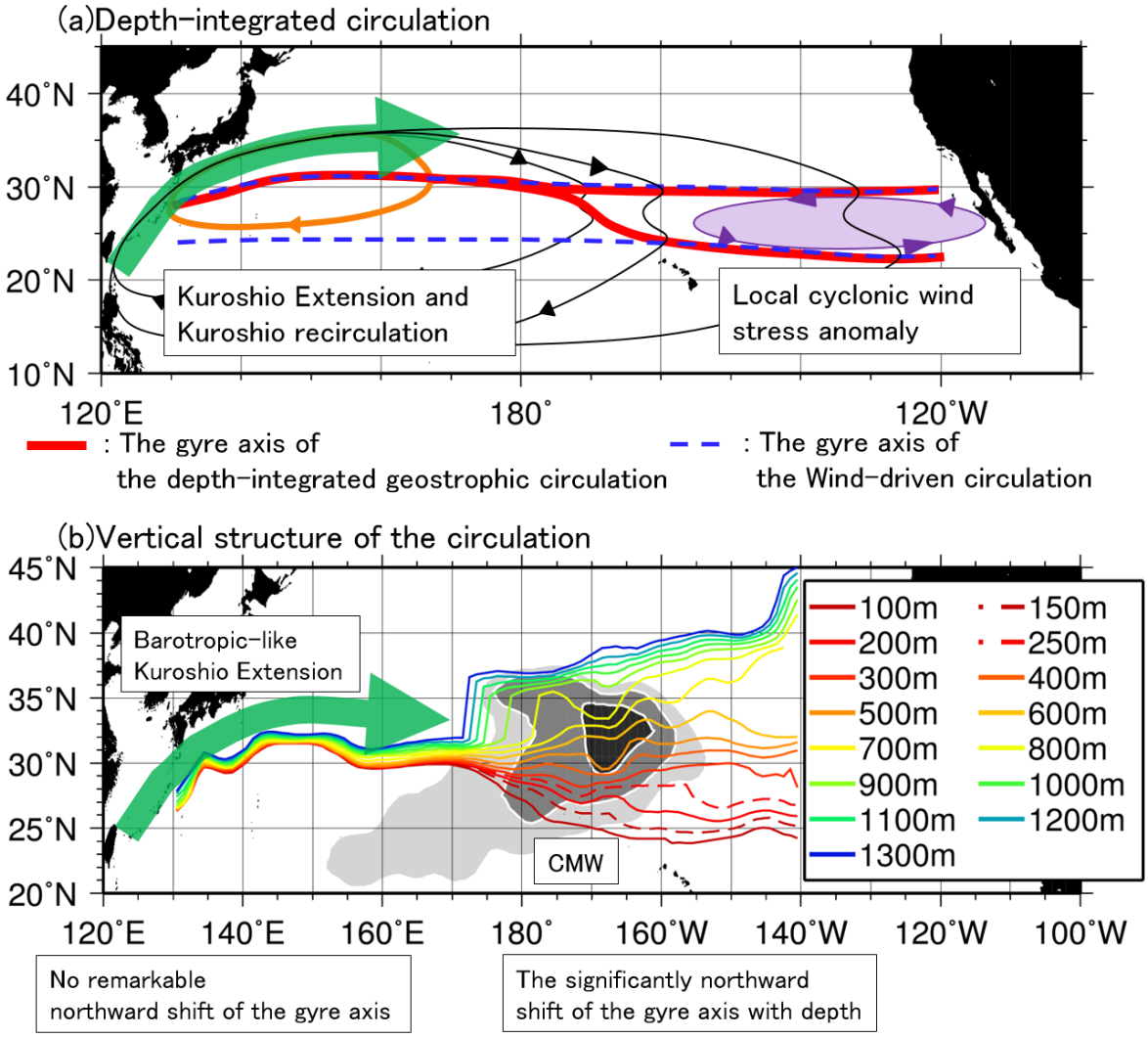


Fig.4-1. Schematic summary for (a) mean depth-integrated geostrophic circulation and (b) mean vertical structures of the circulation in Chapter 2. Green arrows show the Kuroshio Extension. In (a), black contours with arrows are the mean streamlines of the depth-integrated circulation. Thick red lines and dashed blue lines are the gyre axis of the depth-integrated circulation and the wind-drive circulation, respectively. Orange and purple lines with arrows denote the Kuroshio recirculation and the local cyclonic wind stress curl anomaly, respectively. In (b), the gyre axes at different depths are shown by color lines. Shade indicates low PV on the isopycnal surface of 1026.0 kg/m$^3$.

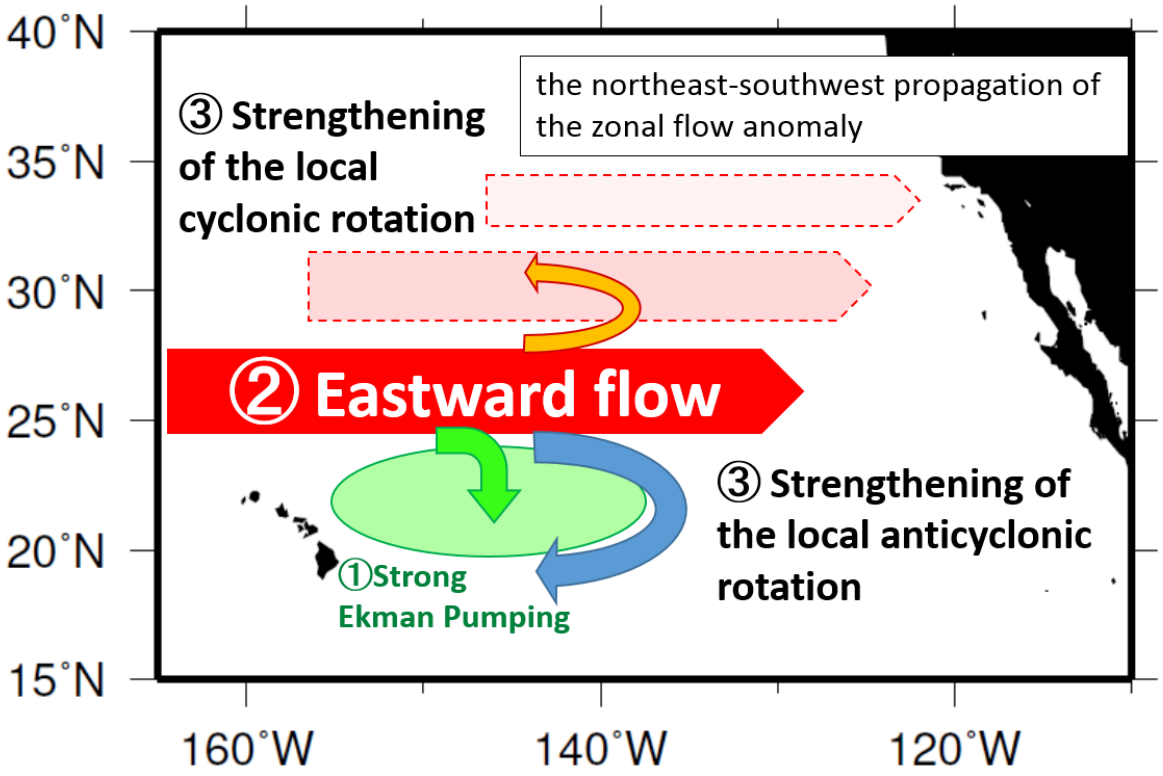


Fig.4-2. Schematic summary for the mechanism of the variations of local cyclonic and anticyclonic rotations in the eastern subtropical gyre. The Ekman pumping at the south of 26°N is first enhanced, accelerating the eastward flow along 26°N, and thereby both the local cyclonic and anticyclonic rotations are strengthened. In addition, the signal of the zonal velocity propagates southwestward from the northeast subtropical gyre is enhanced at 26°N.

# Acknowledgements

I am most grateful to the supervisor Ass. Prof. Fumiaki Kobashi for his guidance and continuous encouragement. This study could not have been done without his dedicated support. I would like to thank Prof. Naoto Iwasaka and Ass. Prof. Koji Shimada for helpful comments and discussions. I am also grateful to Prof. Atsushi Kubokawa and Prof. Youichi Tanimoto for many helpful comments and suggestions.

I thank Prof. Kunio Kutsuwada and Mr. Suguru Kameda for providing QuikSCAT wind stress. I acknowledge Dr. Shusaku Sugimoto for help in processing the data.

I would like to thank Ass. Prof. Eitaro Oka, Mr. Shota Katsura and the other members of the Physical Oceanography and the Climate Dynamics Group, The University of Tokyo for valuable comments and encouragement.

I'm grateful to students in environmental science laboratory: Yosuke Shimura, Keita Suzuki, Tsubasa Okada, Takahiro Suzuki, Koichi Tada, Yukino Onigata and the other undergraduate students. I was able to spend a good time thanks to the life with them.

MOAA GPV was obtained from the Japan Agency for Marine-Earth Science and Technology (JAMSTEC). The JRA25 wind stress data was obtained from the Japan Meteorological Agency website, the J-OFURO from the J-OFURO website of Tokai University, the NCEP/NCAR and NCEP/DOE data from the NOAA website, the MERRA from the NASA website, and the ERA-Interim from ECMWF website. I would like to acknowledge these data providers.

Finally, I great thank my parents Noboru and Mariko, grandmother Yori and brother Toshifumi for their continuous and warm support.

# References


Aoki, K., and K. Kutsuwada, 2008: Verification of the Wind-Driven Transport in the North Pacific Subtropical Gyre Using Gridded Wind-Stress Products. *J. Oceanogr.*, **64**, 49-60.

Auad, G., D. Roemmich, J. Gilson, 2011: The California Current System in relation to the Northeast Pacific Ocean circulation. *Prog. Oceanogr*., **91**. 576-592. doi:10.1016/j.pocean.2011.09.004.

Boyer, T. P., J. I. Antonov, H. E. Garcia, D. R. Johnson, R. A. Locarnini, V. Mishonov, M. T. Pitcher, O. K. Baranova and I. V. Smolyar, 2006: World Ocean Database 2005. In NOAA Atlas NESDIS 60, ed. by S. Levitus, U.S. Government Printing Office, Washington, D.C., 190 pp., DVDs.

Brunke, M. A., Z. Wang, X. Zeng, M. Bosilovich, and C.-L. Shie, 2011: An assessment of the uncertainties in ocean surface turbulent fluxes in 11 reanalysis, satellite-derived, and combined global datasets. *J. Climate*, **24**, 5469–5493.

Chelton, D. B., and A. M. Mestas-Nuñez, 1996: The large-scale, wind-driven response of the North Pacific. Int. *WOCE Newsletter*, **25**, 3-6.

Chelton, D. B., M. G. Schlax, and R. M. Samelson 2011: Global observations of nonlinear mesoscale eddies. *Prog. Oceanogr*., **91**, 167-216, doi:10.1016/j.pocean.2011.01.002.

Chen, S., B. Qiu, and P. Hacker, 2007: Profiling float measurements of the recirculation gyre south of the Kuroshio Extension in May to November 2004. *J. Geophys. Res.*, **112**, C05023, doi:10.1029/2006JC004005.

Cummins, P. F., and H. J. Freeland, 2007: Variability of the North Pacific Current and its bifurcation. *Prog. Oceanogr*., **75**, 253–265, doi:10.1016/j.pocean.2007.08.006.

Dee, D. P., S. M. Uppala, A. J. Simmons, P. Berrisford, P. Poli, S. Kobayashi, U. Andrae, M. A. Balmaseda, G. Balsamo, P. Bauer, P. Bechtold, A. C. M. Beljaars, L. van de Berg, J. Bidlot, N. Bormann, C. Delsol, R. Dragani, M. Fuentes, A. J. Geer, L. Haimberger, S. B. Healy, H. Hersbach, E. V. Holm, L. Isaksen, P. Kallberg, M. Kohler, M. Matricardi, A. P. McNally, B. M. Monge-Sanz, J.-J. Morcrette, B.-K. Park, C. Peubey, P. de Rosnay, C. Tavolato, J.-N. Thepaut and F. Vitart, 2011: The ERA-Interim reanalysis: Configuration and performance of the data assimilation system. *Quart. J. Roy. Meteor. Soc*., **137**, 553–597, doi:10.1002/qj.828.

Douglass, E., D. Roemmich, and D. Stammer, 2006: Interannual variability in northeast Pacific circulation. *J. Geophys. Res.*, **111**, C04001, doi:10.1029/2005JC003015.

Ekman, V.W., 1905: On the influence of the earth's rotation on ocean currents. *Arkiv f. Matem., Astr. O. Fysik* (Stockholm) Bd. 2, No. 11, 53 pp.

Flament, P., S. Kennan, R. Lumpkin, M. Sawyer, and E. Stroup, 1998: The ocean. Atlas of Hawaii, S. P. Juvik and J. O. Juvik, Eds., University of Hawaii Press, 82–86.

Giglio, D., D. Roemmich, S. and T. Gille, 2012: Wind-Driven Variability of the Subtropical North Pacific Ocean. *J. Phys. Oceanogr*., **42**, 2089-2100.

Hanawa, K., and S. Sugimoto, 2004: 'Reemergence' areas of winter sea surface temperature anomalies in the world's oceans. *Geophys. Res. Lett.*, **31**, L10303. doi:10.1029/2004GL019904.

Hautala, S. L., and D. Roemmich, 1998: Subtropical mode water in the Northeast Pacific basin. *J. Geophys. Res*., **103**, 13055–13066.

Hautala, S. L., D. Roemmich, and W. J. Schmitz, Jr. 1994: Is the North Pacific in Sverdrup balance along 24N? *J. Geophys. Res.*, **99**, 16041-16052.

Hellerman, S., and M. Rosenstein, 1983: Normal monthly wind stress over the World Ocean with error estimates. *J. Phys. Oceanogr.*, **13**, 1093-1104.

Hosoda, S., S.-P. Xie, K. Takeuchi, and M. Nonaka 2004: Interdecadal temperature variations in the North Pacific central mode water simulated by an OGCM. *J. Oceanogr.*, **60**, 865-877.

Hosoda, S., T. Ohira, T. Nakamura, 2008: A monthly mean dataset of global oceanic temperature and salinity derived from Argo float observations. *JAMSTEC Rep. Res. Dev.*, **8**, 47–59.

Huang, R. X., and B. Qiu, 1994: Three-dimensional structure of the wind driven circulation in the subtropical North Pacific. *J. Phys. Oceanogr.*, **24**, 1608-1622.

Huang, R. X., and S. Russell, 1994: Ventilation of the subtropical North Pacific. *J. Phys. Oceanogr.*, **24**, 2589-2605.

Kalnay, E., M. Kanamitsu, R. Kistler, W. Collins, D. Deaven, L. Gandin, M. Iredell, S. Saha, G. White, J. Woollen, Y. Zhu, M. Chelliah, W. Ebisuzaki, W. Higgins, J. Janowiak, K. C. Mo, C. Ropelewski, A. Leetmaa, A. Reynolds, and R. Jenne, 1996: The NCEP/NCAR 40-year reanalysis project. *Bull. Amer. Meteor. Soc.*, **77**, 437-471.

Kanamitsu, M., W. Ebisuzaki, J. Woollen, S.-K. Yang, J. J. Hnilo, M. Fiorino, and G. L. Potter 2002: NCEP–DOE AMIP-II Reanalysis (R-2). *Bull. Amer. Meteor. Soc.*, **83**, 1631-1643.

Kessler, W. S., and L. Gourdeau, 2006: Wind-driven zonal jets in the South Pacific Ocean, *Geophys. Res. Lett.*, **33**, L03608, doi:10.1029/2005GL025084.

Kobashi, F., and A. Kubokawa, 2012: Review on North Pacific Subtropical Countercurrents and Subtropical Fronts: role of mode waters in ocean circulation and climate. *J. Oceanogr.*, **68**, doi:10.1007/ s10872-011-0083-7.

Kobashi, F., and S.-P. Xie, 2012: Interannual variability of the North Pacific Subtropical Countercurrent: role of local ocean-atmosphere interaction. *J. Oceanogr.*, 113-126,

doi:10.1007/s10872-011-0048-x.

Kobashi, F., H. Mitsudera, and S.-P. Xie, 2006: Three subtropical fronts in the North Pacific: observational evidence for mode water-induced subsurface frontogenesis. *J. Geophys. Res.*, **111**, C09033. doi:10.1029/2006JC003479.

Kobashi, F., S.-P. Xie, N. Iwasaka, and T. T. Sakamoto, 2008: Deep atmospheric response to the North Pacific oceanic subtropical front in spring. *J. Climate*, **21**, 5960-5975.

Kubokawa, A., 1999: Ventilated thermocline strongly affected by a deep mixed layer: a theory for subtropical countercurrent. *J. Phys. Oceanogr.*, 29, 1314-1333.

Kubokawa, A.,and T. Inui, 1999: Subtropical countercurrent in an idealized ocean GCM. *J. Phys. Oceanogr.*, **29**, 1303-1313.

Kubota, M., H. Yokota, and T. Okamoto, 1995: Mechanism of the seasonal transport variation through the Tokara Strait. *J. Oceanogr.*, **51**, 441-458.

Kubota, M., N. Iwasaka, S. Kizu, M. Konda, and K. Kutsuwada, 2002: Japanese ocean flux data sets with use of remote sensing observation (J-OFURO). *J. Oceanogr.*, **58**, 213-225.

Kwon, Y.-O., M. Alexander, N. Bond, C. Frankignoul, H. Nakamura, B. Qiu, and L. Thompson, 2010: Role of the Gulf Stream and Kuroshio–Oyashio systems in large-scale atmosphere–ocean interaction: A review. *J. Climate*, **23**, 3249–3281, doi:10.1175/2010JCLI3343.1.

Ladd, C., and L. Thompson, 2002: Decadal variability of North Pacific central mode water. *J. Phys. Oceanogr.*, **32**, 2870-2881.

Levitus, S., 1982: Climatological atlas of the World Ocean. NOAA Prof. Paper No. 13, U.S. Dept. of Commerce, Washington, D.C., 173 pp.

Luyten, J. R., J. Pedlosky, and H. Stommel, 1983: The ventilated thermocline. *J. Phys. Oceanogr.*, **13**, 292-309.

Marchesiello, P., J.C. McWilliams, A. Shchepetkin, 2003: Equilibrium structure and dynamics of the California Current System. *J. Phys. Oceanogr.*, **33**, 753–783.

Masuzawa, J., 1969: Subtropical mode water, *Deep Sea Res.*, **16**, 436–472.

Maximenko, N. A., O. V. Melnichenko, P. P. Niiler, and H. Sasaki, 2008: Stationary mesoscale jet-like features in the ocean. *Geophys. Res. Lett.*, **35**, L08603, doi:10.1029/2008GL033267.

Melnichenko, O. V., N. A. Maximenko, N. Schneider, and H. Sasaki, 2010: Quasi-stationary striations in basin-scale oceanic circulation: Vorticity balance from observations and eddy-resolving model. *Ocean Dyn.*, **60**, 653–666, doi:10.1007/s10236-009-0260-z.

Mitas, C. M., and A. Clement, 2005: Has the Hadley cell been strengthening in recent decades? *Geophys. Res. Lett.*, **32**, L03809.

Munk, W. H., 1950: On the wind-driven ocean circulation. *J. Meteor.*, **7**, 79-93.

Nakamura, H., 1996: A pycnostad on the bottom of the ventilated portion in the central subtropical North Pacific: its distribution and formation. *J. Oceanogr.*, **52**, 171-188.

Nakano, H., and N. Suginohara, 2002: A Series of Middepth Zonal Flows in the Pacific Driven by Winds. *J. Phys. Oceanogr.*, **32**, 161-176.

Nishikawa S., H. Tsujino, K. Sakamoto, and H. Nakano, 2010: Effects of mesoscale eddies on subduction and distribution of subtropical mode water in an eddy-resolving OGCM of the western North Pacific. *J. Phys. Oceanogr.*, **40**, 1748–1765.

Nonaka, M., S.-P. Xie, and H. Sasaki, 2012: Interannual variations in low potential vorticity water and the subtropical countercurrent in an eddy-resolving OGCM. *J. Oceanogr.*, doi10.1007/s10872-011-0042-3.

Oka, E., and T. Suga, 2005: Differential formation and circulation of North Pacific central mode water. *J. Phys. Oceanogr*, **35**, 1997-2011.

Onogi, K., J. Tsutsui, H. Koide, M. Sakamoto, S. Kobayashi, H. Hatsushika, T. Matsumoto, N. Yamazaki, H. Kamahori, K. Takahashi, S. Kadokura, K. Wada, K. Kato, R. Oyama, T. Ose, N. Mannoji, and R. Taira, 2007: The JRA-25 reanalysis. *J. Meteor. Soc. Jpn.*, **85**, 369-432.

Pedlosky, J., 1996: Ocean Circulation Theory. Springer-Verlag, Heidelberg, 453 pp.

Press, W. H., A. Teukolsky, W. T. Vettering, and B. P. Flannery, 1992: Numerical Recipes. Cambridge University Press, 963pp.

Qiu, B., 2002a: The Kuroshio Extension System: Its Large-Scale Variability and Role in the Midlatitude Ocean-Atmosphere Interaction. *J. Oceanogr.*, **58**, 57-75.

Qiu, B., 2002b: Large-Scale Variability in the Midlatitude Subtropical and Subpolar North Pacific Ocean: Observations and Causes. *J. Phys. Oceanogr.*, **32**, 353-375

Qiu, B., and S. Chen, 2010: Interannual-to-decadal variability in the bifurcation of the North Equatorial Current off the Philippines. *J. Phys. Oceanogr.*, **40**, 2525–2538.

Qiu, B., and S. Chen, 2012: Multi-decadal sea level and gyre circulation variability in the north western tropical Pacific Ocean. *J. Phys. Oceanogr.*, **42**, 193-206.

Qiu, B., D. A. Koh, C. Lumpkin, and P. Flament, 1997: Existence and formation mechanism of the North Hawaiian Ridge current. *J. Phys. Oceanogr.*, **27**, 431-444.

Qiu, B., P. Hacker, S. Chen, K. A. Donohue, D. R. Watts, H. Mitsudera, N. G. Hogg, and S. R. Jayne, 2006: Observations of the subtropical mode water evolution from the Kuroshio Extension System Study. *J. Phys. Oceanogr.*, **36**, 457–473.

Qiu, B., D. L. Rudnick, S. Chen, and Y. Kashino, 2013: Quasistationary North Equatorial Undercurrent jets across the tropical North Pacific Ocean. *Geophys. Res. Lett.*, **40**, 2183-2187, doi:10.1002/grl.50394.

Qu, T., 2002: Depth distribution of the subtropical gyre in the North Pacific. *J. Oceanogr.*, **58**, 525-529.

Qu, T., and J. Chen, 2009: A North Pacific decadal variability in subduction rate. *Geophys. Res. Lett*., **36**, L22602, doi:10.1029/2009GL040914

Qu, T., S.-P. Xie, H. Mitsudera, and A. Ishida, 2002: Subduction of the North Pacific mode waters in a global high-resolution GCM. *J. Phys. Oceanogr*. **32**, 746–763

Reid, J. L., and R. S. Arthur, 1975: Interpretation of maps of geopotential anomaly for deep Pacific Ocean. *J. Mar. Res.*, **33** (Suppl.), 37-52.

Rhines, P. B., and W. R. Young, 1982: A theory of the wind-driven circulation. Part I: mid-ocean gyres. *J. Mar. Res.*, **40** (Suppl), 559-596.

Richards, K. J., N. A. Maximenko, F. O. Bryan, and H. Sasaki, 2006: Zonal jets in the Pacific Ocean. *Geophys. Res. Lett*., **33**, L03605, doi:10.1029/2005GL024645.

Richards, K. J., H. Sasaki, and F. O. Bryan 2008: Jets and waves in the Pacific Ocean, in *High-Resolution Numerical Modelling of the Atmosphere and Ocean*, edited by K. Hamilton and W. Ohfuchi, pp. 182–196, Springer, New York.

Rienecker, M. M., M. J. Suarez, R. Gelaro, R. Todling, J. Bacmeister, E. Liu, M. G. Bosilovich, S. D. Schubert, L. Takacs, G. Kim, S. Bloom, J. Chen, D. Collins, A. Conaty, A. D. Silva, W. Gu, J. Joiner, K. D. Koster, R. Lucchesi, A. Molod, T. Owens, S. Pawson, P. Pegion, C. R. Redder, R. Reichle, F. R. Robertson, A. G. Ruddick, M. Sienkiewicz, and J. Woollen, 2011: MERRA:NASA's Modern-Era Retrospective Analysis for Research and Applications. *J. Climate*, **24**, 3624-3648.

Roemmich, D., and J. Gilson, 2009: The 2004–2008 mean and annual cycle of temperature, salinity, and steric height in the global ocean from the Argo Program. *Prog. Oceanogr*., **82**, 81–100, doi:10.1016/j.pocean.2009.03.004.

Sasaki, H., B. Taguchi, N. Komori, and Y. Masumoto, 2013: Influence of Local Dynam-

ical Air-Sea Feedback Process on the Hawaiian Lee Countercurrent. *J. Climate*, **26**, 7267-7279.

Sekine, Y., and K. Kutsuwada, 1994: Seasonal Variation in Volume Transport of the Kuroshio South of Japan. *J. Phys. Oceanogr.*, 24, 261-272.

Stommel, H., 1948: The westward intensification of wind-driven ocean currents. *Trans. Amer. Geophys. Union*, **29**, 202-206.

Stommel, H., and F. Schott, 1977: The beta spiral and the determination of the absolute velocity field from hydrographic station data. *Deep-Sea Res.*, **24**, 325-329.

Suga, T., Y. Takei, and K. Hanawa, 1997: Thermostad distribution in the North Pacific subtropical gyre: the central mode water and the subtropical mode water. *J. Phys. Oceanogr.*, **27**, 140-152.

Suga, T., K. Motoki, Y. Aoki, and A. M. Macdonald, 2004: The North Pacific climatology of winter mixed layer and mode waters. *J. Phys. Oceanogr.*, **34**, 3–22.

Suga, T., Y. Aoki, H. Saito, and K. Hanawa, 2008: Ventilation of the North Pacific subtropical pycnocline and mode water formation. *Prog. Oceanogr*., **77**, 285–297.

Sverdrup, H. U., 1947: Wind-driven currents of a baroclinic ocean; with application to the equatorial currents of the eastern Pacific. *Proc. Natl. Acad. Sci. USA*, **33**, 318-326.

Sverdrup, H. U., M. W. Johnson, and R. H. Fleming, 1942: The Oceans: Their Physics, Chemistry and General Biology. Prentice-Hall, Englewood Cliffs, New York, 1087 pp.

Taguchi, B., R. Furue, N. Komori, A. Kuwano-Yoshida, M. Nonaka, H. Sasaki, and W. Ohfuchi, 2012: Deep oceanic zonal jets constrained by fine-scale wind stress curls in the South Pacific Ocean: A high-resolution coupled GCM study. *Geophys. Res. Lett.*, **39**, L08602, doi:10.1029/2012GL051248.

Talley, L. D., 1985: Ventilation of the Subtropical North Pacific: The Shallow Salinity Minimum. *J. Phys. Oceanogr.*, **15**, 633-648.

Talley, L. D., 2007: Hydrographic Atlas of the World Ocean Circulation Experiment (WOCE: Volume 2: Pacific Ocean). Ed. M. Sparrow, P. Chapman and J. Gould, International WOCE Project Office, Southampton, U.K., ISBN 0-904175-54-5.

Talley, L. D., G. L. Pickar, W. J. Emery, J. H. Swift, 2011: Descriptive physical oceanography: an introduction. Academic Press, New York, 560 pp.

Tanaka, H. L., N. Ishizaki, and A. Kitoh, 2004: Trend and interannual variability of Walker, monsoon and Hadley circulations defined by velocity potential in the upper troposphere. *Tellus A*, **56**, 250–269.

Tokinaga, H., Y. Tanimoto, S.-P. Xie, T. Sampe, H. Tomita, and H. Ichikawa, 2009: ocean frontal effects on the vertical development of clouds over the western North Pacific: In situ and satellite observations. *J. Climate*, **22**, 4241–4260.

Toyoda T., T. Awaji, Y. Ishikawa, and T. Nakamura, 2004: Preconditioning of winter mixed layer in the formation of North Pacific eastern subtropical mode water. *Geophys. Res. Lett.*, **31**, L17206, doi:10.1029/2004GL020677.

Tsujino, H., and T. Yasuda, 2004: Formation and circulation of mode waters of the North Pacific in a high-resolution GCM. *J. Phys. Oceanogr.*, **34**, 399–415.

Uda, M., and K. Hasunuma, 1969: The eastward subtropical countercurrent in the western North Pacific Ocean. *J. Oceanogr. Soc. Jpn.*, **25**, 201-210.

Williams R. G., 1991: The role of the mixed layer in setting the potential vorticity of the main thermocline. *J. Phys. Oceanogr.*, **21**, 1803–1814.

Xie, S.-P., W. T. Liu, Q. Liu, and M. Nonaka, 2001: Far-reaching effects of the Hawaiian Islands on the Pacific Ocean–atmosphere system. *Science*, **292**, 2057-2060.

Xie, S.-P., L.-X. Xu, Q. Liu, and F. Kobashi, 2011: Dynamical role of mode water venti-

lation in decadal variability in the central subtropical gyre of the North Pacific. *J. Climate*, **24**, 1212-1225.

Yasuda, I, 2003: Hydrographic structure and variability of the Kuroshio-Oyashio transition area. *J. Oceanogr*., **59**, 389–402.

Yoshikawa, Y., J. A. Church, H. Uchida, and N. J. White, 2004: Near bottom currents and their relation to the transport in the Kuroshio Extension. *Geophys. Res. Lett.*, **31**, L16309, doi:10.1029/2004GL020068.

Young, W. R., and P. B. Rhines, 1982: A theory of the wind-driven circulation. Part II: Gyre with western boundary layers. *J. Mar. Res.*, **40** (Suppl), 849-872.